Since 1955

Strojniški vestnik

Journal of Mechanical Engineering

no. 1
year 2019
volume 65

Strojniški vestnik – Journal of Mechanical Engineering (SV-JME)

Aim and Scope

The international journal publishes original and (mini)review articles covering the concepts of materials science, mechanics, kinematics, thermodynamics, energy and environment, mechatronics and robotics, fluid mechanics, tribology, cybernetics, industrial engineering and structural analysis.

The journal follows new trends and progress proven practice in the mechanical engineering and also in the closely related sciences as are electrical, civil and process engineering, medicine, microbiology, ecology, agriculture, transport systems, aviation, and others, thus creating a unique forum for interdisciplinary or multidisciplinary dialogue.

The international conferences selected papers are welcome for publishing as a special issue of SV-JME with invited co-editor(s).

Editor in Chief
Vincenc Butala
University of Ljubljana, Faculty of Mechanical Engineering, Slovenia

Technical Editor
Pika Škraba
University of Ljubljana, Faculty of Mechanical Engineering, Slovenia

Founding Editor
Bojan Kraut
University of Ljubljana, Faculty of Mechanical Engineering, Slovenia

Editorial Office
University of Ljubljana, Faculty of Mechanical Engineering
SV-JME, Aškerčeva 6, SI-1000 Ljubljana, Slovenia
Phone: 386 (0)1 4771 137
Fax: 386 (0)1 2518 567
info@sv-jme.eu, http://www.sv-jme.eu

Print: Papirografika, printed in 300 copies

Founders and Publishers
University of Ljubljana, Faculty of Mechanical Engineering, Slovenia
University of Maribor, Faculty of Mechanical Engineering, Slovenia
Association of Mechanical Engineers of Slovenia
Chamber of Commerce and Industry of Slovenia, Metal Processing Industry Association

President of Publishing Council
Mitjan Kalin
University of Ljubljana, Faculty of Mechanical Engineering, Slovenia

Vice-President of Publishing Council
Bojan Dolšak
University of Maribor, Faculty of Mechanical Engineering, Slovenia

Cover:
The gearbox with composite gear train is composed of primary planetary gear and two-stage spur gear. Fault diagnosis test of gearbox adopts sun gear and spur gear as fault gear and fault type includes snaggletooth and abrasion. Fault feature extraction method based on EEMD and translation-invariant multiwavelets neighboring coefficients can effectively extract the single and mixed fault features of the gearbox with composite gear train.

Image courtesy:
Shanxi Key Laboratory of Fully Mechanized Coal Mining Equipment, Taiyuan University of Technology, China

ISSN 0039-2480, ISSN 2536-2948 (online)

General information

Strojniški vestnik – Journal of Mechanical Engineering is published in 11 issues per year (July and August is a double issue).

Institutional prices include print & online access: institutional subscription price and foreign subscription €100,00 (the price of a single issue is €10,00); general public subscription and student subscription €50,00 (the price of a single issue is €5,00). Prices are exclusive of tax. Delivery is included in the price. The recipient is responsible for paying any import duties or taxes. Legal title passes to the customer on dispatch by our distributor. Single issues from current and recent volumes are available at the current single-issue price. To order the journal, please complete the form on our website. For submissions, subscriptions and all other information please visit: *http://www.sv-jme.eu.*

You can advertise on the inner and outer side of the back cover of the journal. The authors of the published papers are invited to send photos or pictures with short explanation for cover content.

We would like to thank the reviewers who have taken part in the peer-review process.

SV-JME is indexed / abstracted in: SCI-Expanded, Compendex, Inspec, ProQuest-CSA, SCOPUS, TEMA. The list of the remaining bases, in which SV-JME is indexed, is available on the website.

The journal is subsidized by Slovenian Research Agency.

Strojniški vestnik - Journal of Mechanical Engineering is available on *https://www.sv-jme.eu*.

Contents

Strojniški vestnik - Journal of Mechanical Engineering
volume 65, (2019), number 1
Ljubljana, January 2019
ISSN 0039-2480

Published monthly

Papers

Strojniški vestnik - Journal of Mechanical Engineering 65(2019)1, 3-11
Received for review: 2018-04-23

Received revised form: 2018-09-10
DOI:10.5545/sv-jme.2018.5441
Original Scientific Paper
Accepted for publication: 2018-09-25

A Fault Feature Extraction Method for a Gearbox with a Composite Gear Train Based on EEMD and Translation-Invariant Multiwavelet Neighbouring Coefficients

Xinyu Pang[1,2,*] – Baoan Cheng[1] – Zhaojian Yang[1,2] – Feng Li[1]
[1] Taiyuan University of Technology, College of Mechanical Engineering, China
[2] Shanxi Key Laboratory of Fully Mechanized Coal Mining Equipment, China

Although gearboxes with composite gear trains have been widely used in industrial production, it remains difficult to extract their fault signal features due to relatively complex vibration signals. This paper proposes an effective fault feature extraction method based on ensemble empirical mode decomposition (EEMD) and translation-invariant multiwavelet neighbouring coefficients, through which a clear envelope spectrum of gearbox vibration signals can be obtained. Compared with EEMD denoising or translation-invariant multiwavelet denoising using neighbouring coefficients alone, the method combining both of the denoising approaches can not only effectively suppress the signal noise but also fully retain the fault feature information. The presented method was further experimentally verified using a test rig for a gearbox with a composite gear train. Fault diagnosis was conducted with a single fault, such as snaggletooth and abrasion, as well as mixed faults at different locations. The results have shown that this method can effectively extract the fault features and improve the fault detection rate of a gearbox with a composite gear train.

Keywords: composite gear train; feature extraction; EEMD; multiwavelet neighbouring coefficients

Highlights

- *This paper proposes a fault feature extraction method based on EEMD and translation-invariant multiwavelet neighbouring coefficients.*
- *This method can be used for gearboxes with composite gear trains.*
- *This method was verified in a test rig with a composite gear train.*
- *The results showed this method is suitable not only for single fault but also for mixed faults.*

0 INTRODUCTION

A gearbox with a composite gear train is generally composed of an ordinary gear train and a planetary gear train. It has been widely used in the transmission systems of mechanical equipment, such as coal mine shearer's ranging arm gearboxes, wind turbine gearboxes, and automotive transmissions, etc. [1] to [3]. Compared with ordinary gear train [4] to [6], the complex structure of the composite gear train inevitably leads to its complex vibration characteristics. Its vibration signals contain vibration characteristics [7] and [8] of both ordinary gear train and planetary gear train as well as coupled vibration. Therefore, it is of significance to investigate effective fault diagnosis methods for gearboxes with composite gear trains.

However, its fault features are apt to be disturbed by noises, because its vibration signals are weak and mainly in the low-frequency part. As a result, signal denoising is the chief issue that needs to be solved for fault diagnosis [9] and [10]. At present, the time-frequency and multiresolution characteristics of wavelet transform are mainly utilized for signal denoising. A denoising method based on wavelets has been widely applied in engineering, especially wavelet threshold denoising methods [11] to [13].

Given that the wavelet threshold denoising does not consider the relativity of neighbouring wavelet coefficients, Cai and Silverman [14] proposed a denoising method using neighbouring wavelet coefficients (neighbouring coefficients, NeighCoeff), which considers the relativity of neighbouring wavelet coefficients to improve the denoising effect. Through changing the shrinkage factor of neighbouring coefficients to better extract information of vibration characteristics from noises, Yang and Zhao [15] made some improvements to the NeighCoeff denoising method and successfully realized early weak fault diagnosis of bearings. Strela et al. [16] proposed a multiwavelet scalar denoising method by introducing wavelet soft and hard threshold denoising into multiwavelet transform. Downie and Silverman [17] proposed a multiwavelet vector threshold denoising method by taking account of the relativity of the multiwavelet vector coefficients. To eliminate the Gibbs phenomenon, which exists in the above-mentioned multiwavelet threshold denoising

---

*Corr. Author's Address: Taiyuan University of Technology, College of Mechanical Engineering, No.79, Yingze West Street, Taiyuan, China, typangxy@163.com

method, Bui and Cheng [18] applied the translation-invariant denoising method into multiwavelet denoising to demonstrate that a translation-invariant multiwavelet denoising method has excellent denoising characteristics. A denoising method using neighbouring coefficients into multiwavelet denoising, which has achieved good results in electric power systems has been introduced in the literature [19]. Hu et al. [20] applied the translation-invariant multiwavelets denoising method using neighbouring coefficients into fault diagnosis for satellite communication antenna, which has effectively extracted weak characteristics of early faults. Yuan et al. [21] proposed a denoising method based on translation-invariant multiwavelet neighbouring coefficients, which has successfully extracted the fault feature information of early gear cracks influenced by noise.

In addition to the above-mentioned study on the improvement of the denoising method, signal denoising can be combined with empirical mode decomposition (EMD) to further increase the effectiveness of fault feature extraction. Liu et al. [22] combined a threshold denoising method based on EMD with a probabilistic neural network (PNN) to denoise vibration signals of a rotor system and compared it with a wavelet threshold denoising method and a back propagation neural network (BPNN) denoising method. The comparative results showed that the former has better denoising characteristics. Aiming to solve the problem that the diagnosis signals of a planetary gearbox of a wind turbine generator system under variable working condition are obviously non-linear and nonstationary, which leads to difficulty in fault feature extraction, Si et al. [23] proposed a new fault feature extraction method based on EMD and demodulated resonance techniques. According to experimental results, this method is feasible in the aspect of the vibration signal denoising and fault feature extraction of a planetary gearbox. Lee et al. [24] proposed a method for bearing test and fault diagnosis based on on ensemble empirical mode decomposition (EEMD), which integrated particle swarm optimization (PSO), Principal Component Analysis (PCA), etc. with EEMD to extract the fault features of bearings. Given the difficulty in extracting multi-fault features of bearings, Gong et al. [25] suggested a fault feature extraction method based on EEMD and spectrum kurtosis (SK), which is applicable to the fault feature extraction of rotor imbalance and multi-faults of bearings. Zhang et al. [26] presented a fault feature extraction method for gear based on EMD, sample entropy, and grey relation to extract the fault features of gears influenced by noise. Experimental results showed that this method could effectively extract the fault feature information of gears. For planetary gear fault diagnosis, Chen et al. [27] proposed a method based on the multi-scale fractal box dimension of complementary ensemble empirical mode decomposition (CEEMD) and extreme learning machine (ELM).

By combining translation-invariant multiwavelet neighbouring coefficients and EEMD, this paper proposes a fault feature extraction method based on EEMD and translation-invariant multiwavelets neighbouring coefficients. The presented method is applied in fault diagnosis of a gearbox with a composite gear train so as to extract the fault features of such a gearbox train, which is disturbed by noise.

The first section of this paper introduces signal feature extraction method based on EEMD and translation-invariant multiwavelet neighbouring coefficients. The second section introduces a test rig for a gearbox with a composite gear train. The experiment and simulation results and discussions are given in sections 3 and 4. Finally, conclusions of the study are provided.

1 METHODS

1.1 EEMD

EEMD is an improved algorithm of EMD, which is a self-adaptive decomposition method used to process non-linear and non-stationary signals, can decompose the signal into a limited number of intrinsic mode functions (IMF) components ranging from high frequencies to low frequencies. To eliminate mode mixing of EMD, EEMD introduces white Gaussian noise into original signals. By taking advantage of the homogeneous distribution of white Gaussian noise, different scale components of original signals are automatically distributed to an appropriate reference scale. Steps of EEMD decomposition are as follows [28]:

1. Set the signal to be decomposed as $x(t)$, white Gaussian noise with the same length of $x(t)$ as $n_i(t)$ to obtain a new signal:

$$x_i(t) = x(t) + n_i(t),\ i = 1, 2, ..., I. \tag{1}$$

2. Conduct EMD decomposition on noisy signal $x_i(t)$ to obtain a new intrinsic mode component IMF_k^i, in which $k = 1, 2, ..., K$.
3. Repeat step (1) and (2) and add different white Gaussian noise sequence $n_i(t)$ each time.

4. Conduct overall average calculation on each obtained group of IMF_k^i components.

$$\mathrm{IMF}_k = \frac{1}{I}\sum_{i=1}^{I}\mathrm{IMF}_k^i. \tag{2}$$

1.2 Translation-Invariant Multiwavelets Neighbouring Coefficients

The principle of traditional multiwavelet threshold denoising is the same as that of single wavelet threshold denoising [29]. Both enable to achieve the goal of denoising by setting a threshold to eliminate partial wavelet coefficients. The former has the advantage of symmetry, compact support, orthogonality and high order vanish moments. Therefore, compared with a single wavelet, it has a better denoising effect. However, this method ignores the relativity of neighbouring wavelet coefficients, which has an impact on the effectiveness of feature information. As a result, the wavelet denoising using neighbouring coefficients proposed by Cai and Silverman [14] is introduced into translation-invariant multiwavelets, which has considered the relativity of multiwavelet coefficients, which can effectively retain the local feature information of signals.

Set $\mathbf{d}_{j,k}^{(h)}$ as the high-frequency coefficient of the j layer with translation amount h after translation-invariant multiwavelet decomposition and define the variable $\theta_{j,k}^{(h)} = \left(\mathbf{d}_{j,k}^{(h)}\right)^{\mathrm{T}}\left(\mathbf{V}_j^{(h)}\right)\left(\mathbf{d}_{j,k}^{(h)}\right)$ as a basic variable of multiwavelet denoising using neighbouring coefficients, in which $\mathbf{V}_j^{(h)}$ is the covariance matrix of $\mathbf{d}_{j,k}^{(h)}$ and can be estimated using a robust coefficient.

In view of the multiwavelet coefficient and relativity of adjacent points, define a new variable:

$$\left(S_{j,k}^{(h)}\right)^2 = \left(\theta_{j,k-1}^{(h)}\right)^2 + \left(\theta_{j,k}^{(h)}\right)^2 + \left(\theta_{j,k+1}^{(h)}\right)^2. \tag{3}$$

According to the shrinkage rule of neighbouring coefficients, the coefficient obtained after translation-invariant multiwavelets denoising using neighbouring coefficients reads:

$$\hat{d}_{j,k}^{(h)} = \begin{cases} d_{j,k}^{(h)}\left[1-\left(\dfrac{\lambda^{(h)}}{S_{j,k}^{(h)}}\right)^2\right] & \left(S_{j,k}^{(h)}\right)^2 \geq \left(\lambda_j^{(h)}\right)^2 \\ 0 & \left(S_{j,k}^{(h)}\right)^2 < \left(\lambda_j^{(h)}\right)^2 \end{cases}, \tag{4}$$

where, $\lambda_j^{(h)} = 2\ln n_j^{(h)}$, referring to threshold $n_j^{(h)}$ refers to wavelet coefficient of the j layer after multiwavelet decomposition. Obtain signal $xr_{0,k}^{(h)}$ after conducting translation-invariant multiwavelet anti-transform reconstruction denoising on coefficient $\hat{d}_{j,k}^{(h)}$, and then conduct cyclic anti-translation on $xr_{0,k}^{(h)}$ as well as corresponding postprocessing to obtain a set of one-dimensional output signals $y^{(h)}$ and finally conduct the average calculating operation on $y^{(h)}$ to generate a signal after translation-invariant multiwavelets denoising using neighbouring coefficients.

1.3 Feature Extraction Method Based on EEMD and Translation-Invariant Multiwavelet Neighbouring Coefficients

Translation-invariant multiwavelet denoising using neighbouring coefficients acts on the entire length of the signal, while noises are generally distributed in the high-frequency part of the signal. To better retain the effective feature information while denoising, the high-frequency part of the signal needs to be denoised and reconstructed with the low-frequency part.

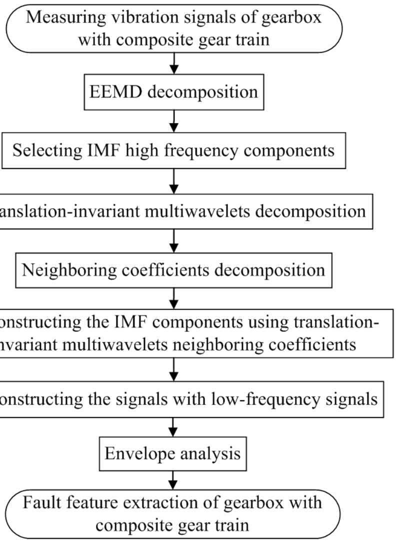

Fig. 1. *Procedure of the method*

This paper combines the translation-invariant multiwavelet denoising method using neighbouring coefficients with EEMD to diagnose the faults of a gearbox with a composite gear train. The specific procedure of the method is shown in Fig. 1. Firstly, conduct EEMD on the signal to select IMF high-frequency components containing the main information from obtained IMF components according to the energy-correlation coefficient, denoise the IMF high-frequency components with translation-invariant multiwavelet neighbouring coefficients, and then reconstruct them with low-frequency signals to obtain the frequency spectrum and spectrum envelope of denoised signal and complete the fault feature extraction of a gearbox with a composite gear train.

2 EXPERIMENTAL

2.1 Test Rig and Fault Gear

A Drivetrain Diagnostics Simulator (DDS) of SpectraQuest from the US is adapted for the test, as seen in Fig. 2a. The gearbox with a composite gear train is composed of a primary planetary gear and a two-stage spur gear, in which the planetary gearbox has four planet gears with a fixed tooth ring. The schematic diagram of its transmission system is shown in Fig. 2b. The gear parameters are shown in Table. 1. The fault diagnosis test of the gearbox is conducted by pre-setting different gear faults. The test adopts unidirectional acceleration sensors with sample frequency set as 10 kHz and motor speed of 3,000 r/min.

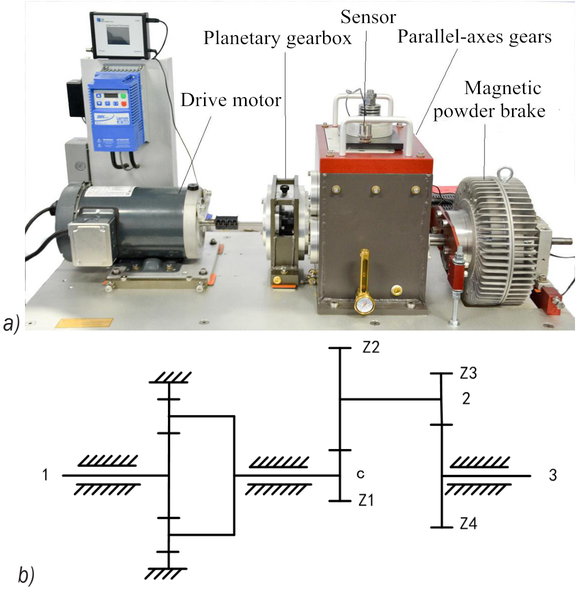

Fig. 2. Test-bed; a) DDS, and b) transmission structure diagram of gearbox

Table 1. *Parameters of gearbox*

Gear	Teeth number	Gear	Teeth number
Sun gear Z_s	28	Spur Gear Z_1	29
Planet gear Z_p	36	Spur Gear Z_2	100
Tooth ring Z_r	100	Spur Gear Z_3	36
		Spur Gear Z_4	90

According to the distribution location of gear faults, they fall into two categories, i.e. the first category is a localized fault, typically such as snaggletooth, missing tooth, tooth root crack; the other is uniformly distributed faults, typically such as abrasion. The test uses the sun gear and spur gear Z_3 as fault gears, and the fault types include snaggletooth and abrasion. For the photo of fault gear of gearbox, please refer to Fig. 3.

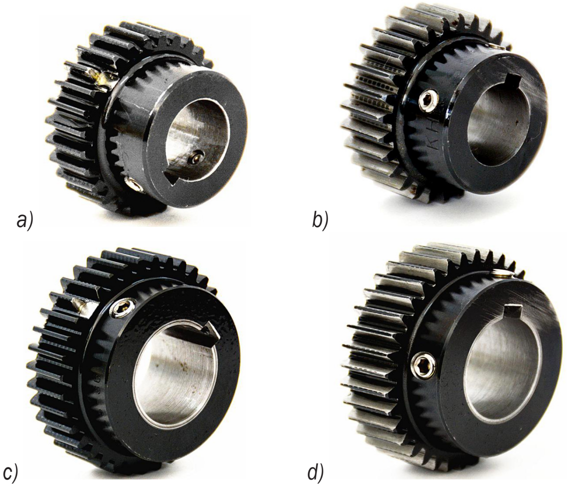

Fig. 3. *Fault gear; a) sun gear with snaggletooth, b) sun gear with abrasion, c) spur gear with snaggletooth, and d) spur gear with abrasion*

Without loss of generality, the experiment is conducted under three circumstances, i.e. fault-free, single fault and mixed fault. The effect of the feature extraction method based on EEMD and translation-invariant multiwavelet neighbouring coefficients is further verified through a uniformly distributed fault diagnosis test on different types of gearbox faults.

2.2 Fault Feature Frequency

The snaggletooth fault frequency of a spur gear is consistent with rotating frequency f_c, $f_{s2}^{(r)}$ and $f_{s3}^{(r)}$ of planet carrier c, shaft 2 and shaft 3. The abrasion fault frequency of the spur gear is consistent with mesh frequency f_{m2} and f_{m3} of Z1-Z2 and Z3-Z4. When a fault occurs, the amplitude and frequency multiplication of the rotating frequency or mesh frequency relating to such gear will change accordingly.

Given the revolution and rotation of the planetary gear, its fault frequency is different from that of the spur gear. Generally, the tooth ring is at rest while the sun gear, planetary gear and planet carrier rotate; in such circumstances, the mesh frequency is calculated as:

$$f_m = f_c Z_r = \left(f_s^{(r)} - f_c\right) Z_s, \tag{5}$$

where Z_r refers to tooth number of tooth ring.

The snaggletooth fault frequency of sun gear of the planetary gear train:

$$f_s = Nf_{m1}/Z_s \,. \tag{6}$$

Abrasion fault frequency of sun gear:

$$f_s = f_{m1}/Z_s \,. \tag{7}$$

Snaggletooth fault frequency of planetary gear:

$$f_p = Nf_{m1}/Z_p \,. \tag{8}$$

Abrasion fault frequency of planetary gear:

$$f_p = f_{m1}/Z_p \,. \tag{9}$$

Snaggletooth fault frequency of tooth ring:

$$f_r = Nf_{m1}/Z_r \,. \tag{10}$$

Abrasion fault frequency of tooth ring:

$$f_r = f_{m1}/Z_r \,. \tag{11}$$

3 EXPERIMENTAL RESULTS AND DISCUSSION

3.1 Single Fault

3.1.1 Snaggletooth of Spur Gear

Fig. 4a shows the spectrum envelope of the spur gear's snaggletooth signal. Unlike a normal signal, in addition to the rotating frequency of the planet carrier f_c, the absolute rotating frequency of the sun gear $f_{s1}^{(r)}$, and sidebands between both, there also exists a relatively high-frequency peak value, which is the same as rotating frequency of the spur gear, and the snaggletooth of the spur gear can be preliminarily considered. According to the partially amplified low-frequency part of the spectrum envelope, as shown in Fig. 4b, in addition to the fault frequency of spur gear f_s, its frequency multiplication nf_s also exists, which proves that the snaggletooth of spur gear occurs in the gearbox with a composite gear train.

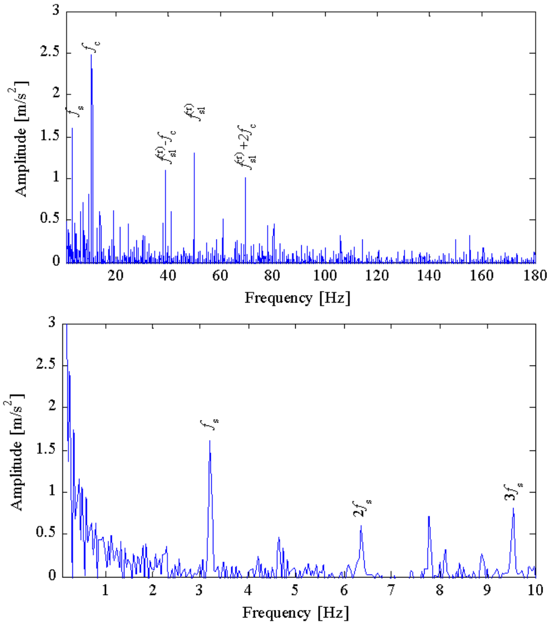

a)

b)

Fig. 4. *Signals of spur gear's snaggletooth; a) spectrum envelope, and b) partially amplified low-frequency part*

3.1.2 *Abrasion of Sun Gear*

Fig. 5 shows the signal spectrum envelope of the sun gear's abrasion fault. It can be seen that the spectrum of the signal is more complex than a normal signal. This is because the abrasion fault is distributed in each tooth of the sun gear; therefore, the former has more frequency components than a normal signal. The signal mainly concentrates around the sun gear's fault frequency f_s and the planet gear's fault frequency f_p. The main frequencies include the rotating frequency of the planet carrier f_c, the sun gear's fault frequency f_s, the planet gear's fault frequency f_p and the absolute rotating frequency of the sun gear $f_{s1}^{(r)}$. Frequency multiplication mainly includes nf_p, nf_s and sideband components of each signal. Because each tooth of the sun gear is faulty in the sun gear's abrasion fault, the assembly error of planet gear is bigger than that under normal circumstances, and the amplitude of planet gear's fault frequency f_p is higher than that under normal state. Furthermore, the sun gear's fault frequency f_s and frequency multiplication conform to the frequency feature of the sun gear's abrasion fault, which proves that the sun gear's abrasion occurs in gearboxes with composite gear trains.

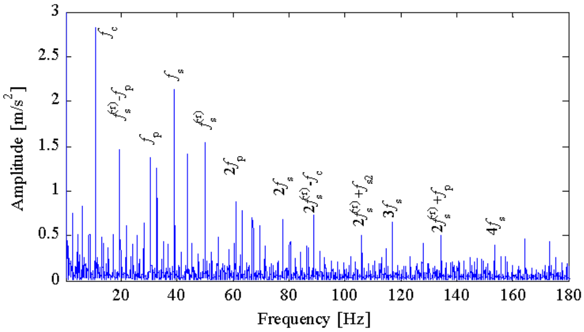

Fig. 5. *Signal spectrum envelope of sun gear's abrasion*

3.2 Mixed Fault

In practice, the faults of gearboxes with composite gear trains during operation are not always in the form of a single fault. Instead, multiple faults are often coupled in actual operation. Therefore, multi-fault diagnosis on such gearboxes is also performed. Fig. 6a shows the spectrum envelope of a mixed fault test signal after denoising. The main frequency in the signal includes the rotating frequency of planet carrier f_c, the absolute rotating frequency of sun gear $f_{s1}^{(r)}$, frequency f_s which is the same as the sun gear's localized fault frequency, the mesh frequency f_{m3} of spur gear Z3 and Z4. Because the sun gear's snaggletooth fault frequency f_s is related to the number of planet gears, and $n/4$ frequency multiplication such as $1/4\,f_s$ and $2/4\,f_s$ exists in the frequency spectrum, it can be diagnosed that the sun gear snaggletooth fault exists in gearboxes with composite gear trains. In addition, spur gear mesh frequency f_{m3} is higher than the peak value under the normal state. Therefore, it can be preliminarily ascertained that spur gear mesh frequency-related faults such as abrasion have occurred in gear. In view of this, we zoom in to the frequency range of the spectrum envelope. Fig. 6b shows that frequency multiplication such as $2\,f_s$, $2\,f_{m3}$ and $3\,f_{m3}$ also exists in the signal, which proves that mesh frequency f_{m3} is the fault frequency of spur gear abrasion. In consideration that f_{m3} is the mesh frequency of spur gear Z3 and Z4 and in order to further determine fault location, the low-frequency part of spectrum envelope is analysed. It is observed that the rotating frequency component of shaft 2 exists in the low-frequency part, which demonstrates that the abrasion fault occurs in spur gear Z3. In conclusion, both the sun gear's snaggletooth fault and the spur gear Z3's abrasion fault occur in gearboxes with composite gear trains, which is consistent with the test results.

According to the results obtained after denoising the vibration signal of gearboxes with composite gear trains under different fault states based on EEMD and translation-invariant multiwavelet neighbouring coefficients and conducting fault diagnosis on the spectrum envelop, this method can effectively improve the signal-to-noise ratio (SNR) of gearboxes with composite gear trains, extract signal feature information flooded in the noise, and help improve accuracy of fault diagnosis for gearboxes with composite gear trains.

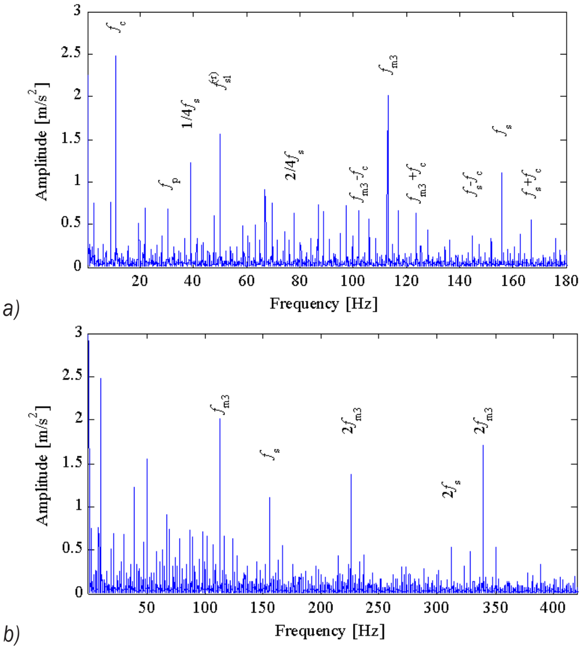

Fig. 6. *Spectrum envelope of mixed fault;*
a) small-frequency range, and b) large-frequency range

4 SIMULATION

4.1 Simulation Test

To verify the denoising characteristics of the feature extraction method based on EEMD and the translation-invariant multiwavelet neighbouring coefficients, select a set of modulated signals to simulate the vibration signals of gearboxes with composite gear trains. This model not only includes the modulation characteristics of the gearbox's vibration signals but also simulates the local faults of a group of sun gears of planetary gear trains. The model of vibration signals is shown as follows:

$$x(t) = x_1(t)\cdot[1 + x_2(t)] + n(t), \qquad (12)$$

$$x_1(t) = [1 - \cos 2\pi f_{s1}^{(r)}t][1 + A\cos(2\pi f_s t + \phi)] \times \cos[2\pi f_{m1}t + B\sin(2\pi f_s t + \varphi) + \theta], \qquad (13)$$

$$x_2(t) = \cos(\pi f_{m2}t + C\sin 2\pi f_{s2}^{(r)}t), \qquad (14)$$

where, $x_1(t)$ refers to the local fault signal of the sun gear, $x_2(t)$ refers to the modulated signals of the spur gear, $n(t)$ refers to white Gaussian noise, A, B and C refer to the intensity of amplitude modulation or frequency modulation, respectively, and ϕ, φ and θ refer to the initial phases (all set as zero). Those parameters are summarized in Table 2. The sampling frequency is set as 10 kHz.

Table 2. *Simulation signal parameters*

Parameter	Value
Intensity of amplitude modulation A	0.8
Intensity of frequency modulation B	0.8
Intensity of frequency modulation C	1.2
Fault frequency f_s	40 Hz
Sun gear rotate frequency $f_{s1}^{(r)}$	15 Hz
Planet gear mesh frequency f_{m1}	400 Hz
Spur gear rotate frequency $f_{s2}^{(r)}$	5 Hz
Spur gear mesh frequency f_{m2}	120 Hz

The length of the simulated signals is selected as 4096. The time-domain plot of original signals without noise is seen in Fig. 7a. There is obvious periodic impact in the vibration signals. Fig. 7b shows the time-domain plot of original signals added with -8 dB white Gaussian noise. Vibration signals of the gearbox are flooded in the noise. Therefore, periodic characteristics cannot be identified.

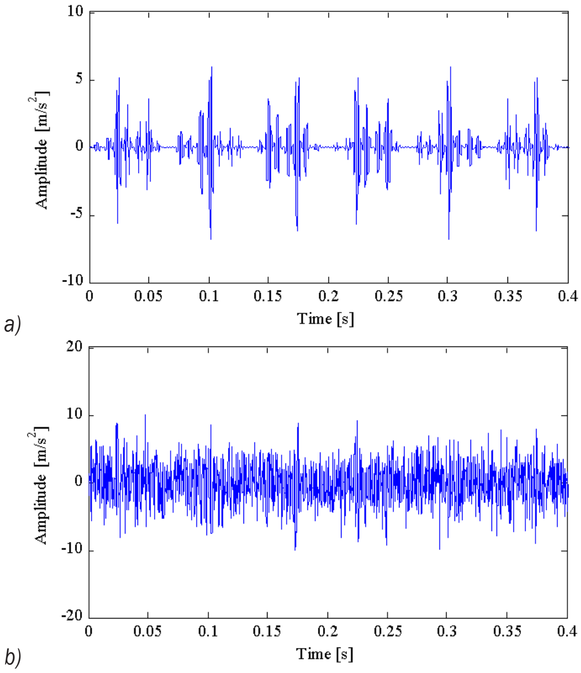

Fig. 7. Original signals; a) without noise, and b) with noise

This paper adopts the most common Geronimo, Hardin, and Massopust (GHM) multiwavelet in multiwavelet signal processing to denoise the noisy signal based on EEMD and translation-invariant multiwavelet neighbouring coefficients, in which the number of multiwavelet decomposition layer is 4 and the cyclic translation amount is 32.

4.2 Simulation Result and Analysis

To highlight the superiority of this method, we conduct denoising on the signal with the other two methods. The first one is EEMD, which achieves denoising by abandoning noisy components; the other one achieves signal denoising through translation-invariant multiwavelets neighbouring coefficients.

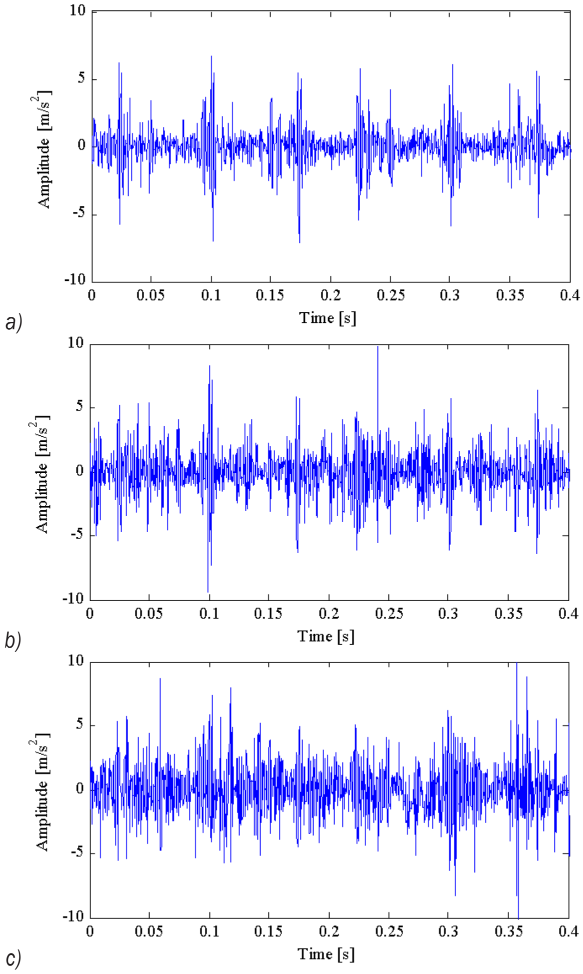

Fig. 8. *Time-domain plot of simulated signals denoising with three methods; a) EEMD and translation-invariant multiwavelets neighbouring coefficients, b) EEMD and, c) translation-invariant multiwavelets neighbouring coefficients*

Fig. 8 gives the time-domain plot of simulated signals denoising with three methods, respectively. It shows that three methods have obvious denoising effect. For the denoising method based on EEMD and translation-invariant multiwavelets neighbouring coefficients, in Fig. 8a it can be seen that more fully retains shock feature of the signal while achieving denoising. For the time-domain plot of the signal after EEMD decomposition and denoising through abandoning partial high-frequency IMF components containing noise, in Fig. 8b it is seen that the signal loses partial shock feature while being denoised, which has an impact on the effect of the gearbox's fault diagnosis. Compared with Fig. 8b, for the translation-invariant multiwavelets neighbouring coefficients denoising, as seen in Fig. 8c the signal has less feature information loss, but noise elimination is inadequate and there still exists partial noise feature information in the signal. That could disturb gearbox's fault diagnosis. Corresponding to Fig. 8, the SNR values are respectively 26.59, 19.99, and 16.94, respectively.

The Hilbert envelope analysis on the simulated signal before denoising and the denoised signal obtained through reconstruction with the denoising method based on EEMD and translation-invariant multiwavelets neighbouring coefficients is conducted. Spectrum envelopes of the signals are shown in Fig. 9. Except fault frequency f_s and spur gear mesh frequency f_{m2}, the other frequencies in Fig. 9a are disturbed by noise and thus not easily identifiable. After denoising, the signal in Fig. 9b has clear characteristic frequencies, including each main frequency, frequency multiplication and side frequency, which facilitates the fault diagnosis of the gearbox.

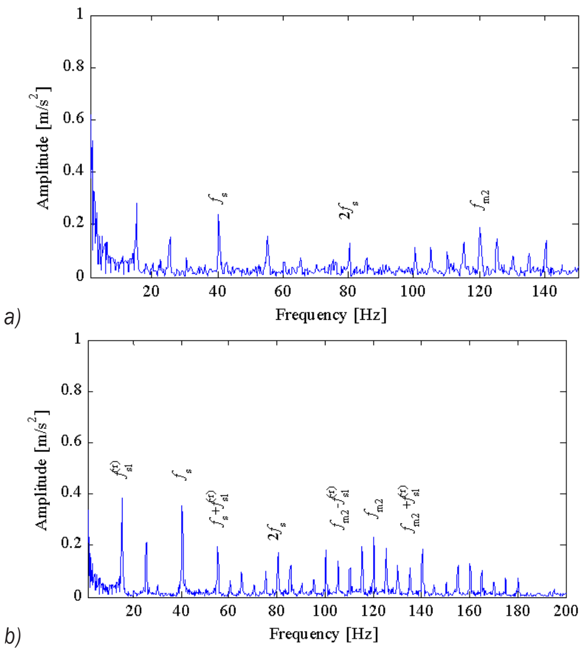

Fig. 9. Envelope spectrum of simulation signal;
a) before denoising, b) after denoising

By comparing the different denoising methods and fault feature extraction and identification, the simulation test proves that the fault diagnosis method of gearboxes with composite gear trains through denoising based on EEMD and translation-invariant multiwavelets neighbouring coefficients cannot only be more effective in improving the SNR of a signal, but also better retain the effective feature information of a signal while achieving denoising. That plays a significant role in improving the fault diagnosis accuracy of a gearbox with a composite gear train.

5 CONCLUSIONS

This paper combines EEMD with translation-invariant multiwavelet neighbouring coefficients to denoise the signals of a gearbox with a composite gear train and to extract its signal feature frequency so as to overcome the difficulty in signal feature extraction for such gearboxes. After conducting experimental tests on single fault and mixed faults of the gearboxes with composite gear trains, test results showed that the fault feature extraction method based on EEMD and translation-invariant multiwavelets neighbouring coefficients can effectively extract the fault feature information of such gearboxes, which facilitates the accurate identification of the faults. The simulation test simulates vibration signals containing noise and conducts denoising tests on signals containing noise with different methods. According to the simulation results, the denoising method based on EEMD and translation-invariant multiwavelets neighbouring coefficients cannot only effectively reduce signal noise but also fully retain the effective features of signals.

6 ACKNOWLEDGEMENTS

The authors are grateful for the financial support provided by the National Natural Science Foundation of China (51475318 and U1510116).

7 REFERENCES

[1] Zhou, D., Zhang, X.F., Zhang, Y.M. (2016). Dynamic reliability analysis for planetary gear system in shearer mechanisms. *Mechanism and Machine Theory*, vol. 105, p. 244-259, **DOI:10.1016/j.mechmachtheory.2016.07.007**.

[2] Gong, Y., Fei, J.-L., Tang, J., Yang, Z.-G., Han, Y.-M., Li, X. (2017). Failure analysis on abnormal wear of roller bearings in gearbox for wind turbine. *Engineering Failure Analysis*, vol. 82, p. 26-38, **DOI:10.1016/j.engfailanal.2017.08.015**.

[3] Kouroussis, G., Dehombreux, P., Verlinden, O. (2015). Vehicle and powertrain dynamics analysis with an automatic gearbox. *Mechanism and Machine Theory*, vol. 83, p. 109-124, **DOI:10.1016/j.mechmachtheory.2014.09.009**.

[4] Li, X.Y., Wang, N.N., Lv, Y.G., Zeng, Q.L., Hidenori, K. (2016). Tooth profile modification and simulation analysis of involute spur gear. *International Journal of Simulation Modelling*, vol. 15, no. 4, p. 649-662, **DOI:10.2507/IJSIMM15(4)6.358**.

[5] Zeng, Q.L., Wang, K., Wan, L.R., Zhang, X. (2017). Accurate modelling and transient meshing analysis of involute spur gear based on the principle of gear shaping. *International Journal of Simulation Modelling*, vol. 16, no. 2, p. 322-333, **DOI:10.2507/IJSIMM16(2)CO7**.

[6] Tang, Z.P., Sun, J.P., Yan, L., Zou, F. (2017). Dynamic contact analysis and tooth modification design for EMU traction gear. *International Journal of Simulation Modelling*, vol. 16, no. 4, p. 742-753, **DOI:10.2507/IJSIMM16(4)CO20**.

[7] Sharmaa, V., Parey, A. (2016). A review of gear fault diagnosis using various condition indicators. *Procedia Engineering*, vol. 144, p. 253-263, **DOI:10.1016/j.proeng.2016.05.131**.

[8] Praveenkumara, T., Saimuruganb, M., Krishnakumarc, P., Ramachandran, K.I. (2014). Fault diagnosis of automobile gearbox based on machine learning techniques. *Procedia Engineering, 12th Global congress on manufacturing and management*, vol. 97, p. 2092-2098, **DOI:10.1016/j.proeng.2014.12.452**.

[9] Moshrefzadeh , A., Fasana, A. (2017). Planetary gearbox with localised bearings and gears faults: simulation and time/frequency analysis. *Meccanica*, vol. 52, no. 15, p. 3759-3779, **DOI:10.1007/s11012-017-0680-7**.

[10] Merainani, B., Rahmoune, C., Benazzouz, D., Ould-Bouamama, B. (2018). A novel gearbox fault feature extraction and classification using Hilbert empirical wavelet transform, singular value decomposition, and SOM neural network. *Journal of Vibration and Control*, vol. 24, no. 12, p. 2512-2531, **DOI:10.1177/1077546316688991**.

[11] Deak, K., Mankovits, T., Kocsis, I. (2016). Optimal wavelet selection for the size estimation of manufacturing defects of tapered roller bearings with vibration measurement using Shannon Entropy Criteria. *Strojniški vestnik - Journal of Mechanical Engineering*, vol. 63, no. 1, p. 3-14, **DOI:10.5545/sv-jme.2016.3989**.

[12] Kumar, R., Singh, M. (2013). Outer race defect width measurement in taper roller bearing using discrete wavelet transform of vibration signal. *Measurement*, vol. 46, no. 1, p. 537-545, **DOI:10.1016/j.measurement.2012.08.012**.

[13] Lu, J.-Y., Lin, H., Dong, Y., Zhang Y.-S. (2016). A new wavelet threshold function and denoising application. *Mathematical Problems in Engineering*, p. 1-8, **DOI:10.1155/2016/3195492**.

[14] Cai, T.T., Silverman, B.W. (2001). Incorporating information on neighbouring coefficients into wavelet estimation. *Sankhya: The Indian Journal od Statistic: Series B*, vol. 63, no. 2, p. 127-148.

[15] Yang, S.P., Zhao. Z.H. (2013). Improved wavelet denoising using neighboring coefficients and its application to machinery fault diagnosis. *Journal of Mechanical Engineering*, vol. 49, no. 17, p. 137-141, **DOI:10.3901/JME.2013.17.137**.

[16] Strela, V., Heller, P.N., Strang, G. Topiwala, P., Heil, C. (1999). Application of multiwavelet filterbanks to image processing. *IEEE Transactions on Image Processing*, vol. 8, no. 4 p. 548-563, **DOI:10.1109/83.753742**.

[17] Downie, T.R., Silverman, B.W. (1998).Discrete multiple wavelet transform and thresholding methods. *IEEE Transactions on Signal Processing*, vol. 46, no. 9, p. 2558-2561, **DOI:10.1109/78.709546**.

[18] Bui, T.D. Chen, G.Y. (2002). Translation-invariant denoising using multiwavelets. *IEEE Transactions on Signal Processing*, vol. 46, no. 12, p. 3414-3420, **DOI:10.1109/78.735315**.

[19] Chen, G.Y., Bui, T.D. (2003). Multiwavelets denoising using neighboring coefficients. *IEEE Signal Processing Letters*, vol. 10, no. 7, p. 211-214, **DOI:10.1109/LSP.2003.811586**.

[20] Hu, X., Xi, Z., Li, K., Cong, B. (2013). Application of translation-invariant multiwavelets denoising using neighboring coefficients to fault diagnosis of antennas on vessel. *Proceedings International Conference on Mechatronic Sciences, Electric Engineering and Computer*, p. 870-873, **DOI:10.1109/MEC.2013.6885181**.

[21] Yuan, J., He, Z.J., Wang, X.D., Li, Z., Zi, Y.Y. (2009). Translation-invariant multiwavelets denoising using neighboring coefficients and its application to monitoring and diagnosis. *Journal of Mechanical Engineering*, vol. 45, no. 4, p. 155-160, **DOI:10.3901/JME.2009.04.155**.

[22] Liu, D., Zeng, H.T. Xiao, Z.H., Peng, L.H., Malik,O.P. (2017). Fault diagnosis of rotor using EMD thresholding-based de-noising combined with probabilistic neural network. *Journal of Vibroengineering*, vol. 19, no. 8, p. 5920-5931, **DOI:10.21595/jve.2017.18365**.

[23] Si, J.S., Cao, Y., Shi, X.J. (2017). Fault diagnosis of wind turbine planetary gear box based on EMD and resonance remodulation. *12th International Conference on Computer Science and Education*, p. 757-762, **DOI:10.1109/ICCSE.2017.8085595**.

[24] Lee, D.H., Ahn, J.H., Koh, B.H. (2017). Fault Detection of Bearing Systems through EEMD and Optimization Algorithm. *Sensors*, vol. 17, no. 11, p. 2477, **DOI:10.3390/s17112477**.

[25] Gong, X.Y., Du, W.L., Georgiadis, A., Zhao, B.W. (2017). Identification of multi-fault in rotor-bearing system using spectral kurtosis and EEMD. *Journal of Vibroengineering*, vol. 19, no. 7, p. 5036-5046, **DOI:10.21595/jve.2017.18671**.

[26] Zhang, W.B., Pu, Y.S., Zhu, J.X., Su, Y.P. (2013). Gear Fault Diagnosis Method Using EEMD Sample Entropy and Grey Incidence. *Advanced Materials Research*, vol. 694-697, p. 1151-1154, **DOI:10.4028/www.scientific.net/AMR.694-697.1151**.

[27] Chen, X.H., Cheng, G., Li, H.Y., Li, Y. (2017). Research of planetary gear fault diagnosis based on multi-scale fractal box dimension of CEEMD and ELM. *Strojniški vestnik - Journal of Mechanical Engineering*, vol. 63, no. 1, p. 45-55, **DOI:10.5545/sv-jme.2016.3811**.

[28] Leng, J.F., Jing, S.X. Luo, C.X., Wang, Z.Y. (2017). EEMD-Based cICA method for single-channel signal separation and fault feature extraction of gearbox. *Journal of Vibroengineering*, vol. 19, no. 8, p. 5858-5873, **DOI:10.21595/jve.2017.18115**.

[29] Hua, W., Niu, Z.H., Wang, Z.Y., Leng,J.F. (2016). Mine gearbox fault diagnosis based on neighboring coefficients of translation-invariant multiwavelets. *Journal of China Coal Society*, vol. 41, no. s1, p. 253-258, **DOI:10.13225/j.cnki.jccs.2015.0968.**

Strojniški vestnik - Journal of Mechanical Engineering 65(2019)1, 12-20

DOI:10.5545/sv-jme.2018.5637
Original Scientific Paper
Received for review: 2018-07-09
Received revised form: 2018-11-09
Accepted for publication: 2018-12-13

Study on the Eligibility of Introducing Hybrid-Drive Buses into the Public Passenger Transport

Janez Blaž[1,*] – Samo Zupan[2] – Miha Ambrož[2]
[1] Republic of Slovenia, Ministry of Infrastructure, Slovenia
[2] University of Ljubljana, Faculty of Mechanical Engineering, Slovenia

The article presents the research related to the feasibility of introduction of alternative power source vehicles (hybrid system) into the public passenger transport (PPT) implemented as public service obligation of public passenger transport (PSO_PPT). The study examines and evaluates the existing implementation of 10 lines of PSO_PPT and implements the methods of mathematical calculations of the energy necessary to overcome the driving resistances of vehicles operating on these lines. The applied mathematical methods also include calculations of possible energy savings from implementing regenerative braking and a simulation of the reduction in air pollutant emissions. Furthermore the article presents the development of the experimental methods involving measurement of driving speeds, fuel consumption, altitude differences, number of brake applications as well as the time of braking during the bus ride along one of the observed lines in the pilot region. The results on the observed line were compared with mathematical calculations of the possible amount of energy regeneration. Based on the comparative analysis, we introduced the regeneration factor and used it to correct the previous mathematical calculations of the possible amount of energy regeneration due to braking on the other 9 lines in the selected pilot region. The final analysis has proven the eligibility of such research, which has demonstrated significant effects in energy savings (7 %) and the reduction of emissions (20 %) in the pilot area.
Keywords: public passenger transport, hybrid drive, regeneration energy, air pollutant emissions

Highlights
- *Introducing hybrid buses into the public passenger transport system could prove highly effective in ensuring energy regeneration and air pollutant emission reduction.*
- *The research has been conducted in the public service obligation of public passenger transport system, which is carried out in Slovenia with 1100 buses carrying around 48 million kilometres annually.*
- *Implementation of passenger transports is based on pre-defined infrastructure base with known elevation profiles, distances and pre-determined times, which were taken into account in these surveys.*
- *It is necessary to make theoretical calculations of the energy required to overcome all the driving resistance and the potential savings during braking and to carry out a comparison of these results with experimental data.*

0 INTRODUCTION

Research on the use of environmentally friendly buses in Europe [1] shows that approximately 30 % of registered buses meet the Euro I and II standard, slightly more than 30 % of buses meet the Euro III standard and just a little more than 30 % of buses meet the Euro IV and V or energy efficient vehicles (EEV) standard. As defined in the EU Strategies [2] and [3], the objective is to reduce greenhouse gas (GHG) emissions to be at least 60 % lower than in the year 1990 and be firmly on the path towards zero. The operational program of measures to decrease GHG emissions by 2020 in Slovenia [4] sets as an objective that traffic emissions are to be reduced by 15 % by 2030 compared to 2008. Research in the field of alternative drives in buses shows that there are two different architectures suitable for hybrid vehicles – series and parallel architecture [5]. Research [6] shows the simulation of energy-conversion efficiency of hybrid drives, while research [7] shows the characteristics from the fuel economic point of view. In the parallel system, the internal combustion engine and electric motor are independently connected through transmission. In the series system, the internal combustion engine is connected to a generator which charges the battery through a controller. It then powers the electric motor or transmission as shown in Fig. 1 [8].

As a result of the previous research review and in terms of the characteristics of the implementation of the 10 lines of public service obligation of public passenger transport (PSO_PPT) in the selected pilot area we continued the research taking into account the engineering solutions of the bus drives with the serial hybrid drive system [9] and [10] and in-wheel electric motors [11].

Regarding the efficiency level in series hybrid versions, research [12] shows that transmission offers approximately 90 % efficiency (η_t), while the motor drive offers approximately 83 % (η_{md}) and the generator approx. 90 % efficiency (η_g). Direct

---

*Corr. Author's Address: Republic of Slovenia, Ministry of Infrastructure, Langusova ulica 4, SI-1000 Ljubljana, Slovenia, janez.blaz@gov.si

efficiency between the internal combustion engine and the generator thus equals approximately 67 %. Research on the efficiency, which directly results from braking regeneration **[13]** shows that the level of efficiency ranges between 20 % and 42 %. Fig. 2 shows the conditions of the regeneration of the energy achieved through braking.

The driving behaviour plays a significant role in this regard. Eco driving **[13]** recaptured almost 42 % of the energy. The estimated mean value (η_{rb}) is approx. 30 %. Total regeneration efficiency (η_{rtot}) is thus:

$$\eta_{rtot} = \eta_t \cdot \eta_{md} \cdot \eta_g \cdot \eta_{rb}. \quad (1)$$

The entire research structure consists of analytical and experimental work. The analytical part (Section 1) describes the parameters that were used in the calculations for all 10 lines and whose meaning and values are shown in Table 2. The structure of the performance of the experiment is shown on one of these 10 lines. In Section 1.1. we present the equations we used to calculate the energy needed to overcome the driving resistances of a bus driving on a bus line, as well as the possible energy savings due to regenerative braking. In the following, we present the final result tables for all 10 lines calculated for a single journey

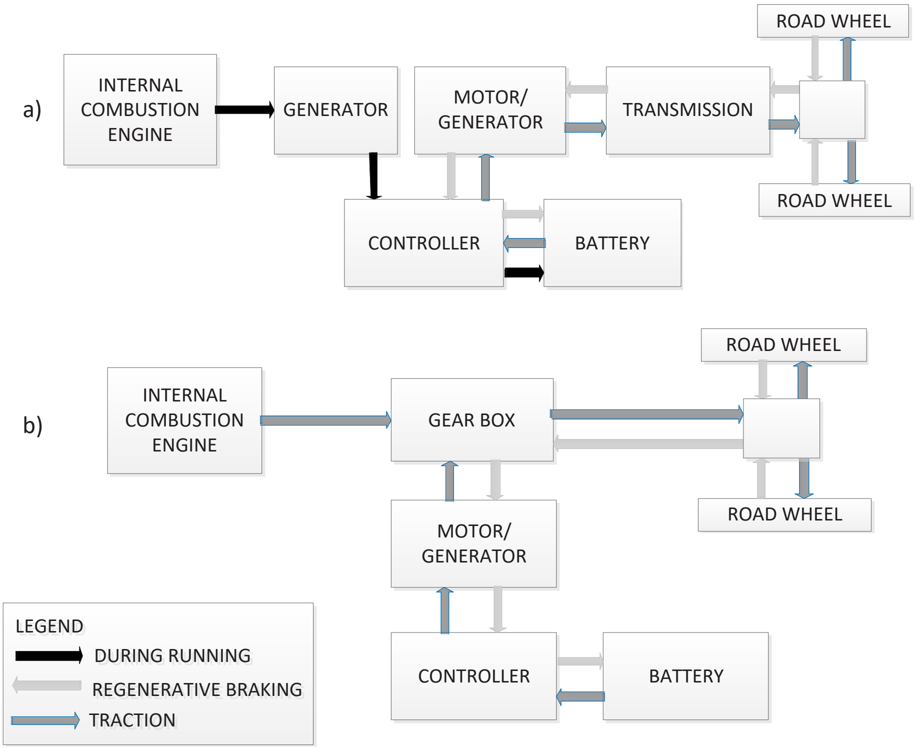

Fig. 1. *Two different architectures suitable for hybrid vehicles – a) series and b) parallel (re-drawn from [8])*

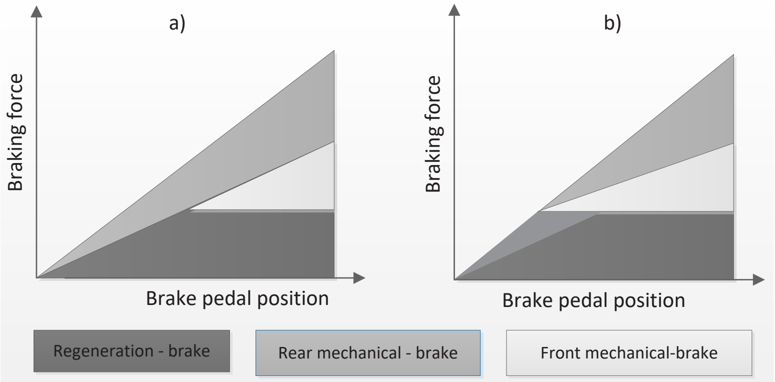

Fig. 2. *Generation of the regenerative energy through braking; a) hard, and b) soft braking (Re-drawn from [13])*

and at the annual level. Calculations are also made to investigate the reduction of pollutant emissions by using hybrid-drive buses.

1 WORKING METHODOLOGY AND CONDUCT OF THE EXPERIMENT

In view of the aforementioned need for research, the Banjšice Plateau near Nova Gorica with a characteristic hilly landscape was selected as the pilot area with the most suitable relief characteristics. Ten bus lines (Table 1) of the PSO_PPT operate on the area. The operator is professional bus company, which was awarded a concession by the Slovenian public transport authority (PTA), i.e. the Ministry of Infrastructure. The map of the pilot area with the bus lines as per Table 1, is shown in Fig. 3.

In the analytical part of the research, simulations and calculations were performed to overcome the following resistances during the bus traveling along the lines on the pilot area: rolling resistance, aerodynamic resistance, slope resistance and inertia mass resistance. We calculated the total energy required to overcome all the resistances (TEOR) and the energy saving potential of regenerative braking (ESPRB) **[14]** and **[8]**.

To enable calculations, a necessary basis was first provided based on the geographical features of each bus line **[15]**. For those segments, the slope inclinations and the route lengths were determined. Among the 10 selected lines included in the research, the measurements, i.e. the experimental part, were performed on Line_6, by acquiring and storing the vehicle diagnostic data from the vehicle controller area network (CAN) bus connector (Fig. 4). In accordance with the SAE J1939 protocol **[16]**, the operating parameter values were obtained as presented and marked in Table 2. The time history of the following values was significant: vehicle speed, detection of the brake switch and fuel rate (Fig. 5). The bus stop locations were manually added to the log file by the

Fig. 3. *Map of bus lines and station points on the pilot area*

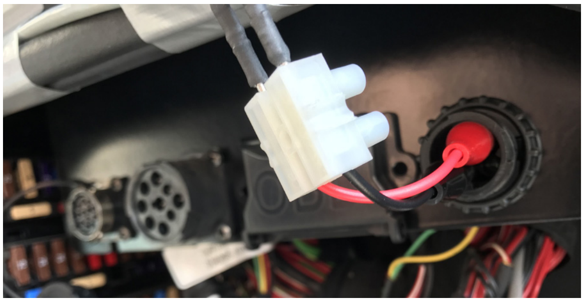

Fig. 4. *Connection of the computer interface probes to the vehicle CAN bus*

Table 1. *List of bus lines in the characteristic pilot area*

No.	Designation	Line	Length [km]	No. of bus stops	Travel time*
1	Line_1	Nova Gorica - Čepovan	35	19	1 h 5 min
2	Line_2	Čepovan - Šempeter pri Gorici	31	20	1 h 4 min
3	Line_3	Nova Gorica - Lokve	23	12	47 min
4	Line_4	Grgar - Šempeter pri Gorici	13	14	29 min
5	Line_5	Grgar - Nova Gorica	39	33	1 h 50 min
6	Line_6	Lokve - Nova Gorica	31	20	1 h 12 min
7	Line_7	Nova Gorica - Kal nad Kanalom	30	13	55 min
8	Line_8	Nova Gorica - Nova Gorica	36	22	1 h 17 min
9	Line_9	Banjšice - Nova Gorica	36	17	1 h 3 min
10	Line_10	Grgar - Nova Gorica	39	33	1 h 50 min

* The values of planned travel times on bus lines are taken from the applicable register of timetables within the Slovenian PSO_PPT system and relate to a single journey, yet are subject to the itinerary of a specific journey and other traffic factors.

operator. Measurements of the elevation profile of the driving route were performed with a GNSS device and synchronized with other measurements based on recorded measurement times. In the CAN messages, speed and fuel rate values are recorded as calculation values, while detection of the brake application is recorded as a bit sequence. Identification marks of the CAN messages for the individual quantities are explained in Table 2.

Throughout the entire measurement process for this bus line, the results were recorded in an electronic spreadsheet with 75,884 time intervals, which enabled

Table 2. *Input parameters in the analytical model and measurement evaluation model*

Parameter	Meaning	Unit	Values from	Values to	Source
R_{SUM}	Sum of resistances	[N]	-29,381.63	64,720.80	Eq. (2)
R_{R}	Rolling resistance	[N]	1,805.33	2,049.80	Eq. (3)
R_{A}	Aerodynamic resistance	[N]	0	248.25	Eq. (4)
R_{S}	Slope resistance	[N]	-29,381.63	64,720.80	Eq. (5)
R_{I}	Inertia mass resistance	[N]	-11,993.73	11,993.73	Eq. (6)
m	Mass of the vehicle and passengers	[kg]	12,430	13,930	Bus company and weighing
g	Gravitational acceleration	[m/s^2]	9.81	9.81	
α_{i}	Slope inclination	[°]	-12.42	28.27	Analyses of the elevation profile of bus lines
v_{i}	Vehicle speed	[m/s]	0	17.83	SAE J1939 message: 18FEF100 CCVS Cruise Control/Wheel-based vehicle Speed, byte 2 and 3
w_{i}	Wind speed against vehicle	[m/s]	0	0	
ρ_{A}	Density of surrounding air	[kg/m^3]	1.25	1.25	[14]
c_{w}	Aerodynamical drag coefficient	[-]	0.65	0.65	[14]
A	Vehicle frontal area	[m^2]	6.24	6.24	Bus type-approval certificate
δ	Inertia mass coefficient	[-]	1.05	1.05	
t_{i}	Acceleration/deceleration time (when braking or stopping)	[s]	0	11.712	Determined from the difference in the speed of the experimental bus drive
$TEOR$	Total energy required for a single bus journey on the line	[kWh]	21.59	55.89	Eq. (7)
$TEOR_{\mathrm{y}}$	Total energy required for all bus journeys per year	[kWh]	4,385.23	42,292.37	PTA Register of bus lines
$(s_{\mathrm{i}} - s_{\mathrm{i-1}})$	The length of the concerned itinerary segment on the observed line	[m]	0	295.8	Analyses of the elevation profile of bus lines
s_{j}, s_{n}	Distance needed for acceleration/deceleration at bus stops	[m]	41.839	41.839	Determined based on the average stopping times from the experimental part
$ESPRB$	The energy saving potential of regenerative braking for a single bus journey on the line	[kWh]	5.24	44.84	Eq. (8)
$ESPRB_{\mathrm{y}}$	The energy saving potential of regenerative braking for all bus journeys per year	[kWh]	3,579.51	11,544.75	PTA Register of bus lines
K_{reg}	Regeneration coefficient	[-]	1.742	1.742	Calculated from the analytical and experimental part (Section 1)
η_{rtot}	Total regeneration efficiency	[-]	0.201	0.201	Eq. (1)
FR	Fuel rate	[l/h]	0	60.7	SAE J1939 message: 18FEF200 FE Fuel economy, byte 1 and 2
BS	Brake switch	[-]	0	1	SAE J1939 message: 18FEF100 CCVS Cruise Control/Wheel-based vehicle Speed, byte 4
η_{t}	Transmission efficiency	[-]	0.9	0.9	[12]
η_{md}	Motor drive efficiency	[-]	0.83	0.83	[12]
η_{g}	Generator efficiency	[-]	0.9	0.9	[12]
η_{rb}	Regeneration braking efficiency	[-]	0.2	0.42	[13]

the reading of 151 cases of brake switch activation. Based on the data on speed changes during brake switch, calculations were made of kinetic energy and deceleration changes, which were then used in subsequent calculations of the regeneration coefficient. Based on the time history of the vehicle speed, numerical differentiation over time was applied to obtain data on the average deceleration value, which were then used to calculate the necessary braking distances and stopping times.

The results of these calculations were used in further research analyses. The total sum of kinetic energy changes during all 151 braking cases which could be used for *ESPRB*, amounts to 9.39 kWh. In the theoretical (analytical) part based on the equations of resistance sums, we obtained the calculated size of *ESPRB* on the same line, equals 5.39 kWh. From the values of the experimental (9.39 kWh) and analytical ESPRB (5.39 kWh), we obtained a quotient, which we named a regeneration coefficient (K_{reg}), the value of which is 1.742. In the analytical part, calculations were made taking into account the simulation of the conditions of the braking at 20 station points. Since the analytical part of calculations was performed on all 10 bus lines and the experimental part only on one line, the calculated regeneration coefficient K_{reg}, was used in the calculation on all other bus lines in the pilot area, as shown in Eq. (8).

Table 2 presents the input parameters which were used in the research described in this paper, whereby parameter values refer to the processed data on all 10 bus lines. To determine the mass of the vehicle together with the passengers, a special weighing method was applied. The plus and the minus sign before the slope angle denotes the bus ascending (+ sign) or descending (- sign) a slope.

1.1 Calculation Methodology

During the vehicle movement along the roadway, driving resistances appear which impede vehicle motion, meaning the resistances are in the opposite direction from vehicle motion. Landscape configuration in the pilot area with many ascents and descents results in "negative resistances" which are in the direction of vehicle motion and occur mainly when the vehicle is descending a slope. All "negative resistances" present the possibility for energy regeneration available to vehicles with an alternative drive (hybrid vehicles). In this way, the sum of resistances (R_{SUM}) was calculated which consists of the rolling resistance, aerodynamic resistance, slope

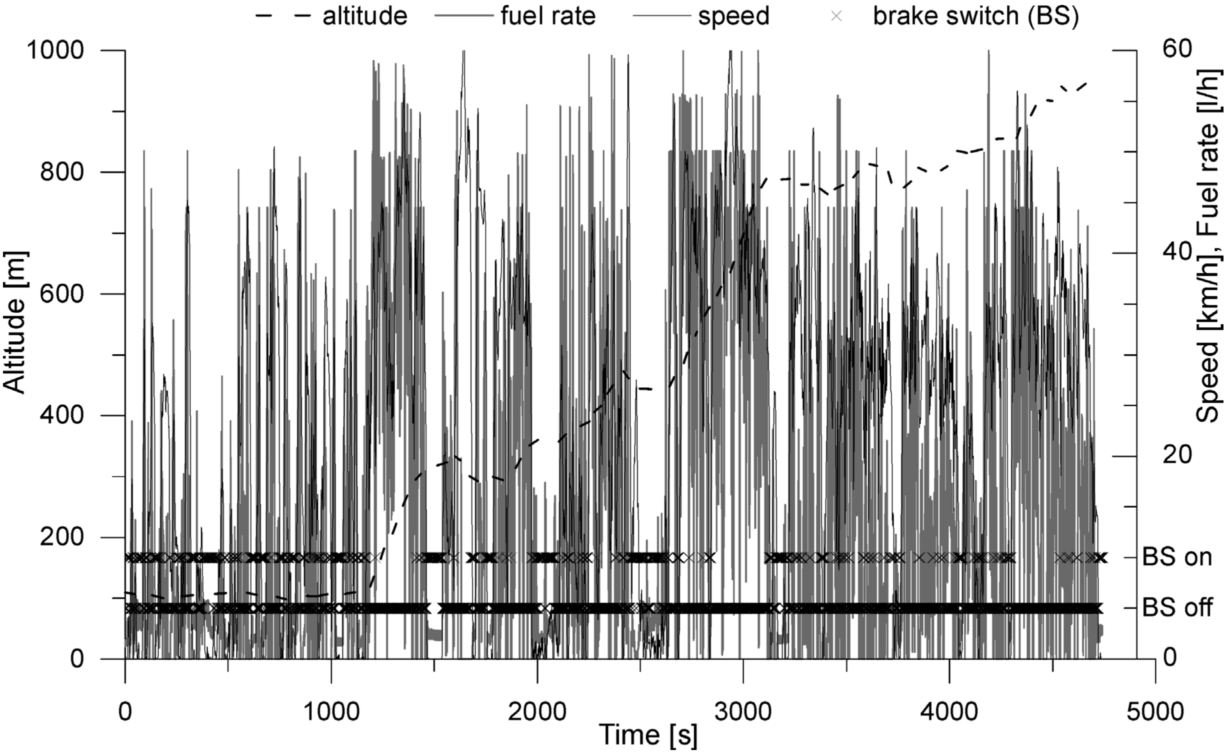

Fig. 5. *Diagram of the measurements performed on Line_6: elevation profile, vehicle speed, fuel rate and brake switch*

resistance and inertia mass resistance. The quantities used in calculation, their symbols and explanations are summarised in Table 2.

1.1.1 Calculation of the Sum of Resistances

The sum of driving resistances on all itinerary segments is calculated as follows:

$$R_{\mathrm{SUM}} = \sum_i (R_{\mathrm{R}i} + R_{\mathrm{A}i} + R_{\mathrm{S}i} + R_{\mathrm{I}i}). \tag{2}$$

The rolling resistance on the i^{th} segment of the observed line is determined as:

$$R_{\mathrm{R}i} = m \cdot g \cdot f \cdot \cos\alpha_i. \tag{3}$$

The aerodynamic resistance on the i^{th} segment of the observed line is calculated as follows:

$$R_{\mathrm{A}i} = \frac{\rho_{\mathrm{A}} \cdot A \cdot (v_i - w_i)^2 \cdot c_{\mathrm{w}}}{2}. \tag{4}$$

The slope resistance on the i^{th} segment is determined by the following equation:

$$R_{\mathrm{S}i} = m \cdot g \cdot \sin\alpha_i. \tag{5}$$

Overcoming the inertia mass resistance on the i^{th} segment of the observed line is calculated as follows:

$$R_{\mathrm{I}i} = \frac{m \cdot \delta \cdot v_i}{t_i}. \tag{6}$$

1.1.2 Total Energy Required to Overcome all the Resistance (TEOR)

$$TEOR = \sum_i ((R_{\mathrm{R}i} + R_{\mathrm{A}i} + R_{\mathrm{S}i}) \cdot (s_i - s_{i-1})) + \sum_j (R_{\mathrm{I}i} \cdot s_j). \tag{7}$$

1.1.3 Calculation Energy Saving Potential of Regenerative Braking (ESPRB)

$$ESPRB = \left(\sum_k TEOR_k + \sum_n (R_{\mathrm{I}n} \cdot s_n) \right) \cdot K_{\mathrm{reg}}. \tag{8}$$

$\sum_k TEOR_k$ is calculated energy saving potential of regenerative braking as the sum of only negative values of the required energy, those who, acting on the basis of the calculated forces of resistance, act in the direction of motion of the vehicle and offer the possibility of regeneration.

$\sum_n (\mathrm{R}_{In} \cdot s_n)$ is calculated regeneration energy only when braking the bus prior to arrival at station point and which is not included in the previous calculation of *TEOR*.

Table 3 presents the comparison of the results obtained from the calculations based on elevation profiles and described equations by taking account of the regeneration coefficient determined through the experimental part measurements performed on Line_6.

2 ANALYSIS OF THE RESULTS AND DISCUSSION

Calculation results for the 10 observed bus lines are presented in Table 3. The analysis of the results shows that the values of all selected lines are widely spread. This is due to different driving regimes on individual lines, which results from different positive and negative slope inclinations. Therefore, the calculations were also made on an annual basis for all bus journeys on the selected bus lines. On all 10 observed lines, 126,540 km are operated per year, which requires 199.4 MWh energy (*TEOR*) to overcome all the

Table 3. *Calculation results and possible regeneration percentage*

Line no.	Distance travelled/ journey [km]	*TEOR*/journey [kWh]	*ESPRB*/journey [kWh]	Distance travelled/ year [km]	*TEOR*/year [kWh]	*ESPRB*/year [kWh]	Rate: *ESPRB*/*TEOR* [%]
1	35	54.61	24.82	12,000	18,203.33	8,273.33	45.45
2	31	49.69	13.48	23,280	37,315.59	10,123.05	27.13
3	23	48.90	5.24	18,900	40,183.04	4,305.91	10.72
4	13	21.59	8.43	5,520	9,167.45	3,579.51	39.05
5	39	39.89	41.10	5,880	6,014.18	6,196.62	103.03
6	31	55.89	9.39	13,600	24,519.48	4,119.48	16.80
7	30	47.77	13.04	26,560	42,292.37	11,544.75	27.30
8	36	47.77	32.00	9,400	12,473.28	8,355.56	66.99
9	36	24.46	44.84	7,200	4,892.00	8,968.00	183.32
10	39	40.72	42.31	4,200	4,385.23	4,556.46	103.90
Summary:				126,540	199,445.96	70,022.66	35.11
Calculation of the ESPRB taking into account total regeneration efficiency (η_{rtot}) = 0.201 - Eq. (1)						14,074.56	7.06

resistances. The *ESPRB* equals 70 MWh, which is 35.11 % of *TEOR* energy. Based on the available data on regeneration efficiency **[12]** and **[13]**, the calculated values are reduced by the total regeneration efficiency η_{rtot}, as shown in Eq. (1). It therefore follows that on the selected bus lines, 14.1 MWh of regenerated *ESPRB* energy could be used on an annual basis, which presents 7.1 % of the TEOR energy needed to overcome all the resistances.

Comparative analyses are also shown in Fig. 6. The results show that the lines with the highest ratio between descents and ascents indicate the highest regeneration rate. It is noted that the best results are obtained from the lines where ascents and descents mostly alternate.

Analyses have also been performed of the amount of emissions in the pilot area on an annual basis, assuming that on all bus routes only diesel and hybrid buses are used (Table 4). The results are based on the measurements of a bus company with a concession in Flanders, Belgium **[17]** and **[18]**, whereby the following average values are taken account of: fuel consumption monitoring, compliance with the applicable emission standards, use of diesel-hybrid buses where possible and use of alternative fuels. Also emphasized is the fact that all bus drivers completed an eco-driving training. The research presented in **[17]** and **[18]** indicates emission values in tank to wheel (TTW) (contrary to well to tank (WTT) or well to wheel ($WTW = WTT + TTW$)) conditions and compares emission values of a conventional diesel bus and hybrid bus. On average, hybrid buses produce 20 % less emissions compared to conventional diesel buses, as shown in Table 4. Analysis of emission values for different hybrid bus technologies is presented in literature **[19]**, whereas literature **[20]** indicates that hybrid buses provide an average of approx. 20 % reduction in GHG emissions compared to conventional diesel buses. The research presented in **[21]** presents the vehicle emission model for road transport that takes account of three models which differ in vehicle interaction with characteristic driving style (especially in regard to vehicle speed) and determined emission values.

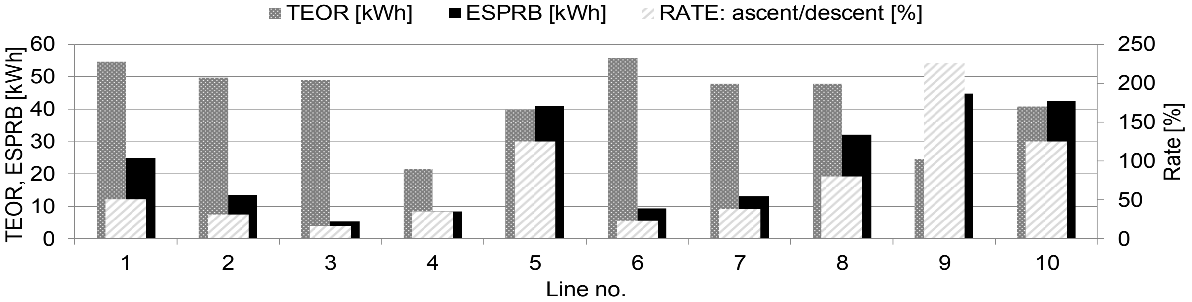

Fig. 6. *Comparison of results obtained on the selected bus lines of the pilot area*

Table 4. *Comparison of results obtained on the selected bus lines of the pilot area*

Line no.	Distance travelled/journey [km]	Distance travelled/year [km]	Conv. diesel CO_2 emission [t]	Conv. diesel PM emission [kg]	Conv. diesel NOx emission [kg]	Hybrid CO_2 emission [t]	Hybrid PM emission [kg]	Hybrid NOx emission [kg]
1	35	12,000	12.68	0.96	144.00	10.15	0.77	115.20
2	31	23,280	24.61	1.86	279.36	19.69	1.49	223.49
3	23	18,900	19.98	1.51	226.80	15.99	1.21	181.44
4	13	5,520	5.83	0.44	66.24	4.67	0.35	52.99
5	39	5,880	6.22	0.47	70.56	4.97	0.38	56.45
6	31	13,600	14.38	1.09	163.20	11.51	0.87	130.56
7	30	26,560	28.07	2.12	318.72	22.47	1.70	254.98
8	36	9,400	9.94	0.75	112.80	7.95	0.60	90.24
9	36	7,200	7.61	0.58	86.40	6.09	0.46	69.12
10	39	4,200	4.44	0.34	50.40	3.55	0.27	40.32
Summary:		126,540	133.75	10.12	1518.48	107.05	8.10	1214.78
Rate of hybrid / conventional diesel:						0.80	0.80	0.80

3 CONCLUSIONS

Based on the aforementioned researches, the following conclusions can be made:

1) The PTA has the obligation to monitor implementation of the public passenger transport by taking account of: fleet properties in the PSO_PPT system, driving mode, landscape configuration, distance travelled, etc. as well as to perform optimization also in the field of energy regeneration and emission reduction in accordance with the applicative European and national guidelines. In order to realize this, the studies presented in this article (Tables 3 and 4) show simulations of such effects.
2) The eligibility of the aforementioned research is based on comparative analyses the results of which indicate that on the selected pilot area, which represents a percentage share of 0.8 % of the overall PSO_PPT operation performed by concessionaire and 0.28 % of the overall PSO_PPT operation performed by all the concessionaires in the Republic of Slovenia.

It should also be taken into consideration that the investment costs of introducing such hybrid buses are according to literature **[19]**, 40 % higher than those for conventional buses. The literature indicates that the operating costs for a conventional diesel bus are 0.82 €/km and for a diesel hybrid bus 0.75 €/km. The replacement costs for the energy storage system are also to be taken into consideration as they account for approximately 25 % of the total operating costs for hybrid buses and 50 % for electric buses. Based on these calculations, it is recommended that additional analyses be made to assess the possibilities of a government or local community subsidized purchase of buses with alternative fuel or hybrid drives.

It is our recommendation that similar and detailed research as well as measurements be continued also in other characteristic areas (high-speed lines, city lines) so as to enable maximum quality of the necessary data. This research presents a basis for the formation of tender specifications in introducing hybrid buses into the public transport in Slovenia. In accordance with the tender specifications, the PTA of Ministry of Infrastructure may require the use of a certain percentage of hybrid buses during the transitional period as well as offer different (financial) incentives to those concessionaires who will purchase hybrid buses and use them in the PSO_PPT system. It is therefore important that the Ministry of Infrastructure takes a position on this matter as soon as possible due to statutory deadlines according to which new concession contracts are to be signed based on prior public tenders in 2019.

4 ACKNOWLEDGEMENT

The research presented in this article has been partly funded by the Slovenian Research Agency as part of the “Modelling in technics and medicine” (code P2-0109 (C)) research programme.

The authors also express their gratitude to the bus company Nomago, d.o.o. (www.nomago.si), who kindly provided the bus and the driver for measurements.

5 REFERENCES

[1] Corazza, M.V., Guida, U., Musso, A., Tozzi, M. (2016). A European vision for more environmentally friendly buses. *Transportation Research Part D: Transport and Environment*, vol. 45, p. 48-63, **DOI:10.1016/j.trd.2015.04.001**.

[2] European Commission, Energy, Climate change, Environment, Climate action, from *https://ec.europa.eu/clima/policies/transport_en*, accessed on 2018-03-30.

[3] Communication from the commission to the European Parliament, the Council, the European Economic and Social Committee and the Committee of the Regions-{SWD(2016) 244 final} (2016). *A European Strategy for Low-Emission Mobility*. European Commission, Brussels.

[4] Ministry of Environment and Spatial Planning: Operational program of measures to reduce greenhouse gas emissions by 2010, from *http://www.mop.gov.si/fileadmin/mop.gov.si/pageuploads/zakonodaja/varstvo_okolja/operativni_programi/optgp2020.pdf*, accessed on 2018-30-3. (in Slovene)

[5] Ranganathan, S (200/). Hybrid buses costs and benefits, from *http://www.eesi.org/files/eesi_hybrid_bus_032007.pdf*, accessed on 2018-04-10, EESI, Washington DC.

[6] Katrašnik, T., Trenc, F., Oprešnik, S.R. (2007). Study of the energy-conversion efficiency of hybrid powertrains. *Strojniški vestnik - Journal of Mechanical Engineering*, vol. 53, no. 10, p. 667-682.

[7] Katrašnik, T. (2010). Fuel economy of hybrid electric heavy-duty vehicles. *Strojniški vestnik - Journal of Mechanical Engineering*, vol. 56, no. 12, p. 791-802.

[8] Cole, D.A. (2016). *The Effectiveness of Energy Storage in Hybrid Vehicles*. University of the West of England, Bristol.

[9] Melo, P., Ribau, J., Silva, C. (2014). Urban bus fleet conversion to hybrid fuel cell optimal powertrains, *Procedia - Social and Behavioral Sciences*, vol. 111, p. 692-701, **DOI:10.1016/j.sbspro.2014.01.103**.

[10] Nurhadi, L., Borén, S., Ny, H. (2014). Advancing from efficiency to sustainability in Swedish medium – sized cities: an approach for recommending powertrains and energy carriers for public transport systems, *Procedia - Social and Behavioral Sciences*, vol. 111, p. 1218-1225, **DOI:10.1016/j.sbspro.2014.03.723**.

[11] Mihály, A., Gáspár, P., Németh, B. (2017). Robust fault-tolerant control of in-wheel driven bus with cornering energy minimization. *Strojniški vestnik – Journal of Mechanical Engineering*, vol. 63, , no. 1, p. 35-44, **DOI:10.5545/sv-jme.2016.3639**.

[12] Ehsani, M., Gao, Y., Gay, S.E., Emadi, A. (2005). *Modern Electric, Hybrid Electric, and Fuel Cell Vehicles*. CRC Press LLC, Boca Raton.

[13] Xiano, B., Lu, H., Wang, H., Ruan, J., Zhang, N. (2017). Enhanced regenerative braking strategies for electric vehicles: Dynamic performance and potential analysis. *Energies*, p. 1-19, **DOI:10.3390/en10111875**.

[14] Zupan, S., Ambrož, M. (2017). *Vehicles*. University of Ljubljana, Faculty of Mechanical Engineering, Ljubljana. (in Slovene)

[15] Ambrož, M., Korinšek, J., Blaž, J., Prebil, I. (2016). Integral management of public transport. *6th Transportation Research Procedia*, vol. 14, p. 382-391, **DOI:10.1016/j.trpro.2016.05.090**.

[16] Surface Vehicle Recommended Practice SAE J1939-71 (2003). Vehicle Application Layer. SAE International, Warrendale.

[17] De Lijn (2018). CO_2-emissions of vehicles, General introduction in figures, from *https://www.delijn.be/en/overdelijn/organisatie/zorgzaam-ondernemen/milieu/co2-uitstoot-voertuigen.html*, accessed on 2018-03-30.

[18] De Lijn (2018). Emissions of our vehicle, from *https://www.delijn.be/en/overdelijn/organisatie/zorgzaam-ondernemen/milieu/uitstoot-voertuigen-delijn.html*, accessed on 2018-03-30.

[19] Lajunen, A. (2014). Energy consumption and cost-benefit analysis of hybrid and electric buses. *Transportation Research Part C: Emerging Technologies*, vol. 38, p. 1-15, **DOI:10.1016/j.trc.2013.10.008**.

[20] Mahmoud, M., Garnett, R., Ferguson, M., Kanaroglou, P. (2016). Electric buses: A review of alternative powertrains, Renewable and Sustainable Energy Reviews, vol. 62, p. 673-684, **DOI:10.1016/j.rser.2016.05.019**.

[21] Hickman, A.J. (1999). *Methodology for Calculating Transport Emissions and Energy Consumption. Project Report SE/491/98*. Transport Research Laboratory, Berkshire.

Strojniški vestnik - Journal of Mechanical Engineering 65(2019)1, 21-30
© 2019 Journal of Mechanical Engineering. All rights reserved.
DOI:10.5545/sv-jme.2018.5620
Original Scientific Paper
Received for review: 2018-07-02
Received revised form: 2018-10-20
Accepted for publication: 2018-11-05

Impact Forces Occurring in a Forced Damped Multi-Body System with Clearances

Guillaume Ricciardi
CEA, Alternative Energies and Atomic Energy Commission, France

The purpose of this paper is to study the effect of clearance and other parameters on the maximal impact forces likely to occur in a forced multi-body system. Numerical simulations are performed for a large range of parameters. The numerical results showed three regions. In the first one, there is no contact between the bodies. The second one, defined as the smooth region, is characterized by regular evolution with a concentration of the impact forces at the boundaries. In the last one, where the most important impact forces are met, the system shows chaotic behaviours and coincides with the lower values of clearance. Theoretical upper bounds for the maximal forces are proposed and compared to numerical results. In the smooth region, the criterion is respected, but in the chaotic region, some discrepancies are observed. Nevertheless, the criterion gives a good estimation. The dimensionless analysis showed that the maximal impact force is proportional to the mass, the acceleration, the stiffness ratio and the inverse of the damping ratio.

Keywords: multi-body, impact, clearance, damping

Highlights

- *A forced multibody system with high damping is investigated.*
- *Numerical simulations are performed for a large range of parameters.*
- *This study focuses on the maximal impact force encoutered.*
- *Analytical upper bounds for the maximal force encoutered are proposed.*

0 INTRODUCTION

Mechanical systems involving several components separated by clearances can be encountered in many engineering fields as energy [**1**], automobile [**2**] or space industry [**3**]. When subjected to an external excitation, impacts occur between the components and the force resulting from these impacts may cause damages. The impact forces strongly depend on the clearance [**4**] and increase with contact stiffness [**5**] and the number of clearances [**6**]. The nonlinear system gives rise to chaotic behaviours with a large variety of transitions between chaotic and periodic behaviours using clearance as a parameter [**7**]. This complexity is illustrated by [**8**] and [**9**]: they propose maps using clearance and excitation frequency as parameters showing the number of impacts within a period: it appears that the more complex behaviours are obtained for lower values of clearance. Some have proposed an analytical analysis of bifurcations [**10, 11**] and showed discontinuity in bifurcation maps. Transitions between chaotic and periodic solutions have been widely studied on many nonlinear mechanical systems, such as pendulum [**12**], tank filled with water [**13**], disk brake [**14**], or cracked rotor [**15**].

This study is applied to a liquid metal fast breeder nuclear reactor core. This core is made of clamped-free slender structures immersed in a liquid as described in [**16**]. In case of a seismic event the impact force generated by the contact between bodies can be damaging; therefore, knowing the maximal force occurring in case of an earthquake is fundamental to making a proper design. The purpose of this paper is to study the effect of clearance and other parameters on the maximal impact forces likely to occur in a forced multi-body system. A dimensionless expression of the dynamic equation is proposed, and numerical simulations are performed for a large range of parameters, assuming that the slender structures only vibrate on their first natural bending mode.

1 METHODOLOGY

Let us consider the simple system composed of Nm bodies of mass M attached to the ground by a spring K and a viscous damping C, the displacement of the ground u_e is imposed as in a seismic event, and the displacement of each body i is noted u_i (Fig. 1). The bodies are separated by a clearance e, and when a contact is detected impact forces, F_{li} and F_{ri} are imposed either on the left or the right of the body. The equation of motion of each body i is given by:

$$M\frac{\partial^2 u_{di}}{\partial t^2}+C\frac{\partial u_{di}}{\partial t}+Ku_{di}=-M\frac{\partial^2 u_e}{\partial t^2}+F_{li}+F_{ri}, \quad (1)$$

---

*Corr. Author's Address: CEA, Cadarache, 13108 Saint Paul lez Durance, France, guillaume.ricciardi@cea.fr where u_{di} is the relative displacement:

$$u_{di} = u_i - u_e. \tag{2}$$

The impact forces are modelled by linear springs K_c when the contact is detected to account for the stiffness contact that can be different from the stiffness of the system. Different models can be found to account for the contact between bodies, by the continuity of the displacements or the velocities when the contact is detected or with nonlinear stiffness given by the Hertz theory. In the present study, a linear spring is chosen to account for the local deformation of the slender body at the contact location which is much higher than the bending stiffness K. This is a very critical parameter that can completely change the behaviour of the structure.

$$\forall i \in [2:Nm], F_{li} = \begin{cases} \frac{K_c}{2}\left(u_{di-1} - u_{di} - e\right) \\ \text{if } \left(u_{di-1} - u_{di} - e\right) > 0, \\ \\ 0 \\ \text{if } \left(u_{di-1} - u_{di} - e\right) < 0, \end{cases} \tag{3}$$

$$\forall i \in [1:Nm-1],$$

$$F_{ri} = \begin{cases} -\frac{K_c}{2}\left(u_{di} - u_{di+1} - e\right) \\ \text{if } \left(u_{di} - u_{di+1} - e\right) > 0, \\ \\ 0 \\ \text{if } \left(u_{di} - u_{di+1} - e\right) < 0, \end{cases} . \tag{4}$$

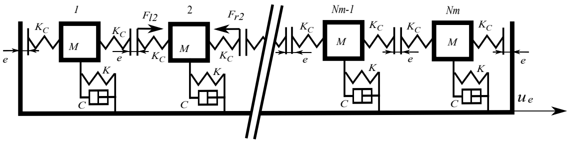

Fig. 1. *Multi-body system with clearances*

The acceleration of the ground is assumed harmonic at the frequency f and for an amplitude of a_0:

$$\frac{\partial^2 u_e}{\partial t^2} = a_0 cos(2\pi f t). \tag{5}$$

In the following, the dimensionless equations are established based on the following dimensionless quantities:

$$f_0 = \frac{1}{2\pi}\sqrt{\frac{K}{M}}, \tag{6}$$

$$f_r = \frac{f}{f_0}, \tag{7}$$

$$f_c = \frac{K_c}{K}, \tag{8}$$

$$\varepsilon = \frac{C}{2\sqrt{KM}}, \tag{9}$$

$$t_r = f_0 t, \tag{10}$$

$$e_r = \frac{4\pi^2 f_0^2 e}{a_0}, \tag{11}$$

$$u_{ri} = \frac{4\pi^2 f_0^2 u_{di}}{a_0}, \tag{12}$$

$$v_{ri} = \frac{\partial u_{ri}}{\partial t_r}, \tag{13}$$

$$F_{lri} = \frac{F_{li}}{Ma_0\sqrt{f_c}}, \tag{14}$$

$$F_{rri} = \frac{F_{ri}}{Ma_0\sqrt{f_c}}. \tag{15}$$

Thus the equations of the system become:

$$\begin{aligned} \frac{1}{4\pi^2}\frac{\partial^2 u_{ri}}{\partial t_r^2} &+ \frac{\varepsilon}{\pi}\frac{\partial u_{ri}}{\partial t_r} + u_{ri} = -cos(2\pi f_r t_r) \\ &+ \sqrt{f_c}F_{lri} + \sqrt{f_c}F_{rri}, \end{aligned} \tag{16}$$

$$\forall i \in [2:Nm],$$

$$F_{lri} = \begin{cases} \frac{\sqrt{f_c}}{2}\left(u_{ri-1} - u_{ri} - e_r\right) \\ \text{if } \left(u_{ri-1} - u_{ri} - e_r\right) > \\ 0, \\ 0 \\ \text{if } \left(u_{ri-1} - u_{ri} - e_r\right) < 0, \end{cases} \tag{17}$$

$$\forall i \in [1:Nm-1],$$

$$F_{rri} = \begin{cases} -\frac{\sqrt{f_c}}{2}\left(u_{ri} - u_{ri+1} - e_r\right) \\ \text{if } \left(u_{ri} - u_{ri+1} - e_r\right) > 0, \\ \\ 0 \\ \text{if } \left(u_{ri} - u_{ri+1} - e_r\right) < 0, \end{cases} \tag{18}$$

The response of the system is totally defined by the stiffness ratio f_c, the number of bodies Nm, the damping ratio ε, the reduced clearance e_r and the reduced frequency imposed to the system f_r.

To observe the dependency of impact forces on dimensionless parameters, a parametric study is performed numerically (Table 1). The range studied corresponds to the different situations and configurations encountered in the seismic response of reactor cores. For each set of parameters (f_c, Nm, ε, e_r, and f_r), a temporal numerical simulation is performed with an explicit time scheme for 1000 periods. For the present study over 430,000 simulations have been performed. For each simulation we note F_m the maximal impact force in time and space:

$$F_m = max\left(F_{rri}(t_{rj}), F_{lri}(t_{rj})\right)_{\forall(i,j)} . \tag{19}$$

In the following, most of the results shown are accounting for a damping ratio of 50 % which will be the default value without indication. In this paper, only high values of damping are considered because while it makes the simulations simpler because the harmonic regime is reached faster, these high values are commonly encountered in the industry especially with structures surrounded by fluid [**17**].

Table 1. *Parameters range used for numerical simulations*

f_c	Nm	ε	e_r	f_r
1 to 2000	1 to 20	10 to 50	1 to 6	1 to 5

2 GENERAL BEHAVIOUR

For each couple of Nm and f_c, Fig. 2 shows the maximal reduced impact force F_m as a function of f_r and e_r. Different behaviours can be observed, but three zones can be identified. The first one corresponds to F_m = 0, which means that there is no impact either because the reduced gap is too high or because the frequency is too far from resonance. The second zone corresponds to $e_r > 0.3$ and will be referred to as the smooth zone. In that zone the force F_m shows a regular evolution with a maximum around f_r = 1 close to the natural frequency of the system; this zone seems to show an identical trend for every (Nm, f_c) couple. The third zone, referred to as a chaotic zone for $e_r < 0.3$, shows irregular evolution and can be very different depending on the (Nm, f_c) couple. This zone shows the highest values of F_m.

The limits of the noimpact zone can be easily estimated considering the response of a single body with no interaction, of which the modulus is given by:

$$|u_0| = \frac{1}{\sqrt{(1-f_r^2)^2 + 4\varepsilon^2 f_r^2}} . \tag{20}$$

It can be seen that the previous equation (red curve) fits the smallest values of F_m in Fig. 3.

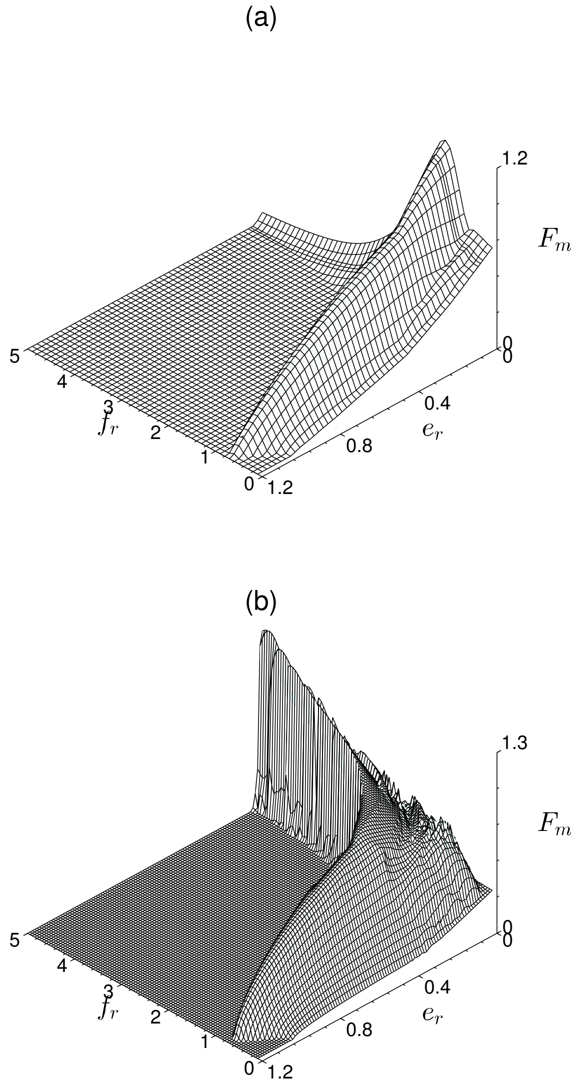

Fig. 2. *Maximal reduced impact force as function of e_r and f_r, for Nm = 3 and f_c = 3 (a), for Nm = 3 and f_c = 100 (b)*

Figs. 4 to 7 show the evolution of F_m as a function of the reduced clearance for two reduced frequencies and various (Nm, f_c) couples. In the smooth region, close to the natural frequency at f_r = 1, F_m shows an asymptotic behaviour as Nm and f_c increase. At lower frequencies the behaviour is different, F_m does not depend on the number of bodies Nm, but it decreases as the stiffness ratio f_c increases. For lower e_r, the only clear trend is for lower frequencies where F_m increases with Nm whereas it decreases when f_c increases. For other frequencies, one can see strong fluctuations.

The chaotic behaviour is more important for higher values of f_c.

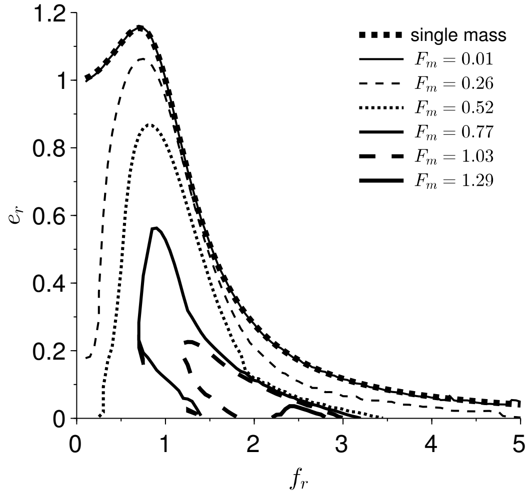

Fig. 3. *Iso F_m curves for Nm = 5 and f_c = 60, with the theoretical response of a single mass (thick dotted curve)*

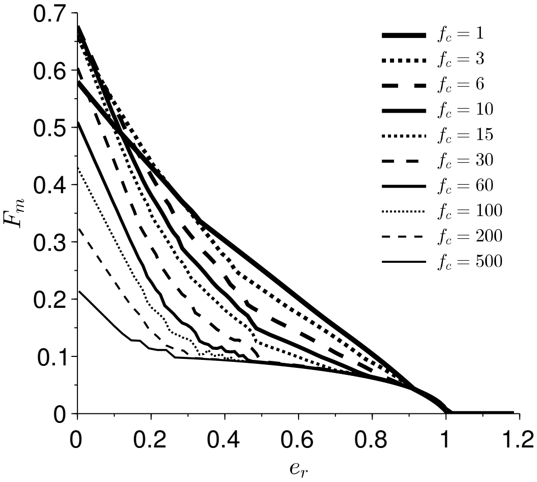

Fig. 4. *Maximal reduced impact force as a function of e_r for Nm = 5 and various f_c for f_r = 0.1*

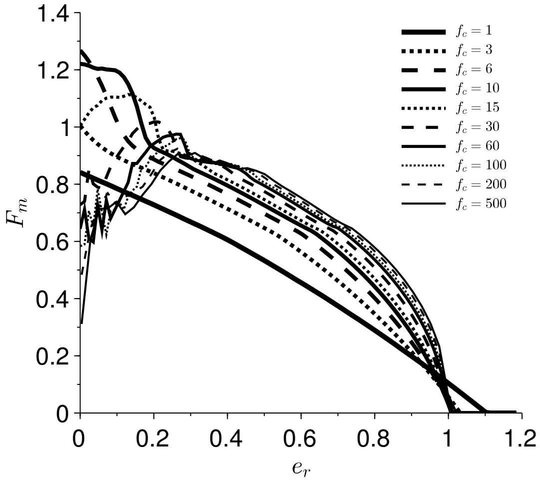

Fig. 5. *Maximal reduced impact force as a function of e_r for Nm = 5 and various f_c for f_r = 1*

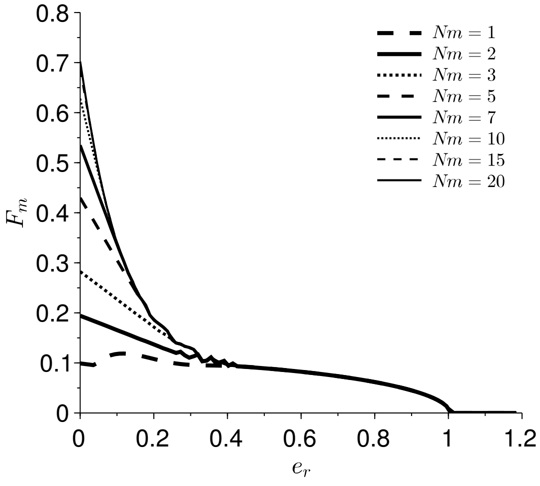

Fig. 6. *Maximal reduced impact force as a function of e_r for f_c = 100 and various Nm for f_r = 0.1*

Fig. 8 shows the evolution of the spatial distribution of F_m close to the natural frequency as a function of e_r. It can be seen that in the smooth region ($e_r > 0.3$) only a few masses at the extremities are in contact. As e_r decreases, the system goes in the chaotic region, and the number of bodies in contact increases to reach a state in which all bodies are in contact, and comparable values of impact forces are seen.

The evolution of F_m as a function of frequency (Fig. 9) shows the difference between a non-chaotic (f_c = 10) and chaotic behaviour (f_c = 100). In the first one, the impact forces are always located at the extremities with a regular spatial evolution, whereas in the second one the maximal values can be located anywhere, and disturbed spatial evolution is shown.

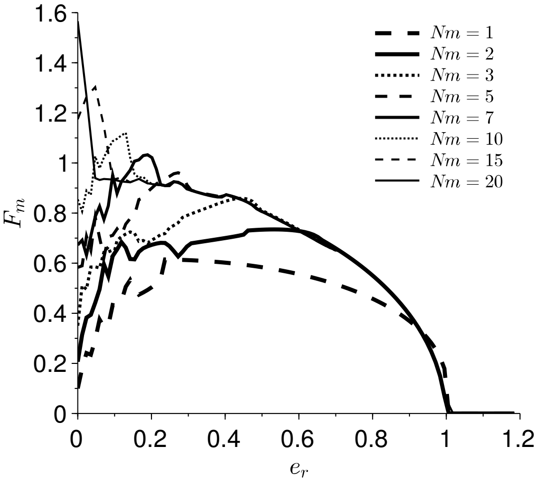

Fig. 7. *Maximal reduced impact force as a function of e_r for f_c = 100 and various Nm for f_r = 1*

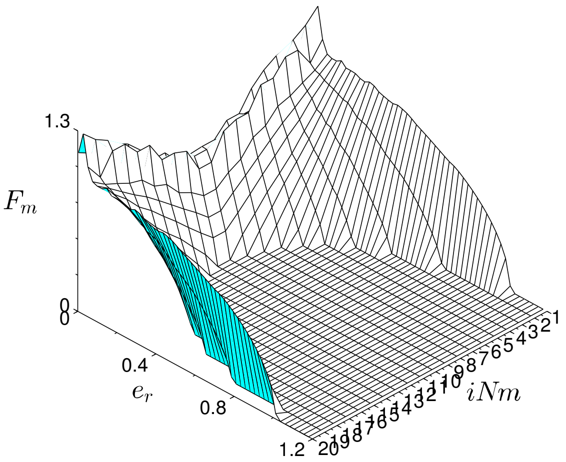

Fig. 8. *Maximal reduced impact force spatial distribution as function of e_r for Nm = 20, f_r = 1 and f_c = 200*

3 SMOOTH REGION

In the smooth region, the maximal impact force is obtained at the natural frequency (f_r = 1) with a small shift toward higher frequencies when f_c increases for lower values of e_r (Fig. 10). At a given f_c, F_m quickly converges as Nm increases, for e_r = 0.24 the results do not change after Nm = 5, and for higher values of e_r, the asymptotic value is reached for Nm = 2 (Fig. 11).

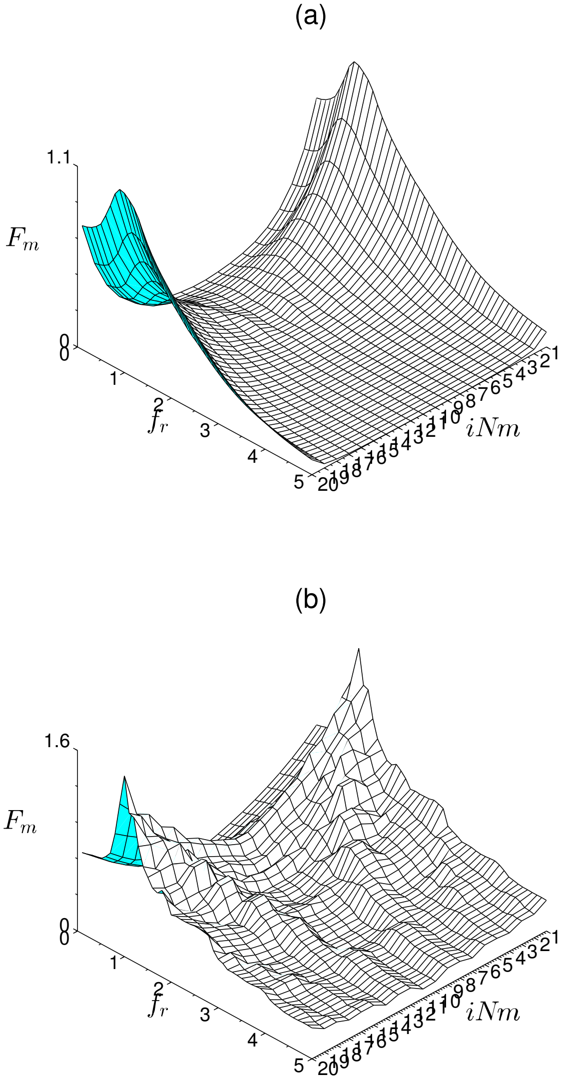

Fig. 9. *Maximal reduced impact force spatial distribution as function of f_r for Nm = 20, e_r = 0 and f_c = 1 (a), f_c = 100 (b)*

When only a few bodies show contact the number of bodies in contact does not depend on the total number of contact and explain why the asymptotic value is quickly reached.

Fig. 12 shows the influence of damping ratio on the maximal impact force; it can be seen that as this ratio decreases, the force increases and that the transitions between chaotic and smooth regions are

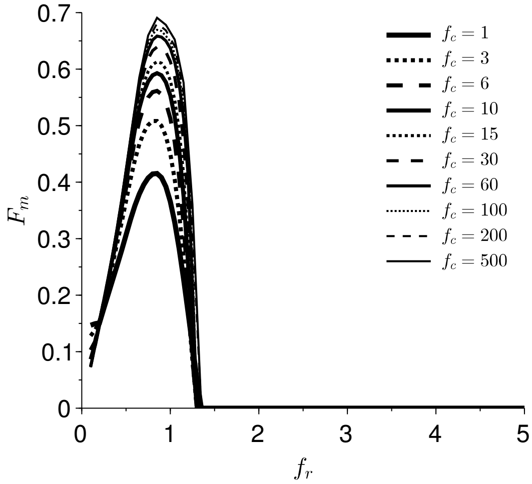

Fig. 10. *Maximal reduced impact force as function of f_r for Nm = 5 and various f_c for e_r = 0.71*

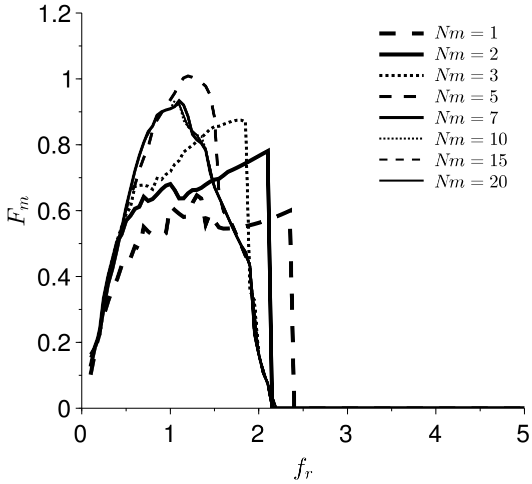

Fig. 11. *Maximal reduced impact force as function of f_r for f_c =1 00 and various Nm for e_r = 0.24*

shifted toward higher values of e_r. This is an expected results, since the damping dissipates energy.

Based on the latter observations, one could assume that the maximal impact force in the smooth region is given by the oscillation of a mass at the extremities in contact with the wall.

This system has a natural frequency f_1:

$$f_1 = \sqrt{1+f_c}. \tag{21}$$

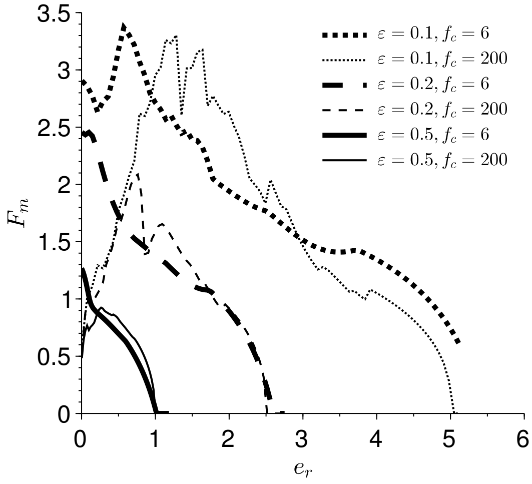

Fig. 12. *Maximal reduced impact force as a function of e_r at f_r = 1 for various ε, and for Nm = 5 and various f_c*

The maximum amplitude u_m is given by:

$$u_m = \frac{1}{2\varepsilon\sqrt{1+f_c-\varepsilon^2}}. \tag{22}$$

The force is given by the compression of the spring K_c, in the dimensionless form it gives for the maximal force:

$$\begin{aligned} F_m &= \sqrt{f_c}u_m, & (23)\\ &= \frac{1}{2\varepsilon}\sqrt{\frac{f_c}{1+f_c-\varepsilon^2}}. & (24) \end{aligned}$$

Thus, the maximal force F_m depends on the stiffness ratio f_c and the damping ratio ε. One can extract from the previous equation an upper bound depending only on ε:

$$F_m < \frac{1}{2\varepsilon}. \tag{25}$$

The observation of the numerical results shows that the criterion (25) is always verified on the range studied in this paper (Table 2). This result illustrates the importance of damping ratio on the impact forces.

Table 2. *Maximum F_m in the smooth region for various damping*

ε	0.1	0.2	0.3	0.5
F_m	3.75	2.46	1.45	0.93
$\frac{1}{2\varepsilon}$	5	2.5	1.66	1

4 CHAOTIC REGION

The bifurcation diagram of the first body in Fig. 13 illustrates the diversity of behaviour met by the nonlinear system. It switches from periodic solution to period-doubling bifurcation between $2.2 < f_r < 2.55$ and chaos between $2.55 < f_r < 2.7$. Then it returns to a periodic solution between $2.7 < f_r < 3.2$ and chaos $3.2 < f_r < 3.55$ and again a period-doubling bifurcation between $3.55 < f_r < 4.15$. Each change of regime is characterized by a significant modification of F_m.

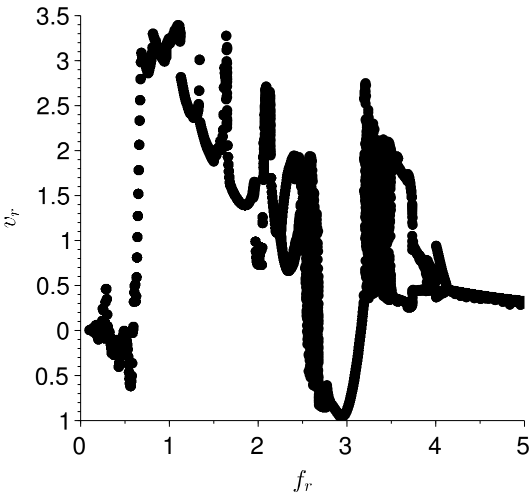

Fig. 13. *Bifurcation diagram using f_r as control parameter for Nm = 5 and f_c = 60 and for e_r = 0.06*

Fig. 14 shows the maximal reduced impact forces for a small value of e_r in the chaotic region. It can be observed that, unlike in the smooth region F_m reaches its maximum values for various frequencies depending on Nm and f_c; this frequency increases with f_c but decreases as Nm increases. Moreover, a very irregular evolution of F_m as a function of the reduced frequency with abrupt decreases can be seen. The maximal impact forces obtain in the chaotic region are much more important than in the smooth region.

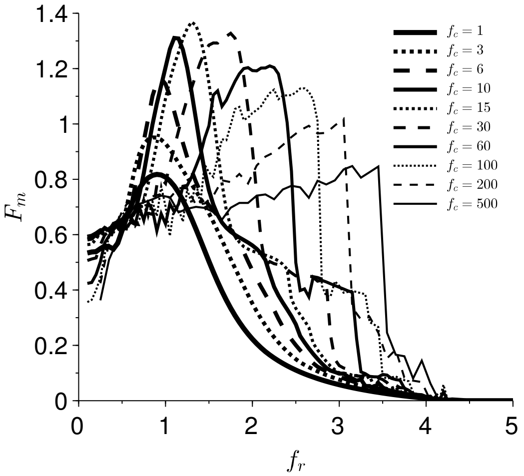

Fig. 14. *Maximal reduced impact force as function of f_r for Nm = 5 and various f_c, for e_r = 0.06*

The example of F_m distribution in Fig. 15 shows that the forces may not be concentrated at the extremities and, in some cases, the maximum can be reached elsewhere.

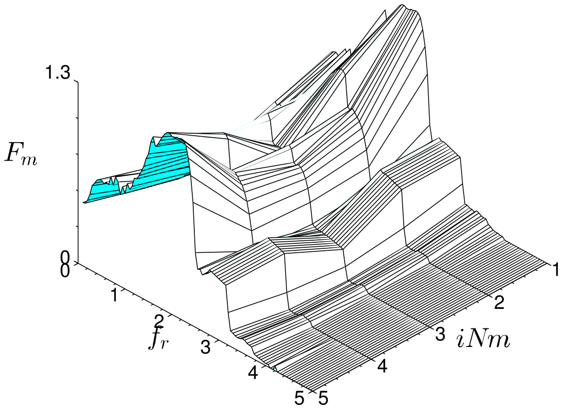

Fig. 15. *Maximal reduced impact force spatial distribution as a function of f_r for Nm = 5, f_c = 60 and e_r = 0.06*

5 LINEAR SYSTEM

Let us consider the linear system without any gap. Since a simple analytical expression of the natural frequencies seems out of reach an approximation is proposed:

$$f_{k_a} = \sqrt{1+f_c\left(\frac{k}{Nm}\right)^2\left(a-b\left(\frac{k}{Nm}\right)^c\right)}, \quad (26)$$

$$a = 4.935, \quad (27)$$

$$b = 2.935, \quad (28)$$

$$c = 1.81. \quad (29)$$

This approximation gives a good estimation of the calculated natural frequency with an error of less than 1 % for f_1 and less than 3 % for other natural frequencies on alarge range of values of f_c and Nm.

The approximated f_1 tend to 1 as Nm tends to infinity, and approximation gives the higher natural reduced frequency:

$$f_{Nm} = \sqrt{1+2f_c}, \quad (30)$$

which is exact in the case of Nm = 1.

Let us define the reduced frequency:

$$f_{r1} = \frac{f_r}{f_{1_a}}. \quad (31)$$

Plotting F_m as a function of f_{r1} (Fig. 16) shows that all the curves reach their maximum values at the same reduced frequency. Thus, we can conclude from this observation that the maximum impact forces are obtained when the system behaves like a linear system oscillating at its first natural frequency. As observed previously, the impact forces increases when the damping ratio decreases (Fig. 17); moreover, for lower values of ε the peaks due to second and third linear natural modes can be observed.

The maximal displacement of the first body on the first natural mode of the linear system is given by:

$$u_{1m} = \frac{1}{2\varepsilon\sqrt{f_1^2-\varepsilon^2}}\Phi_1(1), \quad (32)$$

where Φ_1 is the shape of the first natural mode and given by the eigenvectors of $\mathbf{K_I}$.

Let us assume that the first natural mode is close to a sinus distribution:

$$\Phi_1(i) \approx sin\left(\frac{\pi i}{Nm}\right) \quad (33)$$

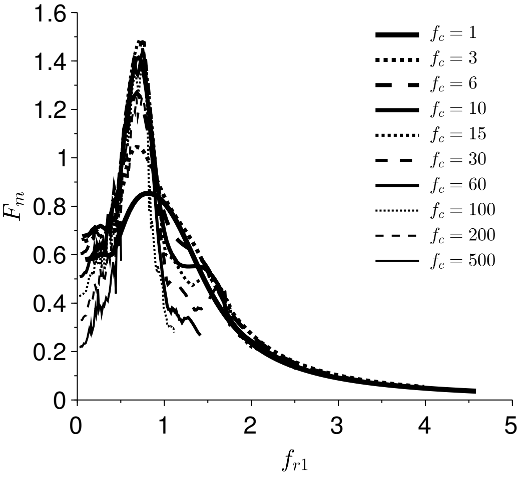

Fig. 16. *Maximal reduced impact force as function of f_{r1} for e_r = 0 and various f_c for Nm = 5.*

Assuming that Nm is high enough one can make the approximation:

$$\Phi_1(1) \approx \frac{\pi}{Nm}. \quad (34)$$

Thus we can finally obtain an approximation of the maximal impact force:

$$F_m = \sqrt{f_c}u_{1m}, \quad (35)$$

$$F_m = \frac{\pi}{2\varepsilon Nm}\sqrt{\frac{f_c}{1+\frac{f_c}{Nm^2}\left(4.935-\frac{2.935}{Nm^{1.81}}\right)-\varepsilon^2}}, \quad (36)$$

with an upper bound:

$$F_m < \frac{\pi}{2\varepsilon\sqrt{4.935}}. \quad (37)$$

Table 3 shows that the upper bound gives a good estimation of the maximal impact force but failes to give a conservative value.

Table 3. *Maximum F_m in the chaotic region for various damping*

ε	0.1	0.2	0.3	0.5
F_m	7.02	3.88	2.65	1.86
$\frac{\pi}{2\varepsilon\sqrt{4.935}}$	7.07	3.54	2.35	1.41

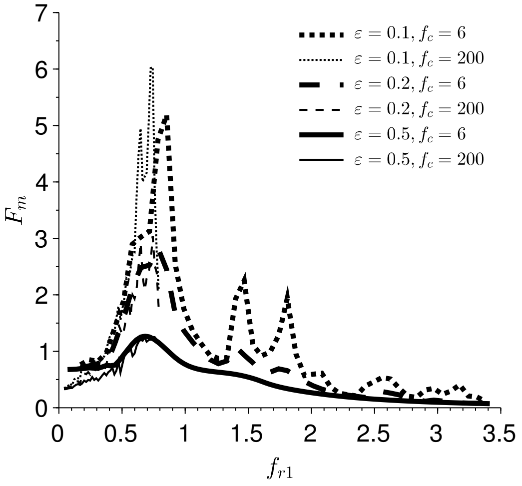

Fig. 17. *Maximal reduced impact force as function of f_{r1} at e_r = 0 for various ε, and for Nm = 5 and various f_c*

6 COMPARISON WITH EXPERIMENT

The experiment described in [**16**] presents a row of 46 slender structures called fuel assemblies positioned vertically and clamped at their foot on a shaking table. The structures are likely to vibrate on their first natural bending mode, the clearance between structures is 3.5 mm, and a seismic spectrum of about 10 m/s^2 is applied. The impact forces are measured; it has been shown that the maximal forces are located at the extremities as in the present study. Table 4 shows the dimensionless parameters of the experiment. It can be observed that the maximal reduced impact force encountered F_m = 0.52 is much lower than the one estimated in the theoretical analysis F_m = 7.02; thus, the simplified analysis seems to give a conservative upper bound. Nevertheless, this difference can be explained by the fact that each body is not a one-degree-of-freedom system, and some energy can be dissipated in higher modes, and the excitation in the experiment is not harmonic; thus, some transient effects are likely to occur.

Table 4. *Experimental parameters*

ε	N_m	f_c	e_r	F_m
0.1	46	559	0.22	0.52

7 CONCLUSION

The numerical results showed three regions. In the first one, there is no contact between the bodies. The second one defined as the smooth region is characterized by regular evolution with a concentration of the impact forces at the boundaries. In the last one, where the most important impact forces are met, the system shows chaotic behaviours, and coincide with the lower values of clearance. In the smooth region the criterion is respected, but in the chaotic region, some discrepancies are observed. Nevertheless, the criterion gives a good estimation. The dimensionless analysis showed that the maximal impact force is proportional to the mass, the acceleration, the stiffness ratio and the inverse of the damping ratio. Theoretical upper bounds for the maximal forces are proposed and compared to numerical and experimental results.

It would be interesting in further study to evaluate the effect of non homogeneous clearances and stiffness and nonlinear contact stiffness to be more representative of real life systems. In further studies a multi beam system will be studied and compared to the present results.

8 NOMENCLATURE

u_i	displacement, [m]
u_e	ground displacement, [m]
u_{di}	relative displacement, [m]
M	mass, [kg]
C	damping, [kg.s^{-1}]
K	stiffness, [N.m^{-1}]
K_c	contact stiffness, [N.m^{-1}]
t	time, [s]
e	clearance, [m]
F_{ri}	right contact force, [N]
F_{li}	left contact force, [N]
F_{rri}	reduced right contact force,
F_{lri}	reduced left contact force,
u_{ri}	reduced relative displacement,
f	ground frequency, [Hz]
f_0	natural frequency, [Hz]
a_0	ground acceleration amplitude, [m.s^{-2}]
f_r	reduced frequency,
f_c	stiffness ratio,
ε	damping ratio,
t_r	reduced time,
e_r	reduced clearance,
N_m	number of bodies,
F_m	maximal reduced impact force.

9 REFERENCES

[1] Ricciardi, G., Bellizzi, S., Collard, B., Cochelin, B. (2009). Row of fuel assemblies analysis under seismic loading: Modelling and experimental validation. *Nuclear Engineering and Design*, vol. 239, no. 12, p. 2692-2704, **DOI:10.1016/j.nucengdes.2009.08.029**.

[2] Wei, D., Wang, Y., Jiang, T., Zheng, S., Zhao, W., Pan, Z. (2017). Chaos vibration of pinion and rack steering trapezoidal mechanism containing two clearances. *Mechanical Systems and Signal Processing*, vol. 92, p. 146-155,**DOI:10.1016/j.ymssp.2017.01.019**.

[3] Zhang, J., Guo, H-W., Liu, R-Q., Wu, J., Kou, Z-M., Deng, Z-Q. (2016). Nonlinear dynamic characteristic analysis of jointed beam with clearance. *Acta Astronautica*, vol. 129, p. 135-146, **DOI:10.1016/j.actaastro.2016.09.009**.

[4] Bai, Z.F., Sun, Y. (2016). A study on dynamics of planar multi-body mechanical systems with multiple revolute clearance joints. *European Journal of Mechanics A/Solids*, vol. 60, p. 95-111, **DOI:10.1016/j.euromechsol.2016.06.009**.

[5] Varney, P., Green, I. (2015). Nonlinear phenomena, bifurcations, and routes to chaos in an asymmetrically supported rotor-stator contact system. *Journal of Sound and Vibration*, vol. 336, p. 207-226, **DOI:10.1016/j.jsv.2014.10.016**.

[6] Li, Y., Chen, G., Sun, D., Gao, Y., Wang, K. (2016). Dynamic analysis and optimization design of a planar slider-crank mechanism with flexible components and two clearance joints. *Mechanism and Machine Theory*, vol. 99, p. 37-57, **DOI:10.1016/j.mechmachtheory.2015.11.018**.

[7] Rahmanian, S., Ghazavi, M.R. (2015). Bifurcation in planar slider-crank mechanism with revolute clearance joint. *Mechanism and Machine Theory*, vol. 91, p. 86-101, **DOI:10.1016/j.mechmachtheory.2015.04.008**.

[8] Luo, G.W., Lv, X.H., Shi, Y.Q. (2014). Vibro-impact dynamics of a two-degree-of freedom periodically-forced system with a clearance: Diversity and parameter matching of periodic-impact motions. *International Journal of Non-Linear Mechanics*, vol. 65, p. 173-195, **DOI:10.1016/j.ijnonlinmec.2014.04.013**.

[9] Wang, Z., Luo, T. (2017). Multiformity of periodic-impact motions of a harmonically forced soft-impacting system and experimental verification based on an electronic circuit. *Chaos, Solitons and Fractals*, vol. 94, p. 23-36, **DOI:10.1016/j.chaos.2016.11.004**.

[10] Liu, Y., Wang, Q., Xu, H. (2017). Analytical determination of bifurcations of periodic solution in three-degree-of-freedom vibro-impact systems with clearance. *Chaos, Solitons and Fractals*, vol. 99, p. 141-154, **DOI:10.1016/j.chaos.2017.04.002**.

[11] Liu, Y., Wang, Q., Xu, H. (2017). Bifurcations of periodic motion in a three-degree-of-freedom vibro-impact system with clearance. *Communications in Nonlinear Science and Numerical Simulation*, vol. 48, p. 1-17, **DOI:10.1016/j.cnsns.2016.12.018**.

[12] de Paula, A.S., Savi, M.A., Pereira-Pinto, F.H.I. (2006). Chaos and transient chaos in an experimental nonlinear pendulum. *Journal of Sound and Vibration*, vol. 294, no. 3, p. 585-595, **DOI:10.1016/j.jsv.2005.11.015**.

[13] Krasnopolskaya, T.S., Shvets, A.Y. (2009). Dynamical chaos for a limited power supply for fluid oscillations in cylindrical tanks. *Journal of Sound and Vibration*, vol. 322, no. 3, p. 532-553 **DOI:10.1016/j.jsv.2008.09.007**.

[14] Wei, D., Ruan, J., Zhu, W., Kang, Z. (2016). Properties of stability, bifurcation, and chaos of the tangential motion disk brake. *Journal of Sound and Vibration*, vol. 375, p. 353-365, **DOI:10.1016/j.jsv.2016.04.022**.

[15] Leng, X., Meng, G., Zhang, T., Fang, T. (2007). Bifurcation and chaos response of a cracked rotor with random disturbance. *Journal of Sound and Vibration*, vol. 299, no. 3, p. 621-632, **DOI:10.1016/j.jsv.2006.07.006**.

[16] Asayama, T., Kitamura, S., Morishita, M., Fontaine, B. (1999). JNC/CEA Collaborative work on core seismic study -SYMPHONY- Simulation of one-row mock-uo tests with restrained configuration. *Transaction of the 15th International Conference on Structural Mechanics in Reactor Technology*, paper C03/01.

[17] Ladouceur, B., Woillez, J., Fontaine, M. (2004). Fuel assembly damping for accident studies: an analytical approach. *Structural behaviour of fuel assemblies for water cooled reactors, Proceedings of a technical meeting*, p. 271-278.

[18] Kerschen, G., Golinval, J.C., Vakakis, A., Bergman, L. (2005). The method of proper orthogonal decomposition for dynamical characterization and order reduction of mechanical systems: an overview. *Nonlinear Dynamics*, vol. 41, no. 1-3, p. 147-169, **DOI:10.1007/s11071-005-2803-2**.

[19] Graham, M.D., Kevrekidis, I.G. (1996). Alternative approaches to the Karhunen-Love decomposition for model reduction and data analysis. *Computers Chemical Engineering*, vol. 20, no. 5, p. 495-506, **DOI:10.1016/0098-1354(95)00040-2**.

[20] Païdoussis, M.P., Sarkar, A., Semler, C. (2005). A horizontal fluid-conveying cantilever: spatial coherent structures, beam modes and jumps in stability diagram. *Journal of Sound and Vibration*, vol. 280, no. 1-2, p. 141-157, **DOI:10.1016/j.jsv.2003.12.026**.

[21] Bellizzi, S., Sampaio R. (2006). POMs analysis of randomly vibrating systems obtained from Karhunen-Loève expansion. *Journal of Sound and Vibration*, vol. 297, no. 3-5, p. 774-793, **DOI:10.1016/j.jsv.2006.04.023**.

Strojniški vestnik - Journal of Mechanical Engineering 65(2019)1, 31-40
© 2019 Journal of Mechanical Engineering. All rights reserved.
DOI:10.5545/sv-jme.2018.5384
Original Scientific Paper
Received for review: 2018-03-30
Received revised form: 2018-10-17
Accepted for publication: 2018-11-13

Deteriorated Indoor Environmental Quality as a Collateral Damage of Present Day Extensive Renovations

Mateja Dovjak[1,*] – Jan Slobodnik[1] – Aleš Krainer[2]
[1]University of Ljubljana, Faculty of Civil and Geodetic Engineering, Slovenia
[2]Institute of Public and Environmental Health, Slovenia

Optimal indoor environmental quality (IEQ) is especially important in every living and working environment with present vulnerable population groups. Especially problematic are educational institutions, where prolonged exposure time of users additionally increases health risks. The present study is focused on the problem of deteriorated IEQ in renovated kindergarten. The problem was critically assessed from the aspects of indoor air quality (IAQ) and energy use. A combination of simulations of the selected IAQ parameters and building energy use was performed for five sets of scenarios, where required and recommended design ventilation rates variated according to Slovenian legislation. Characteristics of actual kindergarten in central Slovenia, renovated in 2016, were used for simulations. Concentrations of CO_2 and formaldehyde were calculated in two model playrooms with CONTAM 3.2, whereas building energy use was calculated for two thermal zones of playrooms with Energy Plus 8.0.0. If ventilation in playrooms was designed according to the minimal permissible value (air changes per hour) ACH 0.5, CO_2 concentrations exceeded the national maximum permissible level by 2.5 and 3 times, and formaldehyde concentrations was close to the value recommended by World Health Organisation (WHO) and exceeded the level recommended by National Institute for Occupational Safety and Health (NIOSH-CDC) by 4.6 and 4.5 times. All required and recommended design ventilation rates resulted in exceeded values of CO_2 above recommendation for category I of IAQ, except the design ventilation rate 55 m^3/h per person. In-line with public health protection measures, relevant information is an aid for recommendation definitions for policies and strategies towards healthier indoor environments as well as for raising awareness about current design practice.

Keywords: kindergarten, energy renovation, air quality, ventilation rate

Highlights

- *Our study shows that minimal permissible value, ACH 0.5, results in the highest concentration of CO_2 in both playrooms that exceeded the national maximum permissible level for acceptable indoor air quality by 2.5 times and 3 times. Formaldehyde concentrations in both playrooms reached almost the value recommended by WHO and exceeded the level recommended by NIOSH by 4.6 and 4.5 times.*
- *We proved that only design ventilation rates that take into account the expected number of occupants result in optimal air quality for category I spaces.*
- *Results show that increase of design ventilation rates from 0.5 ACH to 55 m^3/h per person results in 8.2 times and 6.8 times lower CO_2 concentrations and 22.8 times and 17.6 times lower formaldehyde concentrations; on the other hand, building energy use without recuperation was increased by 5.67 times and 6.68 times and with recuperation by 1.81 times and 2.08 times, compared to the reference 0.5 ACH without recuperation.*

0 INTRODUCTION

The stock of buildings in Europe is relatively old, with more than 40 % of it built before 1960 and 90 % before 1990. About 75 % of buildings are energy inefficient and, depending on the individual Member State, 0.4 % to 1.2 % of the stock is renovated each year **[1]**. From January, 1st 2014, 3 % of the total floor area of buildings owned by central government must be renovated each year **[2]**. According to Energy act in the Republic of Slovenia **[3]**, the European requirement is applied also to educational institutions owned by self-governing local communities and public sector.

The present day extensive renovations are going in wrong direction: towards narrow-minded measures with air tightened building, thermally well-insulated envelope, and highly energy efficient mechanical systems. Such non-holistic approach is in fact stimulated by implemented legal requirements on energy efficiency that allow the use of minimal permissible values for ventilation, while other defined requirements and recommendations are as a rule not taken into the consideration. For example, the minimal value of volume air changes per hour (ACH) for working and living spaces at the time when occupants are present is 0.5 1/h (Article 8) **[4]**. Such low ventilation rates have been associated with statistically significant worsening of occupants` health outcomes **[5]**.

Optimal indoor environmental quality (IEQ) is especially important in every living and working environment with vulnerable population groups. Especially problematic are educational institutions,

---

*Corr. Author's Address: University of Ljubljana, Faculty of Civil and Geodetic Engineering, Jamova cesta 2, 1000 Ljubljana, Slovenia, mdovjak@fgg.uni-lj.si

such as kindergartens and schools as well as health-care facilities, where prolonged exposure times of users increase health risks. Our study focuses on a kindergarten, where several epidemiological studies identify deteriorated indoor air quality (IAQ) as the most problematic field of IEQ. Until now, numerous pollutants have been detected in indoor air of kindergartens, in which primary air quality indicator, CO_2 presents the most researched one. Araújo-Martins et al. [6] and Mainka and Zajusz-Zubek [7] highlight that CO_2 levels often exceed the required and recommended limit values above 1800 mg/m^3 (1000 ppm). Especially high concentrations have been associated with low efficiency of ventilation systems. For example, the average measured CO_2 in Portuguese daycare centres was 3846±662 mg/m^3 (2137±368 ppm); in preschool buildings in Poland it was above 1800 mg/m^3 (1.000 ppm) [6] and [7]. Butala and Novak [8] performed a study on energy consumption and potential energy savings in 24 school buildings in Slovenia. On average, the total energy consumption per school building was 192 kWh/(m^{2}a), and the maximal concentration of CO_2 was above 7198 mg/m^3 (4000 ppm). Dovjak and Pajek [9] holistically assessed indoor environmental quality of 24 playrooms in 17 publicly funded children daycare centres in Slovenia. The results showed that the most critical field was the indoor air quality, where in 63 % of playrooms the average CO_2 exceeded the required value, 3000 mg/m^3 (1667 ppm).

In terms of origin and removal processes, besides CO_2 there are also other important pollutants related to IAQ in kindergarten. Study in 5 kindergartens in Hong Kong [10] detected flame retardants, $PM_{2.5}$, carbonyls and black carbon. The researchers concluded that the evaluated indoor air pollution might present adverse effects to children, where the most problematic were $PM_{2.5}$ and formaldehyde levels. Study in 25 daycare centres in Seoul [11] evaluated biological (mould and bacteria) and chemical pollutants (formaldehyde, CO_2, CO, and total volatile organic compounds). The concentrations were associated with building age and environmental factors such as ventilation time. Important source of indoor pollution that has to be considered in the design process is outdoor pollution in relation to location sources. Higher concentrations of benzene and NO_2 were quantified in 18 schools and kindergartens in Central-Southern Spain located in industrial as well as in rural areas [12]. Additionally, the location of heavy traffic areas were associated with increased exposure to polycyclic aromatic hydrocarbons, detected in indoor air of 27 kindergartens of Sabzevar city, Iran [13].

Educational facilities present 17 % of total floor area and account to 12 % of the final energy use in non-residential buildings in Europe [14]. The educational facilities in Slovenia accounted to 2131 TJ of the final energy use in 2008 (i.e. 33 % of the total final energy use in buildings of the public sector). Slovenian kindergartens accounted to 255 TJ of the final energy use in 2008, the specific final energy use was 241 kWh/m^2 in 2008 [15]. The main reason for high energy use is related to reciprocal effect of imperfections separately on the level of building envelope and systems. To attain optimal IAQ in kindergartens, much higher ventilation rates are needed than in other general environments. Many studies have showed that the increased ventilation rates result in higher ventilation losses and overall building energy use, approximately 2 % to 20 %, depending on the specific building and technology parameters [16] and [17]. Since energy crisis in 1970ies, various technologies and systems that can reduce energy use and costs in buildings have been defined. Hekmat et al. [18] showed that total energy use can be reduced by 9 % to 21 % by using mechanical ventilation systems with heat recovery, compared to comparable examined strategies. Deng et al. [19] focused on the ventilation rate of a ground-source heat pump system from the perspective of energy saving and indoor thermal comfort combined. Their findings provide guidelines for reducing power consumption while improving thermal comfort levels. Beside active systems, a passive design strategy, such as wind-driven ventilation, was used to increase indoor air velocity in naturally ventilated buildings [20]. Several authors recommend to define measures from the perspective of energy saving and IEQ combined. Despite scientific findings, current practice is still based on non-holistic measures, in the direction of improvements of building envelope or mechanical systems separately, besides decreased ventilation rates.

This study is focused on the problem of deteriorated IEQ in renovated kindergartens in Slovenia. The main purpose of our study was to critically assess the relevant problem with comparative analysis of indoor air quality and energy use. A combination of simulations of selected parameters of IAQ and building energy use was performed for five sets of scenarios, where design ventilation rates variated according to national legislation [4]. Actual kindergarten in central Slovenia, renovated in 2016, was used for simulations. Concentrations of CO_2 and formaldehyde were calculated in two model playrooms (age groups 1 and 2) with CONTAM version 3.2. Annual energy use for heating (i.e. building net energy for heating) was calculated for two thermal zones in playrooms with Energy Plus 8.8.0. Research questions were: 1. What is the impact of various design ventilation rates on CO_2 and formaldehyde concentrations? 2. How do design ventilation rates affect building energy use? 3. Which is the optimal design ventilation rate according to target users, room purpose and its specifics, resulting in optimal IEQ and simultaneously minimal possible energy use? In-line with public health protection measures, relevant information is an aid for recommendation definitions for policies and strategies towards healthier indoor environments as well as for raising awareness in current design practice.

1 METHODS

Three-dimensional model of the selected parts of an actual building was established according to the provided floor plans and technical description of the building. It is a multi-story building (4345.4 m^3, 1289.6 m^2) that consists of a ground floor, first floor and attic. Story height varies between 2.5 m to 3.1 m. Slope degree of the pitch roof is 28 %.

Exterior wall of the building is composed of reinforced concrete with polystyrene thermal insulation and façade plaster (U_{wall} 0.60 W/(m^{2}K)). Ventilated roof is composed of reinforced concrete, mineral wool thermal insulation and covered with Al sheet (U_{roof} 0.16 W/(m^{2}K)). Concrete slab floor construction is composed of polystyrene sound insulation, screed and wooden flooring (U_{floor} 0.96 W/(m^{2}K)). Windows are south oriented triple glazing with PVC frame (window area 11 m^2, wall area 18.1 m^2, WWR 0.60 m^2, U_{window} 1.06 W/(m^{2}K)).

For the simulation of IAQ indicators two different ventilation zones (i.e. playroom A for age group 2: 42.0 m^2, 126.84 m^3; playroom B for age group 1: 32.5 m^2, 98.80 m^3) were selected. For simulation of energy use two thermal zones were considered, located at the ground floor (i.e. six playrooms for age group 2: 252.0 m^2, 761.0 m^3), and first floor (i.e. six playrooms for age group 1: 195.0 m^2 , 592.8 m^3) (Fig. 1, Table 1).

Table 1. *Characteristics of analysed model playrooms*

Characteristics	Playroom A (3 to 6 years)	Playroom B (1 to 2 years)
V_z [m^3]	126.84	98.80
A_z [m^2]	42.0	32.50
A_{window} [m^2]	69.6	69.6
WWR	0.54	0.55
U_{window} [W/(m^{2}K)]	1.06	1.06
$\tau_{\text{ao v}}$ [-]	0.46	0.46
U_{wall} [W/(m^{2}K)]	0.60	0.60
Infiltration [1/h]	0.30	0.30
$V_{\text{in,d}}$ [m^3/h]	250	250
$V_{\text{out,d}}$ [m^3/h]	250	250
Furniture load [m^2], No. pieces	11.25 m^2 (5 tables), 26 chairs, 12 m^2 (1 bookcase), 11 m^2 (5 cabinets)	6.75 m2 (3 tables), 16 chairs, 12 m^2 (1 bookcase), 11 m^2 (5 cabinets)
Product specific emission [mg/h] [21]	0.94 mg/h (5 tables) 3.25 mg/h (chairs) 1.00 mg/h (1 bookcase) 0.69 mg/h (5 cabinets)	0.50 mg/h (3 tables) 2.25 mg/h (chairs) 1.00 mg/h (1 bookcase) 0.69 mg/h (5 cabinets)

V_z zone volume, A_z net occupant floor area of the ventilation zone, A_{window} window area, WWR window to wall ratio, U_{window} thermal transmittance of window, $\tau_{\text{ao v}}$ glass visible transmittance, U_{wall} thermal transmittance of wall, $V_{\text{in,d}}$ designed inlet air volume flow, $V_{\text{out,d}}$ designed outlet air volume

2.1 Simulation of Indoor Air Quality

Indoor air quality was analysed by a multizone indoor air quality and ventilation analysis program CONTAM 3.2 [22]. It enables the calculation of contaminant concentrations in model room by various airflow rates and by a variety of processes including emissions from building materials, human metabolism and personal exposure. CO_2 and formaldehyde concentrations (CO_2, CH_2O) were calculated by steady state method in two model playrooms: playroom A for age group 2 (ground floor); playroom B for age group 1 (first floor) (Table 2). CO_2 and CH_2O were presented in units mg/m^3 and ppm, where conversion equation is based on

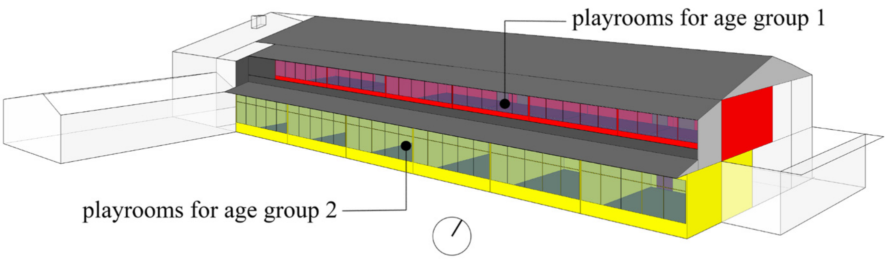

Fig. 1. *Three-dimensional model with analysed ventilation zones and thermal zones*

25 ºC and 101.3 kPa. Background outdoor CO_2, 719.8 mg/m³ (400 ppm) were assumed for calculations.

Validation of the model was based on an actual set of measurements performed in a classically built and prefabricated kindergarten, both subunits of our analysed building (i.e. six measuring days, time periods approximately 8:30 to 10:30, 10:00 to 12:00). The evaluated parameters in two selected playrooms (age group 2) were: number of occupants and their activity, status of window and its opening time, ventilation rate and concentration of CO_2 in 10 minutes time step. Beside measured levels, CO_2 was calculated in both playrooms for every time step according to the real time influential evaluated parameters.

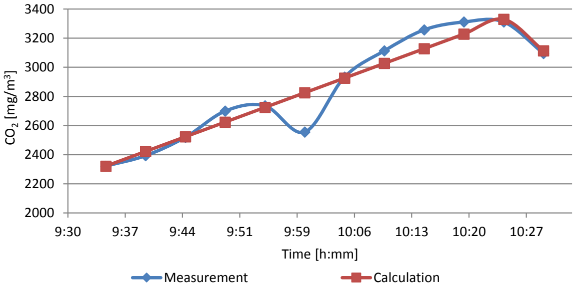

Fig. 2. *Measured and calculated CO_2 for measuring day No.6, playroom in classically built kindergarten*

CO_2 metabolic generation rate coefficients variated according to the actual activity of children. Fig. 2 presents the comparison between measured and calculated CO_2 concentration in playroom of the classically built kindergarten for one measuring day. 9 children and 2 teachers were present during our measurement. In the time period 9:35 to 10:30, 0.24 L/min CO_2 generation rate was assumed. Ventilation rate was 19.8 m³/h (8:30 to 10:25) and 118 m³/h (10:25 to 10:30).

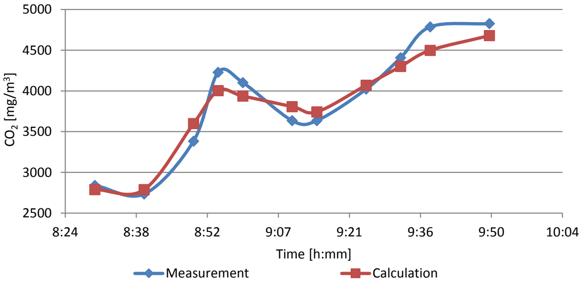

Fig. 3. *Measured and calculated CO_2 for measuring day No. 3, playroom in prefabricated kindergarten*

Fig. 3 presents the comparison between measured and calculated CO_2 concentration in the prefabricated playroom for one measuring day. 15 children and 2 teachers were present during our measurement. In the time period 8:30 to 8:50, 0.35 L/min CO_2 generation rate was assumed and in the time period 8:50 to 9:50, 0.15 L/min. In the time periods 8:30 to 8:55 and 9:25 to 9:50 the ventilation rate was 28.2 m³/h and for 9:00 to 9:15, 44 m³/h (small window opened).

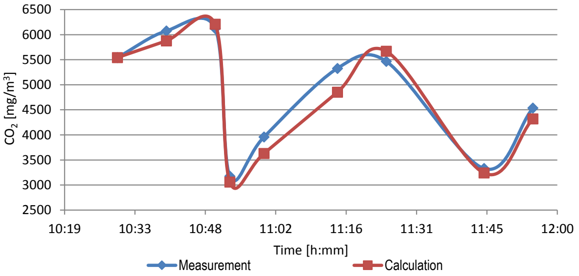

Fig. 4. *Measured and calculated CO_2 concentration for measuring day No. 1, playroom in classically built kindergarten*

Fig. 4 presents the comparison between measured and calculated CO_2 concentration in playroom of the classically built kindergarten for one measuring day. 14 children and 2 teachers were present during our measurement (0.24 L/min CO_2 generation rate). In the time periods 10:53 to 11:00 and 11:45 to 11:55, maximal ventilation rate 810.0 m³/h was attained, due to opened windows and door (no children, 0 L/min CO_2 generation rate). The average ventilation rate was 256 m³/h.

Characteristics of model playrooms and subjects are presented in Tables 1 and 2, respectively.

Table 2. *Characteristics of subjects in analysed model playrooms*

Model playroom /subject characteristic	Playroom A	Playroom B
No. of subjects	24 children 2 educators	14 toddlers 2 educators
Age of children [years]	3 to 6	1 to 2
CO_2 metabolic emission rate [L/s] **[23]**	Children: 0.0029, Educators: 0.0052	
$M_{children}$ [W/m²] **[24]**	Sitting, crawling: 78.5, Sleeping: 46.6	
A_{du} [m²]	0.69	0.51

Detailed methodology and results are described in Dovjak et al. **[25]** and Pirc **[26]**. Results of our measurements showed nearly complete correlation with calculated CO_2 for all measuring days. Measured average CO_2 deviated from calculated values by 11.8 mg/m³ in prefabricated kindergarten and 12.6 mg/m³ in classical built kindergarten.

To answer the research questions, we performed five sets of scenarios, where the required and

Table 3. *List of required and recommended design ventilation rates for playrooms in kindergarten [4]*

Sets of scenarios	Required and recommended design ventilation rate	Playroom A: calculated required and recommended outdoor airflow	Playroom B: calculated required and recommended outdoor airflow
1	Minimal ACH: 0.5/h	63.42 m^3/h	49.40 m^3/h
2	Minimal volume of air for person: 8.7 m^3/hm^2	365.4 m^3/hm^2 (2.9 ACH)	282.8 m^3/hm^2 (2.9 ACH)
3	Minimal outdoor air intake: 15 m^3/h per person	390.0 m^3/h (3.1 ACH)	240.0 m^3/h (2.4 ACH)
4	Minimal air volume: 10.1 m^3/hm^2	424.2 m^3/h (3.3 ACH),	328.3 m^3/h (3.3 ACH)
5	Air volume: 55 m^3/h per person	1430.0 m^3/h (11.3 ACH)	880.0 m^3/h (8.9 ACH)

recommended design ventilation rates varied according to the values from national legislation **[4]** (Table 3).

To calculate CH_2O, we took into account typical wooden furnishing in compliance with E1 class (0.124 mg/m^3) **[27]**. According to data **[21]** and **[28]**, we assumed product specific emissions (Table 1). The calculated CO_2 and CH_2O were compared to the required and recommended values. According to national Rules **[4]**, the permissible value of CO_2 in indoor air is 3000 mg/m^3 (1667 ppm). Recommended CO_2 concentration for the design and assessment of energy performance in buildings with spaces occupied by vulnerable population groups - category I is 630 mg/m^3 (350 ppm) above background outdoor concentration **[29]**. ANSI/ASHRAE Standard 62.1 **[30]** defines that CO_2 concentration should not exceed 2500 ppm (4499 mg/m^3), while 1000 ppm is the recommended value (1800 mg/m^3). A short-term (30 min) guideline of 0.1 mg/m^3 (0.081 ppm) CH_2O is recommended by World Health Organisation, WHO **[31]**. National Institute for Occupational Safety and Health **[32]** recommends 0.0196 mg/m^3 (0.016 ppm) time weighted average (TWA) exposure.

2.2 Simulation of Energy Use

Energy use was simulated for five sets of scenarios with energy analysis and thermal load simulation program EnergyPlus 8.8.0 **[33]**. The building model was created by graphical user interface OpenStudio. Building and mechanical system configurations and conditions were defined according to actual data.

Energy indicators were calculated for thermal zones of six playrooms for age group 1 (i.e. set point temperature, 24 °C) and six playrooms for age group 2 (22 °C): overall building energy use for heating, i.e. building net energy for heating (kWh/(m^2a)), transmission heat losses (kWh/(m^2a)), ventilation heat losses (kWh/m^2a), solar heat gains (kWh/(m^2a)) and internal heat gains (kWh/(m^2a)). Calculation was based on yearly method. Additionally, the increase ratio of ventilation heat losses was calculated for five sets of scenarios with and without recuperation. It presented the ratio of heat losses by ventilation for considered set of scenarios regarding the reference design ventilation rate, 0.5 ACH, without recuperation.

3 RESULTS

3.1 Air Quality

Fig. 5 presents the calculated CO_2 in model playrooms A and B for five sets of scenarios, where the required and recommended design ventilation rates varied according to national legislation. The calculated CO_2 includes background outdoor concentration 719.8 mg/m^3 (400 ppm). In playroom A, the highest CO_2 was reckoned up in scenario 1 with ACH 0.5 (8891 mg/m^3, 4941 ppm) (Fig. 5), while the lowest CO_2 was in scenario 5 with 55 m^3/h per person (1082 mg/m^3, 601 ppm). Similar findings were obtained in playroom B, scenario 1, where ACH 0.5 resulted in the highest CO_2 (7408 mg/m^3, 4116 ppm). In both playrooms for scenario 1 with ACH 0.5, the calculated CO_2 exceeded the required and recommended values **[4]**, **[29]** and **[30]** by 3 and 2.5 times.

Higher design ventilation rates (15 m^3/h per person, 10.1 $m^3/(hm^2)$, 55 m^3/h per person, 8.7 $m^3/(hm^2)$) resulted in lower CO_2. Only design ventilation rates that take into account the expected number of occupants (55 m^3/h per person) resulted in optimal air quality for category I spaces **[29]**.

Similar findings can be obtained in case of calculated CH_2O. The highest CH_2O was calculated in scenario 1 with ACH 0.5 (playroom A: 0.091 mg/m^3, 0.074 ppm; playroom B: 0.088 mg/m^3, 0.072 ppm) (Fig. 6). The lowest CO_2 was calculated in scenario 5 with 55 m^3/h per person (playroom A: 0.004 mg/m^3, 0.003 ppm; playroom B: 0.005 mg/m^3, 0.004 ppm). If ventilation in a playroom is designed according to the minimal permissible value ACH 0.5, the calculated CH_2O almost reached the values recommended by WHO **[31]** and exceeded the level recommended by

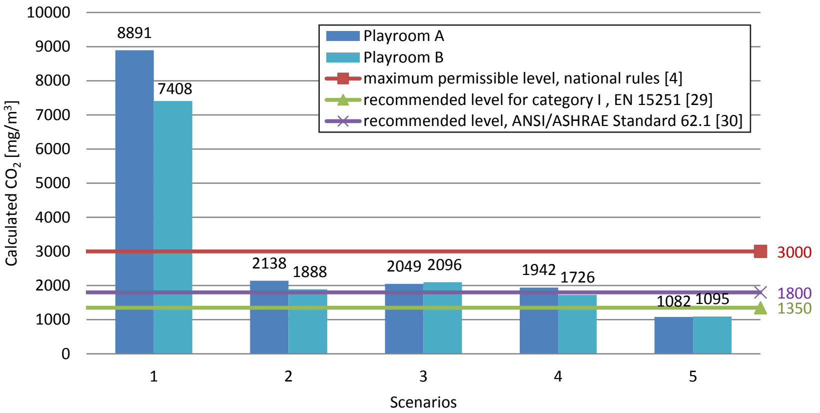

Fig. 5. *Calculated CO_2 [mg/m³, ppm] in analysed model playrooms for five sets of scenarios*

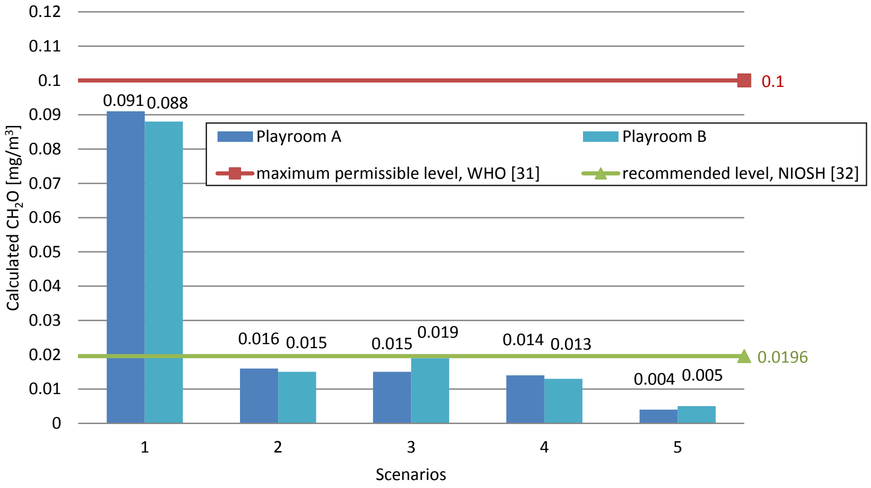

Fig. 6. *Calculated CH_2O [mg/m³, ppm] in analysed model playrooms for five sets of scenarios*

NIOSH by 4.6 (playroom A) and 4.5 times (playroom B) [32].

3.2 Energy Use

Table 4 presents the calculated values of annual energy use for heating, heat gains and losses for two thermal zones and reference scenario 1 (0.5 ACH).

As it was shown in the analysis of IAQ indicators, the design ventilation rate 55 m³/h per person (scenario 5) resulted in the highest level of IAQ in both playrooms. Consequently, this resulted in proportionally higher heat losses by ventilation 285.76 kWh/(m²a) (or overall energy use for heating 325.50 kWh /(m²a)) in playroom age group 1 and 292.99 kWh/(m²a) (or overall energy use 285.40 kWh /(m²a)) in playroom age group 2. Increase ratio between scenarios 5 and 1 is 5.67 and 6.68 (Table 5). However, in case of application of recuperation in scenario 5, the heat losses for ventilation were 91.28 kWh /(m²a) (or overall energy use 131.40 kWh/(m²a)) in playrooms age group 1 and 91.10 kWh/(m²a) (or overall energy use 90.10 kWh/(m²a)) in playroom age group 2. Therefore, the increase ratio was only 1.81 and 2.08 compared to scenario 1, 0.5 ACH without recuperation.

The application of recuperation resulted in minimal change in heat losses for ventilation between scenarios 4 and 5, which was 31.40 kWh/(m²a) for playroom age group 1 and 41.50 kWh/(m²a) for playroom age group 2, with increase ratios 1.60 and 1.84, respectively.

Therefore, the determination of required design ventilation rate must provide primarily, the highest level of IAQ and secondly lower energy use. Minimisation of energy use should be achieved besides by strict hygienic requirements and maintenance also with local recuperation and other efficient systems. Savings

Table 4. *Annual energy use for heating, components of heat gains and losses [kWh/(m²a)] for thermal zones and scenario 1*

Thermal zone	Energy use for heating [kWh/(m²a)]	Heat gains [kWh/(m²a)]		Heat losses [kWh/(m²a)]	
		Interior	Solar	Transmission	Ventilation
Playrooms age group 1	77.50	28.20	10.70	80.10	50.40
Playrooms age group 2	43.30	58.30	39.00	118.9	43.90

Table 5. *Annual heat loss by ventilation for thermal zone of playrooms for five sets of scenarios [kWh/(m²a)]*

Thermal zone / Sets of scenarios	Playrooms age group 1		Playrooms age group 2	
	Heat loss by ventilation [kWh/(m²a)]	Increase ratio* [-]	Heat loss by ventilation [kWh/(m²a)]	Increase ratio* [-]
1	50.40	1.00	43.86	1.00
2	117.69	2.34	100.70	2.30
3	103.68	2.06	105.31	2.40
4	128.89	2.56	109.92	2.51
5	285.76	5.67	292.99	6.68

* According to the reference design ventilation rate (0.5 ACH) without recuperation.

with achieving physiological minimums should not be allowed!

4 DISCUSSION

The problem of deteriorated IEQ in renovated public and residential buildings has been highlighted in epidemiological studies [6], [7] and [34], as well as pointed out by building users. Poor indoor air quality presents one of the most expanded indicator of inadequate indoor environment and is recognized as the leading health risk factor in built environment. WHO [35] reported that 4.3 million people a year die because of the exposure to indoor air pollution.

Decision making in current design practice is often directed towards reducing energy losses through the instrument of minimal permissible values of ventilation rate. We have critically assessed the impact of variations in design ventilation rate on the selected air quality indicators, CO_2 and CH_2O. Concentration of a main bioeffluent and indicator of air quality CO_2, varies according to the rates of occupancy and design ventilation. The highest concentration was in playroom A (8891 mg/m³, 4941 ppm) and playroom B (7408 mg/m³, 4116 ppm) with scenario 1, 0.5 ACH. According to national rules, the calculated CO_2 exceeded the required value of 3000 mg/m³ (1667 ppm) by 3 times (in playroom A) and 2.5 times (in playroom B). However, Bakó-Biró et al. [36] reported that even lower levels of CO_2 concentrations, compared to these required concentrations, may lead to occupant dissatisfaction and decreased productivity. In order to protect particularly vulnerable population groups, optimal and not the lowest permitted values for acceptable indoor air quality have to be used. Thus, recommended CO_2 concentration for category I spaces occupied by vulnerable population groups is 630 mg/m³ (350 ppm) above background outdoor concentration [29]. All required and recommended design ventilation rates resulted in values of CO_2 above recommendation, except 55 m³/h per person.

In the European Union, formaldehyde is classified under category 1B carcinogen [37]. Acute and chronic inhalation exposure to formaldehyde in humans can result in eye, nose and throat irritation, respiratory symptoms, exacerbation of asthma, and sensitization [31]. Our study highlighted that design of buildings on minimal permissible values 0.5 ACH results in concentration that reaching almost the limit value for formaldehyde 0.1 mg/m³ (0.081 ppm) [31] in both playrooms, which can cause irritation of sensitive people after 30 min of exposure [31]. Additionally, CH_2O exceeded the recommended limit level by NIOSH [32] by 4.6 (playroom A) and 4.5 times (playroom B). Besides that, the calculated CH_2O at 0.5 ACH reaches the odour threshold for formaldehyde, 0.0614 mg/m³ to 1.23 mg/m³ (0.05 ppm to 1.0 ppm). According to ANSI/ASHRAE Standard 62.1-2010 [38], the calculated CH_2O exceeded the concentration of 0.0331 mg/m³ (0.027 ppm, 8 h, CARB), which might cause irritation in sensitive individuals. Reaching 0.0614 mg/m³ to 1.29 mg/m³ (0.05 ppm to 1.05 ppm) might lead to neurophysiological health effects [39].

Despite, current design practice, European standards provide different approach [40]. For example, EN 15251 [29] defines the design criteria for I-IV categories of indoor environment. The required ventilation rates are based on health and comfort criteria and expressed in three ways: 1. calculated for people and building components, 2. calculated per person or per square meter floor area or 3. based on a mass balance and CO_2 level. Similarly, SIST CR 1752 **[41]** that presents the basic standard for the national Rules on ventilation **[4]** defines the design criteria for A-C categories. Moreover, several researchers concluded that optimal ventilation rates that result in the decreased health related outcomes (i.e. expressed per person), are much higher than those recommended in standards or required by law. For example, literature review of 41 studies **[5]** showed that ventilation rates below 10 L/s per person in office buildings were associated with statistically significant worsening in one or several health or perceived air quality outcomes. Carrer et al. **[42]** estimated the lowest ventilation rates with no adverse effects for respiratory symptoms, asthma or allergy symptoms, airborne infectious diseases or acute health symptoms, to be about 6 L/s to 7 L/s per person. In terms of effects on short-term absence rates and performance and learning, these minimum rates are much higher, ranging from 16 L/s to 24 L/s per person.

Standards often guide designers as follows: “When national regulations do not decide it, the designer shall make his own decision and report it”. And consequently, due to economic and energetic pressures, they often select lower levels, which might “work” in general environments (i.e. living room, offices), but are not accepted in other indoor environments with vulnerable population groups (i.e. kindergartens), where the number of users and activity might be dynamically changed. Unfortunately, such biased approach is reflected in collateral damage, the attainment of physiological minimums and its negative health outcomes. We reviewed these problems in current design practice, as reported by users, and they present the motive of our research.

As it was presented, in the design of ventilation systems for educational institutions, special attention is needed, due to present vulnerable population groups. Required design ventilation rates have to be defined in-line with scientific findings that support higher ventilation rates to attain optimal indoor air quality. To attain energy efficiency, deep renovation is needed, from building envelope **[43]** to mechanical systems based on renewable energy sources **[44]**. Special attention has to be paid to thermal comfort that should be based on exergy analyses approach **[45]**, which takes into account location characteristics and user specifics **[46]**. Our study evaluated the effect of recuperators. It showed the decreased energy use for heating from 12 % (0.5 ACH) to 68 % (8.9 ACH and 11.3 ACH), which is comparable to other studies **[17]**. Other researchers **[17]** to **[19]** recommend combination of passive and active systems in order to achieve energy efficiency without deterioration of IEQ.

5 CONCLUSIONS

Building renovation should be directed towards attaining healthy and incentive indoor environments particularly for vulnerable population groups. This approach is highlighted also in new Directive (EU) 2018/844 **[1]**: “Better performing buildings provide higher comfort levels and wellbeing for their occupants and improve health by reducing mortality and morbidity from a poor indoor climate. Adequately heated and ventilated dwellings alleviate negative health impacts caused by dampness, particularly amongst vulnerable groups such as children and the elderly and those with pre-existing illnesses”.

Unfortunately, besides the treated issues of deteriorated IAQ, there is also a problem in current design practice that the actual number or children and educators in a playroom is much higher than the defined number in the building permit. Irrespectively, the selected calculation model for the design of ventilation, i.e. ACH, and $m^3/(hm^2)$ might results in sufficient outdoor airflow per m^2, but not per person. This can cause problematic deterioration of IAQ.

To maintain high level of IAQ it is necessary to implement integral interventions, supported by national policies and strategies. Healthy indoor environment may encourage a higher renovation rate **[2]**, which will bring large-scale benefits to individuals and society alike.

The study presents the first example of the critically assessed problem, related to energy efficient design approach in Slovenia, from IEQ point of view. According to the literature review, the presented problem is relevant also in other countries. Although our study was focused on the national legislation status, the recommendations can be applicable in any indoor environment and country with similar practice. In order to achieve healthy, comfortable, stimulating and healing conditions **[47]**, optimal values that reflect in prevented and mastered health risk factors have to be defined. The number of people (e.g. given as a schedule, etc.) as a basic criteria for the building and system design process shall be used. The definition of ventilation rate according to the number of people presents an important step in the design process defined in EN 16798-3 **[40]**, and is required for all sub-holders. All these issues by EN 16798-3 **[40]** shall be implemented in national legal acts.

6 ACKNOWLEDGEMENTS

The authors acknowledge the financial support from the Slovenian Research Agency (research core funding No. P2-0158, Structural engineering and building physics).

7 NOMENCLATURES

ACH	air changes per hour, [1/h]
A_{du}	DuBois body surface area, [m^2]
A_z	net occupant floor area of the ventilation zone, [m^2]
A_{window}	window area, [m^2]
$M_{children}$	metabolic rate of children, [W/m^2]
U_{floor}	thermal transmittance of floor, [W/(m^{2}K)]
U_{roof}	thermal transmittance of roof, [W/(m^{2}K)]
U_{window}	thermal transmittance of window, [W/(m^{2}K)]
U_{wall}	thermal transmittance of wall, [W/(m^{2}K)]
$V_{in,d}$	designed inlet air volume flow, [m^3/h]
$V_{out\ ,d}$	designed outlet air volume flow, [m^3/h]
V_z	zone volume, [m^3]
WWR	window to wall ratio, [-]
$\tau_{ao\ v}$	glass visible transmittance, [-]

8 REFERENCES

[1] Directive (EU) *2018/844 of the European Parliament and of the Council of 30 May 2018 amending Directive 2010/31/EU on the energy performance of buildings and Directive 2012/27/EU on energy efficiency*.

[2] *Directive 2012/27/EU of the European Parliament and of the Council of 25 October 2012 on energy efficiency, amending Directives 2009/125/EC and 2010/30/EU and repealing Directives 2004/8/EC and 2006/32/EC*.

[3] Energy Act (2015). *Official Gazette of the Republic of Slovenia*, no. 17/14, 81/15.

[4] Rules on the ventilation and air-conditioning of building (2002). *Official Gazette of the Republic of Slovenia*, no. 42/02 with changes. (in Slovene)

[5] Seppänen, O.A., Fisk, W.J., Mendell, M.J. (1999). Association of ventilation rates and CO$_2$ concentrations with health and other responses in commercial and institutional buildings. *Indoor Air*, vol. 9, no. 4, p. 226-252, **DOI:10.1111/j.1600-0668.1999.00003.x**.

[6] Araújo-Martins, J., Carreiro Martins, P., Viegas, J., Aelenei, D., Cano, M.M., Teixeira, J.P., Paixão, P., Papoila, A.L., Leiria-Pinto, P., Pedro, C., Rosado-Pinto, J., Annesi-Maesano, I., Neuparth, N. (2014). Environment and Health in Children Day Care Centres (ENVIRH) – Study rationale and protocol. *Revista Portuguesa de Pneumologia* (English Edition), vol. 20, no. 6, p. 311-323, **DOI:10.1016/j.rppneu.2014.02.006**.

[7] Mainka, A., Zajusz-Zubek, E. (2015). Indoor air quality in urban and rural preschools in Upper Silesia, Poland: Particulate matter and carbon dioxide. International Journal of Environmental Research and Public Health, vol. 12, no. 7, p. 7697-7711, DOI:10.3390/ijerph120707697.

[8] Butala, V., Novak, P. (1999). Energy consumption and potential energy savings in old school buildings. *Energy and Buildings*, vol. 29, no. 3, p. 241-246, **DOI:10.1016/S0378-7788(98)00062-0**.

[9] Dovjak, M., Pajek, L. (2016). Childcare - the role of comfort conditions in kindergartens, in-situ analysis and proposed measures. *Institute of Public and Environmental Health*, p. 1-14. (in Slovene)

[10] Deng, W.-J., Zheng H.-L., Tsui, A.K.Y., Chen, X.-W. (2016). Measurement and health risk assessment of PM2.5, flame retardants, carbonyls and black carbon in indoor and outdoor air in kindergartens in Hong Kong. *Environment International,* vol. 96, p. 65-74, **DOI:10.1016/j.envint.2016.08.013**.

[11] Hwang, S.H., Seo, S.C., Yoo, Y., Kim, K.Y., Choung, J.T., Park, W.M. (2017). Indoor air quality of daycare centers in Seoul, Korea. *Building and Environment*, vol. 124, p. 186-193, **DOI:10.1016/j.buildenv.2017.07.042**.

[12] Villanueva, F., Tapia, A., Lara, S., Amo-Salas, M. (2018). Indoor and outdoor air concentrations of volatile organic compounds and NO2 in schools of urban, industrial and rural areas in Central-Southern Spain. *Science of the Total Environment*, vol. 622-623, p. 222-235, DOI:10.1016/j.scitotenv.2017.11.274.

[13] Miri, M., Alahabadi, A., Ehrampoush, M.H., Ghaffari, H.R., Sakhvidi, M.J.Z., Eskandari, M., Rad, A., Lotfi, M.H., Sheikhha, M.H. (2018). Environmental determinants of polycyclic aromatic hydrocarbons exposure at home, at kindergartens and during a commute. *Environment International*, vol. 118, p. 266-273, **DOI:10.1016/j.envint.2018.06.006**.

[14] BPIE, Buildings Performance Institute Europe (2011). Europe's Buildings under the Microscope. A country-by-country review of the energy performance of buildings, from *http://bpie.eu/publication/europes-buildings-under-the-microscope/*, accessed on 15.10.2018.

[15] Česen, M., Urbančič, A., Lah, P. (2008) Energy use in the public sector, its costs and environmental impacts, from *https://www.stat.si/StatisticniDnevi/Docs/Radenci%202012/prispevki/Cesen_RabaEnergijeEmisijeStroskiJS-Prispevek_v2.pdf*, accessed on 15.10.2018.

[16] NYSERDA, New York State Energy Research and Development Authority (2018). Evaluation of increased ventilation rates and energy conservation measures at Four New York State Schools, from *https://www.nyserda.ny.gov/About/Publications/EA-Reports-and-Studies/Energy-Efficiency-Services-Reports*, accessed on 12.10.2018.

[17] Ben-David, T., Rackes, A., Waring, M.S. (2018). Simplified daily models for estimating energy consumption impacts of changing office building ventilation rates. *Building and Environment*, vol. 127, p. 250-255, **DOI:10.1016/j.buildenv.2017.11.002**.

[18] Hekmat, D., Feustel, H.E., Modera, M.P. (1986). Impacts of ventilation strategies on energy consumption and indoor air quality in single-family residences. Energy and Buildings, vol. 9, no. 3, p. 239-251, **DOI:10.1016/0378-7788(86)90024-1**.

[19] Deng ,Y., Feng, Z., Fang, J., Cao, S.-J. (2018). Impact of ventilation rates on indoor thermal comfort and energy efficiency of ground-source heat pump system. *Sustainable Cities and Society*, vol. 37, p. 154-163, **DOI:10.1016/j.scs.2017.11.014**.

[20] Aflaki, A., Hirbodi, K., Mahyuddin, N., Yaghoubi, M., Esfandiari, M. (2019). Improving the air change rate in high-rise buildings through a transom ventilation panel: A case study. *Building and Environment*, vol. 147, p. 35-49, **DOI:10.1016/j.buildenv.2018.10.011**.

[21] DEPA, Danish Environmental Protection Agency. (2016). Emission of Formaldehyde from Furniture, from *https://www2.mst.dk/Udgiv/publications/2016/01/978-87-93435-12-4.pdf*, accessed on 2018-03-01.

[22] NIST (2017). National Institute of Standards and Technology. CONTAM Software, from *https://www.nist.gov/services-resources/software/contam*, accesed on 2018-03-01.

[23] Persily, A., de Jonge, L. (2017). Carbon dioxide generation rates for building occupants. *Indoor Air*, vol. 27, no. 5, p. 868-879, **DOI:10.1111/ina.12383**.

[24] Yun, H., Nam, I., Kim, J., Yang, J., Lee, K., Sohn, J. (2014). A field study of thermal comfort for kindergarten children in Korea: An assessment of existing models and preferences of children. *Building and Environment*, vol. 75, p. 182-189, **DOI:10.1016/j.buildenv.2014.02.003**.

[25] Dovjak, M, Košir, M, Kristl, Ž. (2014). Integral interventions for improved indoor air quality in energy efficient kindergartens. *24th Scientific Conference on Energy and the Environment*, vol. 5, p. 261-270.

[26] Pirc, J. (2014). *Study of indoor air quality in prefabricated and classically built kindergarten*. University of Ljubljana, Faculty of Civil and Geodetic Engineering, p. 1-104.

[27] EN 13986:2004. *Wood-based panels for use in construction – Characteristics, evaluation of conformity and marking*. International Organization for Standardization, Geneva.

[28] EN 717-1:2004. *Wood-based panels – Determination of formaldehyde release – Part 1: Formaldehyde emission by the chamber method*. International Organization for Standardization. Geneva.

[29] EN 15251:2007. *Indoor environmental input parameters for design and assessment of energy performance of buildings-addressing indoor air quality, thermal environment, lighting and acoustics*. International Organization for Standardization, Geneva.

[30] ANSI/ASHRAE Standard 62.1:2004. *Ventilation for acceptable indoor air quality*. ASHARE, Atlanta.

[31] WHO, World Health Organization. (2010). Formaldehyde. Selected pollutants. *WHO Guidelines for Indoor Air Quality. WHO*, Regional Office for Europe, Copenhagen, p. 103-156.

[32] *NIOSH, National Institute for Occupational Safety and Health*. (2010). NIOSH Pocket Guide to Chemical Hazards. CDC, Atlanta.

[33] EnergyPlus(2018). EnergyPlus 8.0.0., from: *https://energyplus.net/features*, accessed on2018-01-08.

[34] Földváry, V., Bekö, G., Langer, S., Arrhenius, K., Petráš, D. (2017). Effect of energy renovation on indoor air quality in multifamily residential buildings in Slovakia. *Building and Environment*, vol. 122, p. 363-372, **DOI:10.1016/j.buildenv.2017.06.009**.

[35] WHO, World Health Organisation. (2016). Household air pollution and health, from *http://www.who.int/mediacentre/factsheets/fs292/en/*, accessed on 2018-03-01.

[36] Bakó-Biró, Z., Clements-Croomea, D.J, Kochhara, N., Awbia, H.B., Williams, M.J. (2007). Ventilation rates in schools and learning performance. *Proceedings of the 9th REHVA World Congress: Clima 2007 Wellbeing Indoors,* p. 1-19.

[37] *Commission Directive 2001/58/EC of 27 July 2001 amending for the second time Directive 91/155/EEC defining and laying down the detailed arrangements for the system of specific information relating to dangerous preparations in implementation of Article 14 of European Parliament and Council Directive 1999/45/EC and relating to dangerous substances in implementation of Article 27 of Council Directive 67/548/EEC* (safety data sheets).

[38] ANSI/ASHRAE Standard 62.1:2010. *Ventilation for Acceptable Indoor Air Quality*. ASHARE, Atlanta.

[39] Report on the Consensus Workshop on Formaldehyde. (1984). *Environmental Health Perspective*, vol. 58, p. 323-81.

[40] EN 16798-3:2017. *Energy performance of buildings - Ventilation for buildings - Part 3: For non-residential buildings - Performance requirements for ventilation and room-conditioning systems.* International Organization for Standardization, Geneva.

[41] SIST CR 1752:1999. *Ventilation for buildings - Design criteria for the indoor environment*. International Organization for Standardization, Geneva.

[42] Carrer, P., Wargocki, P., Fanetti, A. (2015). Can we establish relationship between outdoor air ventilation and health based on the published epidemiological data? *Proceedings of the 11th International Conference on Industrial Ventilation*, vol. 1, p. 62-69.

[43] Hudobivnik, B., Pajek, L., Kunič, R., Košir, M. (2016). FEM thermal performance analysis of multi-layer external walls during typical summer conditions considering high intensity passive cooling. *Applied Energy*, vol. 178, p. 363-375, **DOI:10.1016/j.apenergy.2016.06.036**.

[44] Prek, M., Butala, V. (2012). An enhanced thermal comfort model based on the exergy analysis approach. *International Journal of Exergy,* vol. 10, no. 2, p. 190-208, **DOI:10.1504/IJEX.2012.045865**.

[45] Stritih, U., Koželj, R. (2017). Materials and numerical analysis of thermochemical seasonal solar energy storage for building thermal comfort applications: a review. Research Journal of Environmental Sciences, vol. 11, no. 4, str. 177-191, **DOI:10.3923/rjes.2017.177.191**.

[46] Thapa, R., Rijal, H.B., Shukuya, M. (2018). Field study on acceptable indoor temperature in temporary shelters built in Nepal after massive earthquake 2015. Building and Environment, vol. 135, p. 330-343, **DOI:10.1016/j.buildenv.2018.03.001**.

[47] Dovjak, M., Shukuya, M., Krainer, A. (2018). User-centred healing-oriented conditions in the design of hospital environments. International Journal of Environmental Research and Public Health, vol. 15, no. 10, p. 2140, **DOI:10.3390/ijerph15102140**.

Strojniški vestnik - Journal of Mechanical Engineering 65(2019)1, 41-49
© 2019 Journal of Mechanical Engineering. All rights reserved.
DOI:10.5545/sv-jme.2018.5301
Original Scientific Paper
Received for review: 2018-02-20
Received revised form: 2018-07-07
Accepted for publication: 2018-08-09

Experimental Investigation of Newtonian and Non-Newtonian Liquid Flow in Wavy and Straight Mini-Channel Cross-Flow Plate Heat Exchangers

Ali Reza Anvari[1] – Koroush Javaherdeh[2,*]
[1] University of Guilan, Department of Mechanical Engineering, Iran
[2] University of Guilan, Faculty of Mechanical Engineering, Iran

In this research, an experimental study was performed regarding the heat transfer performance and pressure drop specifications of a Newtonian fluid and a non-Newtonian fluid. To this end, laminar flow of the deionized (DI) water and the aqueous solution containing 0.2 wt.% carboxyl methyl cellulose (CMC) were used as the Newtonian fluid and the non-Newtonian fluid, respectively, in wavy and straight mini-channel cross-flow heat exchangers (CFHE). Each mini-channel cross-flow plate heat exchanger (MCFPHE) was made of three copper plates for the hot and cold sides, which contain 27 mini-channels in parallel. The mini-channel CFHE was examined for Reynolds numbers (Re) in the range of 200 to 1800 and the hot-side inlet temperature was between 40 °C and 50 °C while the cold-side temperature varied in the range of 10 °C to 20 °C. The thermal and rheological properties of the non-Newtonian fluid were investigated. The results showed that for both fluids, the thermal performance of the wavy mini-channel is more than that of the straight mini-channel and, although the pressure drop was intensified, its effect is low at high Re values

Keywords: heat exchanger, mini-channel, non-Newtonian, CMC, wavy

Highlights

- *Non-Newtonian flow and convective heat transfer characteristics through straight and wavy micro-channels are experimentally investigated.*
- *Thermal and hydrodynamic performances of wavy micro-channels are investigated for different relative waviness.*
- *Results showed that the thermal and hydrodynamic performances increase with an increase in the relative waviness of wavy micro-channels.*

0 INTRODUCTION

The increasing industrial development of recent decades is directly linked to the improvement and development of new technologies. Heat exchangers are devices that are used to perform the thermal exchange between two fluids at different temperatures and, considering their wide applications, they have become the object of several research studies and developments. However, even along with this increasing evolution, the improvement of this system continues to be sought [1] and [2], aiming at both the conservation of energy and the elaboration of projects applied to specific situations. Among the several existing types, one of the best known is the plate heat exchanger. This type of equipment is widely used in various industrial segments and with numerous applications. Due to the need for smaller equipment with high effectiveness, micro- and mini-channel heat exchangers were developed. The higher volumetric heat transfer densities require advanced manufacturing techniques and more complex manifold designs. Dixit and Ghosh [3] summarized the manufacturing processes used in the fabrication of mini/micro-channel heat sinks and compared the different techniques related to tolerances and material compatibility. Naqiuddin et al. [4] reviewed the different geometric designs of mini/micro-channels, which were derived from numerical simulation and experimental works. Sidik et al. [5] comprehensively discussed the passive techniques for heat transfer augmentation in mini/micro-channels. Even though mini- and micro-channels can enhance the heat transfer rates significantly, it is not sufficient for some applications that need large heat fluxes. Thus, the usage of wavy channels has been considered. It was reported that wavy channels with larger wave amplitudes and shorter wavelengths [6], and channels employing coolants with nano-particles displayed better cooling performance. In another study, by Rostami et al. [7], water-Cu and water-Al_2O_3 as nanofluid was investigated in terms of heat transfer capability and fluid flow by using a rectangular micro-channel. It was shown that the Nusselt number increases with the increase in volume fraction and the decrease in particle diameter and that it is about three times higher for a nanofluid in a wavy micro-channel as compared to water in a straight micro-channel.

---

*Corr. Author's Address: Department of mechanical engineering, University of Guilan, Rasht, Iran, javaherdeh@guilan.ac.ir

The fluid flow and heat transfer capability of the TiO_2 nanofluid were studied by Arshad and Ali **[8]** experimentally in the straight mini-channel heat sink for laminar and transitional flows. The nanofluid containing 15 wt.% nanoparticle was used as a coolant. It is reported that the thermal performance of the nanofluid is a function of heating power, which could be enhanced at lower heating power. However, by decreasing the heating power, the pressure drop was increased.

Furthermore, Sohel et al. **[9]** have shown that the by using the nanofluid as a coolant, cooling performance is enhanced considerably. They have revealed that the nanoparticles in addition to enhancing the heat transfer, do not lead to excessive pressure. Thermal performance of a microprocessor was investigated by using pure water and nanofluid of Al_2O_3 and Cu by Siddiqui et al. **[10]**. It was observed that the Al_2O_3-water nanofluid yields significant performance in enhancing the heat transfer coefficient and reducing the thermal resistance. Also, by increasing the Reynolds number, the Cu-water nanofluid provided better results for thermal enhancement. Singh et al. **[11]** numerically confirmed the enhancement of the heat transfer in a 3D MHS by Nanofluids. The Nanofluids were found to increase the heat transfer rate compared to water. Parametric studies are carried out for different particle concentrations of 1, 3, and 5 vol.%. The particle size effect is observed for different particle sizes of 50 nm and 150 nm. In addition to the Nanofluid, non-Newtonian fluid **[12]** to **[18]** is an alternative for working fluid. Compared with Nanofluids, non-Newtonian fluids widely exist and can easily be prepared. Many common fluids such as solutions of polymers or surfactants, shows non-Newtonian fluid behaviour. The behaviour of non-Newtonian fluids is of great interest to many applications, including collecting, distributing, detecting, mixing and separating different types of biological and chemical species in a microchip. As a working fluid of a heat exchanger, for example, the heat transfer performance of non-Newtonian fluids was studied by Shamsi et al. **[19]** and Li et al. **[20]** in square micro-channels with triangular ribs and in a manifold micro-channel heat sink, respectively. They have reported that by increasing the volume fraction of the nanoparticles, the heat transfer is adversely affected.

Moreover, Li et al. **[21]** reported an increase in heat and mass transfer by non-Newtonian flows and noticed that the change in the dynamic viscosity of the materials in working chemical materials is the main reason for strengthening the secondary flow in the dimpled/protruded passage with flow separation. Pimenta and Campos **[22]** proved that the Nusselt numbers (*Nu*) for the non-Newtonian fluid flows in a spiral coil were, on mean, somewhat higher than those for Newtonian fluids because the viscous element of the shear-thinning polymer shows a tendency to affect the mixing effect of the Dean vortices. In the current work, the non-Newtonian characteristic of aqueous solutions containing 2 wt.% carboxyl methyl cellulose (CMC) was assessed, and calculations were also performed regarding the rheological behaviour of the non-Newtonian fluid. Furthermore, for a new cross-flow heat exchanger, pressure drop and heat transfer performance were studied with experiments with straight and wavy mini-channels.

1 MATERIALS AND METHODS

The CMC solutions were prepared by adding sodium carboxyl methyl cellulose with a nominal molecular weight of 900,000 [$gmol^{-1}$] and a DS of 0.8 to 0.95 (Dae-Jung company, South Korea) to distilled water, and agitating it on an electromagnetic stirrer at low axial speed for 2 h, to achieve complete hydration and avoiding the formation of air bubbles. The studied concentration was 0.2 *wt*.%. The specific heat c_p [Jkg^{-1} k^{-1}] and thermal conductivity *k*, were obtained for 0.2 % CMC solution, at temperatures between 40 °C and 50 °C. By adopting KD2 Pro (Decagon Devices, Inc., USA), the thermal conductivity and specific heat at constant were obtained for a non-Newtonian fluid. This is a portable device that is used in thermal analyses. For evaluating the specific heat (heat capacity) and thermal conductivity, the transient line heat source method is used with a KD2 device **[23]**. A small needle sensor (SH-1) was employed for assessing the specific heat in which the heat pulse method is used, and reliable values are obtained for specific heat capacity c_p by using nonlinear least square method during the processes. Only the SH-1 sensor can be considered for determining the specific heat, which is 30 mm in length and 1.28 mm in diameter and distance between two needles is 6 mm. By adopting this sensor, the thermal conductivity can also be determined **[24]** and **[25]**. The precision of this instrument is 5 % which meets the standards of EN 55022 **[26]** and IEEE 442-1987 **[27]**. The density of the CMC solution was determined in triplicates, by pycnometer. Rheological measurements were determined using a Rheometer (MCR 301 by Anton Paar, Graz, Austria) equipped with a cone-and-plate geometry (angle: 0.034 rad, diameter: 40 mm). The shear rate was varied between 12.2 s^{-1} and 200 s^{-1}, and both upward and downward tests were performed in duplicate for the CMC solution, at five different temperatures between 10 °C and 50 °C.

2 EMPIRICAL SETUP AND METHODOLOGY

An experimental setup has been developed to examine the heat transfer characteristics and the drop in the pressure of the wavy and straight mini-channels under different flow conditions as shown in Fig. 1. It consists of two parts: a hot fluid and a cold fluid. For maintaining the inlet temperature and flow velocity at constant values, a thermostatic bath, a controllable magnetic gear pump and a paddle wheel flow meter were used for each part of the setup. Two filters were installed at the entrance of each flow meter to remove the external matter in the liquid and to prevent fluctuations and the rusting of the flow meter. Insulation is applied throughout the unit in an experimental setting in order to minimize the heat loss. Thermocouples, as well as absolute and differential pressure transmitters, were installed on all inputs and outputs. Before starting each experiment, each measuring device was calibrated. Non-Newtonian fluid flow rate has been varied in a range of 0.5 Lmin^{-1} to 4 Lmin^{-1} whereas the inlet hot stream temperature ranges from 40 °C to 50 °C. The cold stream flow rate has been varied in range of 0.5 Lmin^{-1} to 4 Lmin^{-1} along with inlet temperature being in a range of 10 °C to 20 °C. A typical test usually takes about 20 minutes. A time interval was needed for the system to achieve stable conditions. To verify that such conditions have reached a stable state, the temperature was monitored continuously. Once the thermal equilibrium conditions were obtained, the flow rate and temperature readings were recorded. The average values of the measurements were recorded beside the estimated errors.

The heat exchanger plate used in this study was fabricated from copper alloy. Each plate was 80 mm in width and 80 mm in length, and the thickness is 2 mm. The wavy and straight mini-channels with cross-sectional dimensions of 1 mm in width and 1 mm depth were machined with a CNC machine. Schematic patterns of the constructed plates with two keyway dimensions are shown in Fig. 2.

As can be observed in the figure, specific geometrical parameters of wavy channels can be considered for investigating the relative waviness (2A/2L). In this regard, in the current research, the impact of such parameters on the performance of cross-flow heat exchangers was studied on two levels of relative waviness (i.w. 2A/2L = 0.2 and 0.3). The

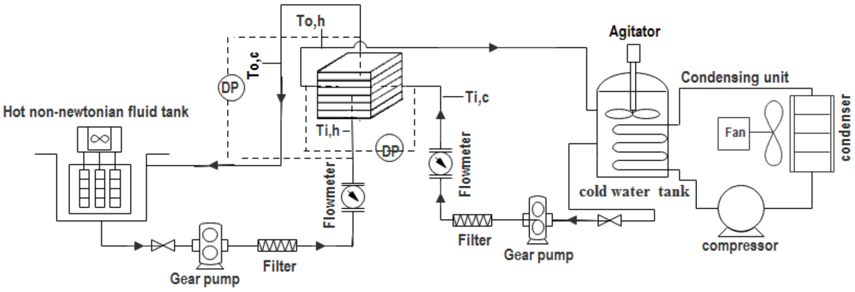

Fig. 1. *Schematic diagram of the experimental setup*

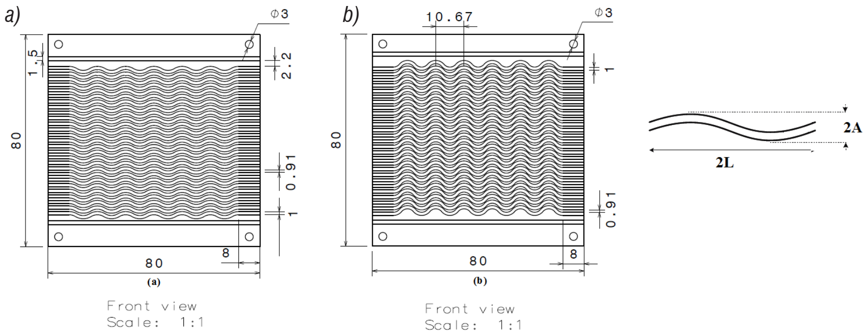

Fig. 2. *Schematic of a repeating unit of wavy mini-channels; a) 2A/2L=0.2, b) 2A/2L=0.3*

dimensions of the mini-cross-flow heat exchanger are also tabulated in Table 1.

Table 1. *Geometrical parameters of tested plate heat exchanger*

Parameter	Value
Wave amplitude [2A]	2.2, 3.2
Dimensions of heat exchanger (w×l×h)[mm]	100×100×22
Dimensions of plates (w×l×t) [mm]	80×80×2
Wavelength (2L) [mm]	10.67
Thermal conductivity of plate material [$\mathrm{Wm^{-1}k^{-1}}$]	385
Total number of channels	27
Number of channels per plate	6

2.1 Thermal Physical Properties of CMC Aqueous Solutions

Specific heat capacity and thermal conductivity were determined at three different temperatures. Fig. 3 shows the viscosity against the shear stress of the CMC aqueous solution at different temperatures. By increasing the shear rate, the viscosity of the CMC aqueous solutions decreases, also at the same shear rate, the viscosity of the CMC aqueous solutions increases with decreases in temperature.

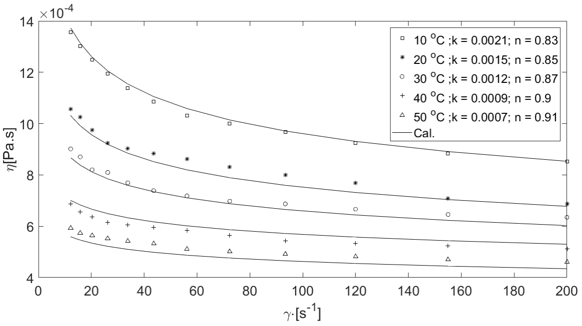

Fig. 3. *The relation of viscosity and shear rate for CMC aqueous solution*

It is disclosed that the CMC solutions present shear-thinning behaviour. However, the CMC aqueous solutions follow the power law model, given in Eq. (1), with a flow behaviour index or power law index of less than unity ($n < 1$) [28] and [29]:

$$\eta = K\gamma^{n-1}. \quad (1)$$

In Eq. (1) η [Pa·s] is the apparent viscosity, γ [$\mathrm{s^{-1}}$] is the shear rate, and parameters K and n [m] are the consistency index and the power law index, respectively.

3 RESULTS AND DISCUSSION

Experiments were conducted for two wavy channels with different relative waviness ($2A/2L$) of the wavy mini-channels and in the presence of CMC to study the effects of these parameters on heat transfer capability and friction factor. Initial tests were also performed for a straight channel and base fluid to validate the experiment procedure and form baselines for the comparison. The inlet temperature for the hot liquid was 40 °C and 50 °C, with a cold water temperature of 10 °C to 20 °C. The hot and cold flow rate in Reynolds was measured from 200 to 600. The heat transfer rate in hot and cold fluids through the test section can be achieved using $\dot{Q} = \dot{m} c_p \Delta T$. By considering the logarithmic temperature average (LMTD), the heat transfer coefficient (U) can be evaluated:

$$\Delta T_{LMTD} = \frac{(T_{i,hot} - T_{o,cold}) - (T_{o,hot} - T_{i,cold})}{\ln\left\{(T_{i,hot} - T_{o,cold}) - (T_{o,hot} - T_{i,cold})\right\}}, \quad (2)$$

and mean heat transfer $\dot{Q}_m$ [W], via

$$U = \frac{\dot{Q}_m}{F\, A_S\, \Delta T_{LMTD}}. \quad (3)$$

That A_S [$\mathrm{m^2}$] is the total heat transfer area and $\dot{Q}_m = \left(\dot{Q}_{hot} + \dot{Q}_{cold}\right)/2$. Also, the coefficient factor F for the cross-flow heat exchanger in this equation is 0.97. The hydraulic diameter is calculated using the proposed method by [30] as:

$$d_h = \frac{4V_S}{A_S}, \quad (4)$$

where V_S [$\mathrm{m^3}$] is the enclosed (wetted) volume. For power law fluids, Tang et al. [32] introduced a new generalized *Re*. For power law fluid flow, the generalized *Re* for non-Newtonian fluid is presented as:

$$\mathrm{Re} = \frac{\rho\, d_h^n\, u^{2-n}}{k}\left(\frac{n}{a+bn}\right)^n 8^{1-n}, \quad (5)$$

where ρ [$\mathrm{kgm^{-3}}$] and u [$\mathrm{ms^{-1}}$] are density and the average velocity of the fluid respectively, and k and n are the rheological parameters that are obtained from Eq. (1), for the CMC solution. The constants are $a = 0.2121$ and $b = 0.6766$ for square cross-sectional channels [31]. It is noteworthy that the heat transfer coefficients of the hot and cold loop should be calculated independently.

The Fanning friction factor was also calculated using the following equation:

$$f = \frac{1}{2}\frac{d_h\, \Delta P / L}{\rho u^2}. \quad (6)$$

In plate heat exchanger (PHE) experiments, the temperatures, flow rates and pressure loss were measured by employing appropriate instruments.

During the measurements, uncertainties of the PHE results were estimated by Moffat's theory **[32]**. In this theory, Moffat has defined the final result (Y) as a function of different measured variables, X_i, through $Y=f(X_1,X_2,\ldots,X_n)$. According to this theory, the contribution of the uncertainty to each variable can be estimated by:

$$\frac{U_Y}{Y}=\frac{\sqrt{\left(\frac{\partial Y}{\partial X_1}U_{X_1}\right)^2+\ldots+\left(\frac{\partial Y}{\partial X_n}U_{X_n}\right)^2}}{f\left(X_1,X_2,\ldots,X_n\right)}. \qquad (7)$$

The overall uncertainty for the estimated results is given in Table 2. Repeated tests show that all the sets of the experimental data are within the uncertainty limits.

Table 2. *Parameters and estimated uncertainty*

Instrument / parameters	Model	Accuracy
Flow meter [l/min]	Fotek - KTM	±0.5 % of readings**
Thermocouples [T]	Type-T	±1.0 [°C] of readings**
Pressure transmitter [p]	EWDT-2.5	≤1%**
Pump [24DC]	Gear pump	Head 21 meter
PID controller	Delta	±1% of readings*
Bolt heater [W]	2000	±2% of readings**
Thermo-physical properties		
Viscosity	Brookfield	±2.5% of readings*
Density	Anton paar, MCR 301	±3% of readings*
Thermal conductivity	Decagon KD2-Pro	±5% of readings*
Specific heat	Decagon KD2-Pro	±5% of readings*
Calculated parameters		
Reynolds number of hot and cold side	Moffat	±1% to 2%
Heat transfer coefficient of hot and side	Moffat	±6% to 7%
Friction factor	Moffat	±6%

* Based on manufacturer claim
**Based on the calibration process

3.1 Validation

To validate the present experimental results and form a baseline for comparison, the initial tests are conducted for the water flow in the straight mini-channel cross-flow heat exchanger. The straight mini-channel has the same number of mini-channels and magnitude of geometrical parameters as the wavy channel. The fitted curve of the heat transfer rate is calculated using correlations of Nu proposed by Shah and London and Stephan and Preußer **[33]** and **[34]** which are used to validate the experimental data of heat transfer rate as depicted in Fig. 4 for the water flow against the Re of the cold fluid. As shown in the figure, the obtained results in the present study are in good agreement with analytical analysis. For estimating the heat transfer coefficient, the following relation is employed:

$$U=\frac{1}{\frac{1}{h_{hot}}+\frac{1}{h_{cold}}+\frac{t}{K_{cooper}}}, \qquad (8)$$

where t [mm] is the thickness of the plate, K_{cooper} [$Wm^{-1}k^{-1}$] is the thermal conductivity of copper (the heat exchanger has been fabricated from copper), h_{hot} [$Wm^{-2}k^{-1}$] and h_{cold} [$Wm^{-2}k^{-1}$] are the convective heat transfer coefficients of the hot and cold water, respectively. The correlations overestimate the obtained results. However, it can be related to the fouling resistances that are ignored during the calculations and, considering the fact that the correlations are empirical, the obtained data would be acceptable.

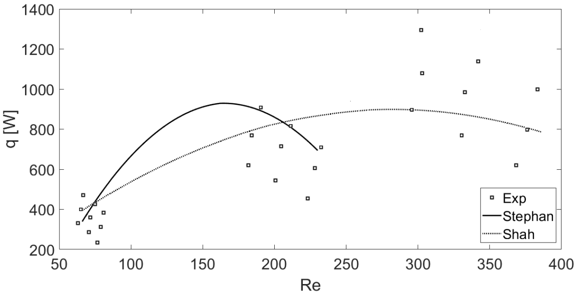

Fig. 4. *Experimental evaluation compared to calculated using correlations by Shah and London and Stephan and Preußer*

3.2 Effect of Geometrical Parameters

There are three submissive mechanisms **[35]** that enhance the heat transfer rate in single-phase flow, including: (1) decrease in thickness of the thermal boundary layer, (2) increase in fluid disturbance **[36]** and **[37]**; and (3) increase in gradient velocity in vicinity of the heat transfer wall. When the fluid flows in wavy channels, disturbance of the streamlines of the flow occurs **[38]** to **[40]**. Mixing of the flow is the result of this interruption and, as a consequence, the heat transfer capability is enhanced. The regions that possess the maximum amplitude values in a wavy channel initiate the vortices and secondary flows.

While flowing the liquid through curved passages, the liquid is exposed to centrifugal force resulting in secondary flow, which is commonly known as Dean Vortices or chaotic advection; as vortices are formed, the fluid undergoes a rapid shearing and stretching, which results in better fluid mixing and, consequently, higher rates of heat transfer are acquired.

In addition, the pressure near the outer concave wall is increased due to the centrifugal force in the curvature of the channel and, as a result, the pressure gradient is enhanced toward the centre of the flow. Considering this pressure gradient, the high-pressure fluid is moved from the outer region toward the core **[41]**.

However, all these processes enhance not only the heat transfer rate but also the pressure drop. Fig. 5a shows the variations of *q* as a function of Re. It is clear that the higher heat transfer is obtained for a wavy mini-channel cross-flow heat exchanger (MCFPHE) compared with the straight channels in which the heat transfer rate is increased with the relative waviness. The analysis of *U* vs. Re of the cold fluid confirms this conclusion as shown in Fig. 5b.

3.3 Effect of Non-Newtonian Behaviour

The viscosity increase caused by the CMC dissolution in water can affect the flow pattern or flow regime considerably. To study the effects of the non-Newtonian fluid, i.e. the water–CMC mixtures, the variations of the q as a function of the Re are shown in Fig. 6. According to this figure, the same conclusion regarding the wavy effect of Newtonian fluid can be drawn. However, higher heat transfer values compared to the Newtonian fluid are obtained at all configurations.

3.4 Pressure Drop Characteristics

Experiments showed that using the CMC/water non-Newtonian fluids can slightly enhance the pressure drop in comparison to the base fluid. In fact, the presence of CMC inside the water can enhance the viscosity and, as a result, higher values of pressure drop are obtained for the non-Newtonian fluids.

Fig. 7 compares the pressure drop of the systems with water and CMC solution as hot fluid versus Re of the hot fluid. According to this figure, the ratio is always higher than 1, which verifies the above-mentioned conclusion in comparing the non-Newtonian and Newtonian fluids. The effect of temperature is negligible and wavy 2 (with higher relative waviness) shows the least pressure drop ratio, especially at higher Re.

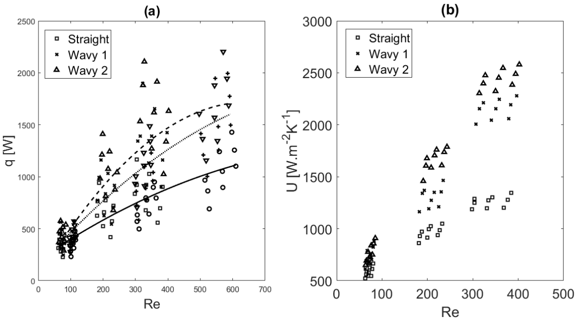

Fig. 5. *Experimental data for a) heat transfer, q and b) heat transfer coefficient of MCFPHE using water as hot and cold fluid*

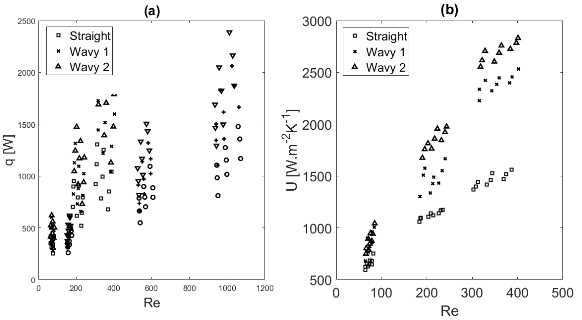

Fig. 6. *Experimental data for a) heat transfer, q and b) heat transfer coefficient, U of MCFPHE using water as cold fluid and CMC solution as hot fluid*

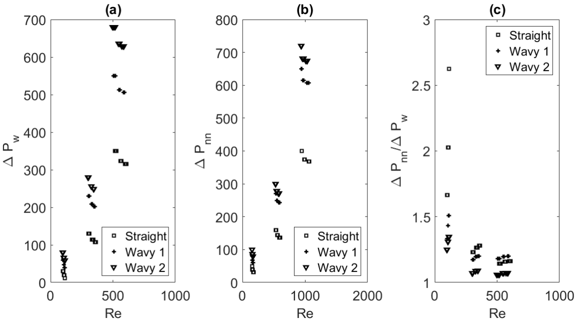

Fig. 7. *The pressure drop of MCFPHE with water as cold fluid and a) water as hot fluid, b) CMC solution as hot fluid, and c) the ratio of CMC and water pressure drop*

The experimental results of the friction factor are shown in Fig. 8. According to Fig. 8a for water and Fig. 8b for CMC, the friction factor of the wavy channel is always higher than that of the straight channel; however, according to Fig. 8c the influence of non-Newtonian fluid in enhancing the pressure drop is less in the case of wavy MCFPHE with higher relative waviness.

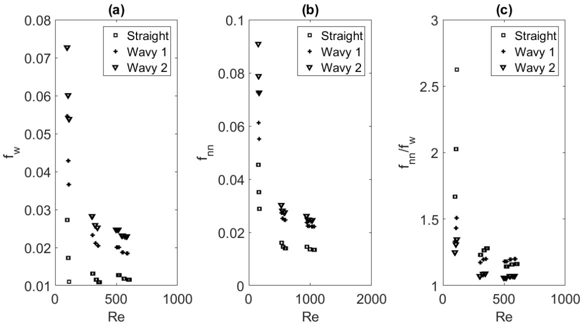

Fig. 8. *Friction factor of MCFPHE with water as cold fluid and a) water as hot fluid, b) CMC solution as hot fluid, and c) the ratio of CMC and water friction factor*

3.5 Overall Performance Factor (PF)

To investigate the performance of wavy passages, the heat transfer performance of the two wavy channel configurations is compared along with the pressure drop. Fig. 9 shows the performance evaluation criterion (PEC) as a function of the Reynolds number. It was calculated from Eq. (9) **[42]**.

$$PEC = \frac{U_{nn}/U_{ws}}{\left(f_{nn}/f_{ws}\right)^{0.333}}, \tag{9}$$

where U_n and f_n are heat transfer coefficient and friction factors of a non-Newtonian fluid flow in a wavy and straight channel with different relative waviness and the U_{ws} and f_{ws} are heat transfer coefficient and friction factors of a DI water in a straight, respectively. It is clear that when the PEC is higher than unity, the applied technique is more in favour of heat transfer improvement rather than increasing the pressure drop.

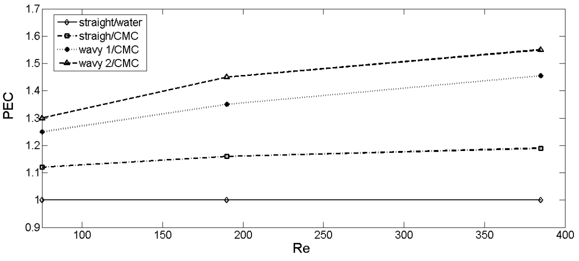

Fig. 9. *Performance evaluation criterion versus Reynolds number for various working fluids in MCFPHE*

The geometric parameters, the working fluid composition, and the Reynolds number affect the amount of this parameter. From Fig. 9, it is clear that for each case, the PEC increases approximately as the Reynolds increases, and the overall improvement due to the wave channel in the higher flow current is significant. Also, for a given flow rate, the non-Newtonian fluid with higher weight fraction has higher values of the PEC.

4 CONCLUSION

In this research work, the thermal-hydraulic performance of a wavy mini-channel cross-flow heat exchanger was studied using the CMC/water as non-Newtonian fluid, and the effects of relative waviness (A/L), non-Newtonian fluid, and Reynolds number were studied. The results obtained for the straight MCHS were first confirmed by considering the previous works for which a reasonable agreement was established. It was observed that for all considered cases, higher heat transfer was obtained for the wavy channel compared with a straight channel. The CMC/water non-Newtonian showed better heating performance compared with the base fluid. The pressure drop of the wavy mini-channels was higher than that of the straight mini-channels. This is due to the change of the geometrical parameter, especially with relative waviness (A/L) change. It is suggested that applying the combined method (i.e. simultaneous use of wavy mini-channels and non-Newtonian fluid) as proposed in this research, can be a good choice in practical applications to enhance the heat transfer performance of cross-flow mini-channel heat exchangers.

5 REFERENCES

[1] Hussein, N.F. (2018). Experimental investigation of using new shape augmentations for enhancing heat transfer in heat exchanger. *Journal of Engineering and Sustainable Development*, vol. 21, no. 6, p. 80-91.

[2] Balaji, K., Iniyan, S., Muthusamyswami, V. (2017). Experimental investigation on heat transfer and pumping power of forced circulation flat plate solar collector using heat transfer enhancer in absorber tube. *Applied Thermal Engineering*, vol. 112, p. 237-247, **DOI:10.1016/j.applthermaleng.2016.09.074**.

[3] Dixit, T. Ghosh, I. (2015) Review of micro-and mini-channel heat sinks and heat exchangers for single phase fluids. *Renewable and Sustainable Energy Reviews*, vol. 41, p. 1298-1311, **DOI:10.1016/j.rser.2014.09.024**.

[4] Naqiuddin, N.H., Saw, L.H., Yew, M.C., Yusof, F., Ng. T.C., Yew, M.K. (2018). Overview of micro-channel design for high heat flux application. *Renewable and Sustainable Energy Reviews*, vol. 82, p. 901-914, **DOI:10.1016/j.rser.2017.09.110**.

[5] Sidik, N.A.C., Muhamad, M.N.A.W., Japar, W.M.A.A., Rasid, Z.A. (2017). An overview of passive techniques for heat transfer augmentation in microchannel heat sink. *International Communications in Heat and Mass Transfer*, vol. 88, p. 74-83, **DOI:10.1016/j.icheatmasstransfer.2017.08.009**.

[6] Lin, L., Zhao, J., Lu, G., Wang, X.-D., Yan, W.-M. (2017). Heat transfer enhancement in microchannel heat sink by wavy channel with changing wavelength/amplitude. *International Journal of Thermal Sciences*, vol. 118, p. 423-434, **DOI:10.1016/j.ijthermalsci.2017.05.013**.

[7] Rostami, J., Abbassi, A., Harting, J. (2018). Heat transfer by nanofluids in wavy microchannels. *Advanced Powder Technology*, vol. 29, no. 4, p. 925-933, **DOI:10.1016/j.apt.2018.01.010**.

[8] Arshad, W., Ali, H.M. (2017). Experimental investigation of heat transfer and pressure drop in a straight minichannel heat sink using TiO_2 nanofluid. *International Journal of Heat and Mass Transfer*, vol. 110, p. 248-256, **DOI:10.1016/j.ijheatmasstransfer.2017.03.032**.

[9] Sohel, M.R., Khaleduzzaman, S.S., Saidur, R., Hepbasli, A., Sabri, M.F.M., Mahbubul, I.M. (2014). An experimental investigation of heat transfer enhancement of a minichannel heat sink using $Al_2O_3–H_2O$ nanofluid. *International Journal of Heat and Mass Transfer*, vol. 74, p. 164-172, **DOI:10.1016/j.ijheatmasstransfer.2014.03.010**.

[10] Siddiqui, A.M., Arshad, W., Ali, H.M., Ali, M., Nasir, M.A. (2017). Evaluation of nanofluids performance for simulated microprocessor. *Thermal Science*, vol. 21, no. 5, p. 2227-2236, **DOI:10.2298/TSCI150131159S**.

[11] Singh, P.K., Naruka, D.S., Seng, L.P. (2018). Numerical investigation of flow and heat transfer of nanofluids in a wavy microchannel. *International Journal of Energy for a Clean Environment*, vol. 19, no. 1-2, p. 19-35, **DOI:10.1615/InterJEnerCleanEnv.2018021099**.

[12] Sajadifar, S.A., Karimipour, A., Toghraie, D. (2017). Fluid flow and heat transfer of non-Newtonian nanofluid in a microtube considering slip velocity and temperature jump boundary conditions. *European Journal of Mechanics-B/Fluids*, vol. 61, p. 25-32, **DOI:10.1016/j.euromechflu.2016.09.014**.

[13] Shojaeian, M., Koşar, A. (2016). Convective heat transfer of non-Newtonian power-law slip flows and plug flows with variable thermophysical properties in parallel-plate and circular microchannels. *International Journal of Thermal Sciences*, vol. 100, p. 155-168, **DOI:10.1016/j.ijthermalsci.2015.09.024**.

[14] Shojaeian, M., Yildiz, M., Koşar, A. (2015). Convective heat transfer and second law analysis of non-Newtonian fluid flows with variable thermophysical properties in circular channels. *International Communications in Heat and Mass Transfer*, vol. 60, p. 21-31, **DOI:10.1016/j.icheatmasstransfer.2014.12.002**.

[15] Stocks, M.D., Bello-Ochende, T., Meyer, J.P. (2014). Maximum thermal conductance for a micro-channel, utilising Newtonian and non-Newtonian fluid. *Heat and Mass Transfer*, vol. 50, no. 6, p. 865-875, **DOI:10.1007/s00231-014-1298-0**.

[16] Ellahi, R. (2013). The effects of MHD and temperature dependent viscosity on the flow of non-Newtonian nanofluid in a pipe: analytical solutions. *Applied Mathematical Modelling*, vol. 37, no. 3, p. 1451-1467, **DOI:10.1016/j.apm.2012.04.004**.

[17] Prasad, K.V., Vajravelu, K., Vaidya, H., Raju, B.T. (2015). Heat transfer in a non-Newtonian nanofluid film over a stretching surface. *Journal of Nanofluids*, vol. 4, no. 4, p. 536-547, **DOI:10.1166/jon.2015.1174**.

[18] Ternik, P., Rudolf, R., Žunič, Z. (2015). Heat-transfer characteristics of a non-Newtonian Au nanofluid in a cubical enclosure with differentially heated side walls. *Materials and Technology*, vol. 49, no. 1, p. 87-93.

[19] Shamsi, M.R., Akbari, O.A., Marzban, A., Toghraie, D., Mashayekhi, R. (2017). Increasing heat transfer of non-Newtonian nanofluid in rectangular microchannel with triangular ribs. *Physica E: Low-dimensional Systems and Nanostructures*, vol. 93, p. 167-178, **DOI:10.1016/j.physe.2017.06.015**.

[20] Li, S.-N., Zhang, H.-N., Li, X.-B., Li, Q., Li, F.-C., Qian, S., Joo, S.W. (2017). Numerical study on the heat transfer performance of non-Newtonian fluid flow in a manifold microchannel heat sink. *Applied Thermal Engineering*, vol. 115, p. 1213-1225, **DOI:10.1016/j.applthermaleng.2016.10.047**.

[21] Li, P., Zhang, D., Xie, Y., Xie, G. (2016). Flow structure and heat transfer of non-Newtonian fluids in microchannel heat sinks with dimples and protrusions. *Applied Thermal Engineering*, vol. 94, p. 50-58, **DOI:10.1016/j.applthermaleng.2015.10.119**.

[22] Pimenta, T.A., Campos, J.B.L.M. (2013). Heat transfer coefficients from Newtonian and non-Newtonian fluids flowing in laminar regime in a helical coil. *International Journal of Heat and Mass Transfer*, vol. 58, no. 1-2, p. 676-690, **DOI:10.1016/j.ijheatmasstransfer.2012.10.078**.

[23] Amrollahi, A., Rashidi, A.M., Lotfi, R., Meibodi, M. E., Kashefi, K. (2010). Convection heat transfer of functionalized MWNT in aqueous fluids in laminar and turbulent flow at the entrance region. *International Communications in Heat and Mass Transfer*, vol. 37, no. 6, p. 717-723, **DOI:10.1016/j.icheatmasstransfer.2010.03.003**.

[24] Sanuade, O.A., Adesina, R.B., Amosun, J.O., Fajana, A.O., Olaseeni, O.G. (2017). Using artificial neural network to predict dry density of soil from thermal conductivity. *Materials and Geoenvironment*, vol. 64, no. 3, p. 169-180, **DOI:10.1515/rmzmag-2017-0012**.

[25] Siddiqui, O.K., Zubair, S.M. (2017). Efficient energy utilization through proper design of microchannel heat exchanger manifolds: A comprehensive review. *Renewable and Sustainable Energy Reviews*, vol. 74, p. 969-1002, **DOI:10.1016/j.rser.2017.01.074**.

[26] EN 55022 (2010). *Information Technology Equipment - Radio Disturbance Characteristics - Limits and Methods of Measurement*, CENELEC, Brussels.

[27] IEEE 854 (1987). *The Standard for Radix-Independent Floating-Point Arithmetic*, Institute of Electrical and Electronics Engineers (IEEE), Piscataway.

[28] Abdelrahim, K.A., Ramaswamy, H.S. (1995). High temperature/pressure rheology of carboxymethyl cellulose (CMC). *Food Research International*, vol. 28, no. 3, p. 285-290, **DOI:10.1016/0963-9969(94)00045-A**.

[29] Yaşar, F., Toğrul, H., Arslan, N. (2007). Flow properties of cellulose and carboxymethyl cellulose from orange peel. *Journal of Food Engineering*, vol. 81, no. 1, p. 187-199, **DOI:10.1016/j.jfoodeng.2006.10.022**.

[30] Hesselgreaves, J.E., Law, R., Reay, D. (2016). *Compact Heat Exchangers: Selection, Design and Operation*. Butterworth-Heinemann, Oxford.

[31] Tang, G.H., Lu, Y.B., Zhang, S.X., Wang, F.F., Tao, W.Q. (2012). Experimental investigation of non-Newtonian liquid flow in microchannels. *Journal of Non-Newtonian Fluid Mechanics*, vol. 173-174, p. 21-29, **DOI:10.1016/j.jnnfm.2012.02.001**.

[32] Moffat, R.J. (1982). Contributions to the theory of single-sample uncertainty analysis. *Journal of Fluids Engineering*, vol. 104, no. 2, p. 250-258, **DOI:10.1115/1.3241818**.

[33] Stephan, K., Preußer, P. (1979). Wärmeübergang und maximale Wärmestromdichte beim Behältersieden binärer und ternärer Flüssigkeitsgemische. *Chemie Ingenieur Technik*, vol. 51, no. 1, p. 37-37, **DOI:10.1002/cite.33051112**. (in German)

[34] Mortean, M.V.V., Paiva, K.V., Mantelli, M.B.H. (2016). Diffusion bonded cross-flow compact heat exchangers: Theoretical predictions and experiments. *International Journal of Thermal Sciences*, vol. 110, p. 285-298, **DOI:10.1016/j.ijthermalsci.2016.07.010**.

[35] Tao, W.Q., He, Y.L., Wang, Q.W., Qu, Z.G., Song, F.Q. (2002). A unified analysis on enhancing single phase convective heat transfer with field synergy principle. *International Journal of Heat and Mass Transfer*, vol. 45, no. 24, p. 4871-4879, **DOI:10.1016/S0017-9310(02)00173-4**.

[36] Wang, Y., Ling, X. (2016). Experimental and numerical studies of fluid flow confined in microchannel. *ASME 5th International Conference on Micro/Nanoscale Heat and Mass Transfer*, p. no.MNHMT2016-6671, **DOI:10.1115/MNHMT2016-6671**.

[37] Chai, L., Wang, L. (2018). Thermal-hydraulic performance of interrupted microchannel heat sinks with different rib geometries in transverse microchambers. *International Journal of Thermal Sciences*, vol. 127, p. 201-212, **DOI:10.1016/j.ijthermalsci.2018.01.029**.

[38] Sui, Y., Teo, C.J., Lee, P.S. (2012). Direct numerical simulation of fluid flow and heat transfer in periodic wavy channels with rectangular cross-sections. *International Journal of Heat and Mass Transfer*, vol. 55, no. 1-3, p. 73-88, **DOI:10.1016/j.ijheatmasstransfer.2011.08.041**.

[39] Sui, Y., Teo, C.J., Lee, P.S., Chew, Y.T., Shu, C. (2010). Fluid flow and heat transfer in wavy microchannels. *International Journal of Heat and Mass Transfer*, vol. 53, no. 13-14, p. 2760-2772, **DOI:10.1016/j.ijheatmasstransfer.2010.02.022**.

[40] Sui, Y., Lee, P.S., Teo, C.J. (2011). An experimental study of flow friction and heat transfer in wavy microchannels with rectangular cross section. *International Journal of Thermal Sciences*, vol. 50, no. 12, p. 2473-2482, **DOI:10.1016/j.ijthermalsci.2011.06.017**.

[41] Yang, C S., Jeng, D.Z., Liu, C.W., Liu, C.G., Gau, C. (2010). Fluid flow and heat transfer in a horizontal channel with divergent top wall and heated from below. *Journal of Heat Transfer*, vol. 132, no. 8, p. 081403, **DOI:10.1115/1.4001606**.

[42] Karwa, R., Sharma, C., Karwa, N. (2013). Performance evaluation criterion at equal pumping power for enhanced performance heat transfer surfaces. *Journal of Solar Energy*, art. ID. 370823, **DOI:10.1155/2013/370823**.

Strojniški vestnik - Journal of Mechanical Engineering 65(2019)1, 50-60
© 2019 Journal of Mechanical Engineering. All rights reserved.
DOI:10.5545/sv-jme.2018.5422
Original Scientific Paper
Received for review: 2018-04-13
Received revised form: 2018-08-13
Accepted for publication: 2018-08-20

Research on the Hill Start Assist of Commercial Vehicles Based on Electronic Parking Brake System

Pai Peng[1] – Hongliang Wang[1,*] – Xianhui Wang[1] – Weihua Wang[2] – Dawei Pi[1] – Tianle Jia[1]
[1] Nanjing University of Science & Technology, Department of Mechanical Engineering, China
[2] Nanjing University of Posts & Telecommunications, School of Electronic Science & Engineering, China

In this study, we aim to develop a logic threshold control framework to improve the hill-start assist quality of the commercial vehicles equipped with the electronic parking brake (EPB) system, while fulfilling the requirements of start safety. First, the desired pressure model and the EPB pneumatic model are constructed; the solenoid valve is controlled by the proposed scheme via the pulse width and frequency modulation (PWM-PFM) control signal according to the pressure error between the desired pressure and the actual pressure deduced from the EPB pneumatic model. Second, the controller is sufficiently evaluated in a variety of slopes, such as 8 %, 13 %, and 18 %, and is compared with two existing benchmark controllers in a co-simulation environment involving Matlab/Simulink and Trucksim. The simulation results demonstrate the hill-start effect and the reductions in the parking brake release delay, friction work and starting jerk. Finally, we further validate the effective implementation of the hill-start assist with the proposed controller on 8.2 %, 13 % and 20 % slopes in the vehicle experiment.

Keywords: hill-start assist, electronic parking brake, commercial vehicle, logic threshold control, co-simulation, experiments

Highlights

- *The control system is designed based on the investigation of the EPB pneumatic system.*
- *Simulation results of the hill start on several slopes indicate the effectiveness our scheme.*
- *Comparative outcomes with two existing controllers verify the benefits of our scheme in parking brake release delay, friction work and starting jerk.*
- *The actual vehicle experiment results further validate the proposed controller.*

0 INTRODUCTION

A frequent situation that causes a serious concern for drivers is starting the vehicle on a hill without any rollback. Hill-start depends on the driver's skill to coordinate with the brake, clutch, and throttle to achieve a smooth start [1], requiring considerable expertise and concentration from the driver [2]. The failure of performing such actions will result in engine stalling, even cause the vehicle to rollback, which leads to the risk of an accident, and may bring stress and panic to the driver. Even for the skilled driver, the frequent manoeuver will aggravate his/her fatigue and increase the possibility of failure [3]. Moreover, the vehicle parts are exposed to abnormal wear if excessive clutch slipping is created during the process in [4] and [5]. The hill-start assist (HSA) system provides the driver with the possibility of starting with safety and comfort by controlling the brake release process [6], without any complex operation and simultaneously avoiding the undesirable effect of vehicle rollback.

Many researchers have done a lot of work on HSA systems and developed different types of HSA systems. An HSA valve in [7] and [8], which is assembled between the master cylinder and the wheel cylinder, is utilized to retain the brake pressure to keep the vehicle stopped while the driver releases the brake pedal and requests enough engine torque to safely start in hill condition. In [9], the authors presented an HSA system for vehicles equipped with anti-lock brake system (ABS)/acceleration slip regulation (ASR) that keeps the brake forces on the wheels by communication with the ABS/ASR control unit, without necessity of keeping the brake pedal actuated. Researchers [10] to [12] investigated the electronic throttle technology on the automated mechanical transmission (AMT) -equipped vehicles; the accelerator pedal was only used to reflect the driver's intention, and the control unit increased the idle speed and engaged the clutch after the brake released. [13] to [15] proposed the hill-start implementation method of the EPB system. The HSA systems described above have been researched considerably mainly from the perspective of HSA function realization, but the control effect issue has not been considered thus far.

In conventional HSA control strategy, the brake starts to release until sufficient driving torque has been generated, which, however, causes excessive clutch friction work and jerk. Wang et al. [16] proposed the Bang-Bang control method of the hill-start functionality of EPB for commercial vehicles, which gradually releases the parking brake according to the increase in the driving torque. However, as

---

*Corr. Author's Address: Department of Mechanical Engineering, Nanjing University of Science & Technology, Nanjing, Jiangsu, China, whl343@163.com

the parking brake pressure increases, the difference between the two thresholds of the Bang-Bang control will increase and the control cycle will become longer accordingly, which leads to a decrease in the control precision and the release delay of the parking brake.

The primary objective of this study is to develop a logic threshold control framework to improve the hill start quality of an EPB-equipped commercial vehicle in hill start scenarios, while meeting the requirements of start safety. There are three important contributions that clearly distinguish our endeavor from the aforementioned literature:

1. First, the control system model is designed: the desired pressure model and EPB pneumatic system model are constructed; the vehicle model is formulated in Trucksim platform; the proposed controller responds to the pressure error and outputs PWM-PFM control signal for the solenoid valve to regulate the pressure in the parking brake chamber.
2. Second, the co-simulation platform is established involving Matlab/Simulink and Trucksim to verify the effectiveness of the proposed controller under different hill start conditions, including 8 %, 13 %, and 18 % slopes. Several criteria, including brake release delay, rollback distance, friction work and starting jerk, are considered to compare the control effect of the proposed scheme with two existing controllers.
3. Finally, the actual vehicle experiment is carried out on three different slopes, i.e. 8.2 %, 13 % and 20 %, to further demonstrate the effective implementation of our method.

The remainder of the paper is organized as follows: The description of the EPB system is introduced in Section 1. The logic threshold controller design is presented in Section 2, followed by the simulation and the experiment in Section 3. Conclusions are ultimately summarized in Section 4.

1 DESCRIPTION OF THE EPB SYSTEM

1.1 Working Principle

The architecture of the EPB for commercial vehicles is shown in Fig. 1. On the basis of the original parking brake system of commercial vehicles, the EPB system replaces the manual lever with a switch and adds a solenoid valve to the original pneumatic system. Several sensors have to be strategically positioned on the commercial vehicle to improve the control effectiveness of the HSA functionality of the EPB. Installed at the control port on the relay valve, the pressure sensor is used to indirectly sense the pneumatic pressure of the parking brake chamber. The Hall effect angle sensor is designed to measure the deflection of the suspension to calculate the rear axle load and to acquire the vehicle mass [17]. An accelerometer embedded in the electronic control unit (ECU) is expected to detect the road slope. The ECU receives signals including the switch, controller area network (CAN) bus, pressure sensor pressure feedback and hall effect angle sensor angle feedback necessary to determine the actuation control signal according to the control strategy.

When the driver pushes the switch to release, a signal is sent to the ECU and the ECU activates the solenoid valve to allow compressed air from the air reservoir to go the control port on the relay valve, which opens the delivery ports on the relay valve and then enables the release of the pressurised air already available at the supply port to the parking brake chambers.

As the switch is pulled to apply, any air between the relay valve control port and the solenoid valve is discharged to the atmosphere via the solenoid valve. Then, the air supply from the supply port to the delivery port of the relay valve is cut, and the compressed air in the parking brake chambers is exhausted through the relay valve's exhaust port, assuring the parking brake.

When the vehicle is about to be driven away on a slope, the EPB system's logic checks all the requirements needed to control the release process of the parking brake automatically.

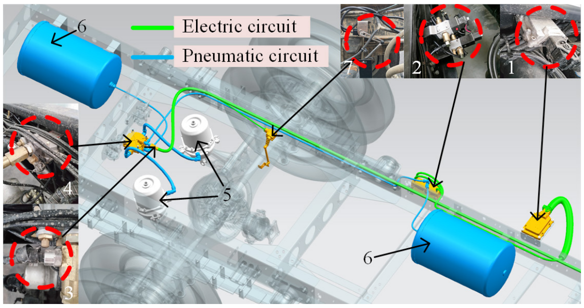

Fig. 1. *Architecture of the EPB for commercial vehicles; 1) ECU, 2) solenoid valve, 3) pressure sensor, 4) relay valve, 5) parking brake chamber, 6) air tank, 7) hall effect angle sensor*

1.2 Pneumatic Characteristics

Fig. 2 shows that with the initial pressure P_{in} in the parking brake chamber, the solenoid valve is set to open t_o to allow the compressed air to pressurise the brake chamber. However, because of the response lag of the solenoid valve and the inertia effect of the compressed air, there is a delay and over-inflation in the EPB system.

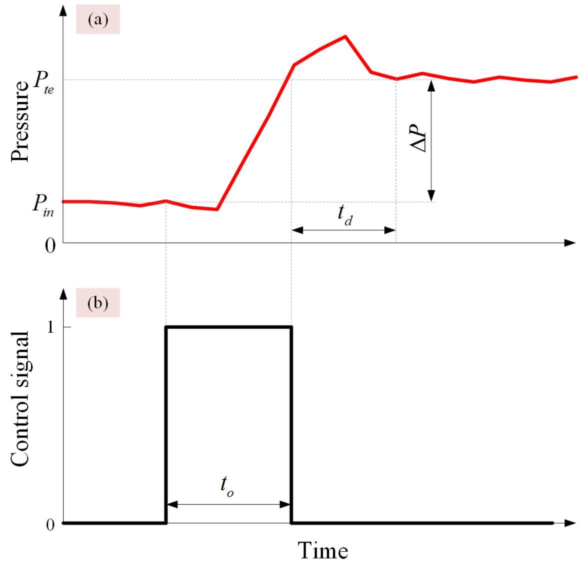

Fig. 2. *Typical experimental results; a) brake chamber pressure, and b) control signal of the solenoid valve*

With a large number of experiments, the delay time t_d is identified to be approximately 40 ms. The pressure increase value ΔP between before and after the switching action of the solenoid valve decreases with an increase in the initial pressure. Furthermore, the magnitude of ΔP decides the control mode of the solenoid valve, only when it is in a certain range can the servo control be realized, which will be further discussed in Section 2.

2 CONTROL SYSTEM DESIGN

The block diagram of the proposed control system is depicted in Fig. 3. This control system structure contains the desired pressure model, logic threshold controller, EPB pneumatic system model and Trucksim vehicle model. The desired pressure and the actual pressure in the parking brake chamber are denoted by P_d and P, respectively; their error is represented by e. The PWM-PFM control signal for the solenoid valve is referred to as S. T_d and i_g from the Trucksim vehicle model are the driving torque and the transmission gear ratio, respectively. The main objective of the proposed control system is to make the actual pressure to follow the desired values obtained from the desired pressure model, thereby reducing the release delay of the parking brake. The logic threshold controller responds to the input pressure error and outputs the PWM-PFM control signal for the solenoid valve.

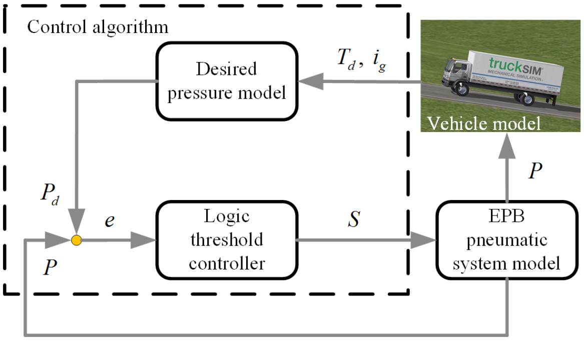

Fig. 3. *Block diagram of proposed control system*

2.1 Desired Pressure Model

Fig. 4 shows that the brake force F_{Xb} generated by the parking brake actuators decreases with an increase in the driving force F_t during the hill-start process **[18]**. The parking brake, ideally, should be released entirely at time t_1 where the driving force F_t just overcomes the gradient resistance F_i; if it is not released in time, e.g. the parking brake is applied continuously until the time t_2, the brake force F_{Xb} will develop into the resistance of the vehicle forward movement during the time period t_1 to t_3. A very delayed release of the parking brake in the starting manoeuvre leads to the retardation of the start, creating excessive clutch slipping and serious jerks, which enhances the need for reducing or even eliminating the release delay of the parking brake, under the prerequisite of no rollback, to improve the control effect of the HSA. To capture this requirement, a suitably tailored control strategy for diminishing the brake release delay is proposed to regulate the release process of the parking brake, i.e., releasing the brake gradually as the driving force F_t, in other words, the driving torque T_d, increases.

A simplified parking brake system model is developed for the convenience of study. The maximum brake force $F_{Xb\max}$ of the parking brake system is expected to be equal to the gradient resistance $F_{i\max}$ on the maximum slope $\alpha_{\max}$ on which vehicle can stop safely, where the pressure P of the parking brake chamber is 0. The magnitude of the maximum brake force $F_{Xb\max}$ can be derived as follows:

$$F_{Xb\max} = mg\sin\alpha_{\max}. \tag{1}$$

When the parking brake is completely released, the pressure in the parking brake chamber is P_0.

The vehicle parking brake system model is thereby simplified as follows:

$$F_{Xb} = F_{Xb\max} - F_{Xb\max} \cdot P / P_0. \tag{2}$$

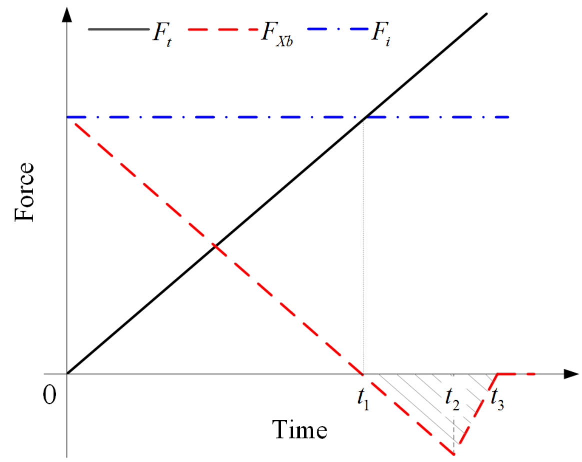

Fig. 4. *Forces in the hill-start process*

When the vehicle is starting on a low slope α, which is less than $\alpha_{\max}$, the maximum brake force $F_{Xb\max}$ that the parking brake actuator can provide is greater than the gradient resistance F_i. Here, to shorten the release delay of the parking brake, a certain amount of compressed air P_1 released into the parking brake chamber under the premise of a safety start.

$$P_1 = \frac{F_{Xb\max} - F_i}{F_{Xb\max}} \cdot P_0. \tag{3}$$

As mentioned above, the parking brake should be released entirely when the driving force F_t exceeds the gradient resistance F_i in the ideal case. Hence, the following equality has to be fulfilled:

$$F_t = T_d i_g i_0 \eta_T / r = mg \sin\alpha = F_i. \tag{4}$$

When the driving torque T_d is greater than the demand torque T_i, the solenoid valve is opened to rapidly pressurise the brake chamber to reduce the brake release delay. The demanded torque T_i is derived from Eq. (4) as given in Eq. (5):

$$T_i = \frac{mg \sin\alpha r}{i_g i_0 \eta_T}. \tag{5}$$

The desired pressure P_d is assumed to be proportional to the driving torque T_d such that

$$P_d = P_1 + (P_0 - P_1) \cdot T_d / T_i. \tag{6}$$

Therefore, the vitally influencing factor in the implementation of the HSA functionality of the EPB-equipped commercial vehicles is to adopt the appropriate control strategy for the solenoid valve, in which the parking brake chamber pressure P will effectively follow the desired pressure P_d.

2.2 EPB Pneumatic System Model

As the solenoid valve is the core component of the EPB system, its dynamic characteristics play a significant role in the performance of the EPB system. When implementing the HSA manoeuver, the solenoid valve of the EPB system can be regarded as an on/off valve, regulating the air flow to the parking brake chamber by an open/close action.

The dynamic of the solenoid valve **[19]** includes the electrical circuit model, the magnetic circuit model and the dynamic model of the mechanical components. The electrical circuit model is expressed as follows:

$$U = IR + N\frac{\mathrm{d}\Phi}{\mathrm{d}t}. \tag{7}$$

According to Kirchhoff's law, the magnet circuit model is written as follows:

$$IN = \frac{\delta\Phi}{\mu A_c}. \tag{8}$$

The dynamic model of the mechanical components can be derived as follows:

$$\ddot{x} = \frac{1}{m_s}\left[\frac{\Phi^2}{2\mu A_c} - P_s A_s - K_s(x + x_p) - c\dot{x}\right]. \tag{9}$$

Assuming that air is an ideal gas, heat transfer from the valve orifice is negligible, and shear forces on the walls of the orifice are negligible, the dynamic of the parking brake chamber can be mathematically formulated as follows **[20]**:

$$\frac{dP}{dt} = 0.0405 C_d C_A x \frac{P_{us}}{\sqrt{T}}, \text{ if } \frac{P_{us}}{P_{ds}} \le P_{cr}, \tag{10}$$

$$\frac{dP}{dt} = C_d C_A x \frac{P_{us}}{\sqrt{T}} \left(\frac{2\gamma}{R_{gs}(\gamma - 1)} \left(\left(\frac{P_{us}}{P_{ds}}\right)^{\frac{2}{\gamma}} - \left(\frac{P_{us}}{P_{ds}}\right)^{\frac{\gamma+1}{\gamma}} \right) \right)^{\frac{1}{2}}$$

$$\text{if } \frac{P_{us}}{P_{ds}} \ge P_{cr}. \tag{11}$$

The EPB pneumatic system model is illustrated in Fig. 5, and the main parameters of the pneumatic system are listed in Table 1.

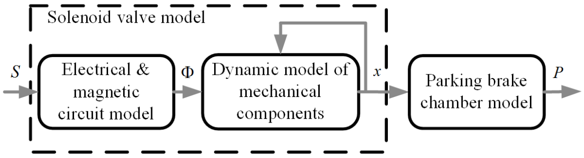

Fig. 5. *EPB pneumatic system*

Table 1. *Main parameters of EPB pneumatic system*

Parameter	Value	Parameter	Value
U	24	N	900
R	41	x_p	1.2×10^{-3}
μ	$4\pi\times10^{-7}$	δ	2×10^{-3}
A_c	4.72×10^{-5}	c	0.26
K_s	0.77×10^{-3}	m_s	0.02 kg

2.3 Logic Threshold Controller

From the above analysis, we know that the challenge in the implementation of the HSA is to maintain the desired pressure calculated in Eq. (6); hence, a quick response control strategy of the solenoid valve should be adopted. The logic threshold control method is firstly introduced to the HSA of EPB-equipped commercial vehicles since it only requires to set the reasonable threshold values according to the system characteristics and no need for establishing complex control model, which is suitable for the nonlinear systems. Once the reasonable threshold values are determined, a satisfactory control performance can be obtained. Moreover, it has a strong practicability.

First, according to the pneumatic characteristics of the EPB discussed in Section 1, the delay time t_d is maintained at around 40 ms for the different opening times of the solenoid valve. Therefore, t_d is used as the closing time in one control period. The PWM-PFM is introduced to control the on/off action of the solenoid valve as it can regulate the duty cycle and the frequency of the control signal at the same time, i.e., by modifying the length of the opening time with the closing time unchanged to regulate the inflation rate and the pressure increase value of the pneumatic system.

The logic threshold control strategy is designed to control the on/off action of the solenoid valve on the basis of the pressure error e between the desired pressure P_d and the actual pressure P in the parking brake chamber, as shown in Fig. 6. Three logic threshold values P_d-e_1, P_d-e_2, and P_d-e_3 $(e_1<e_2<e_3)$ are set, and each corresponds to the fixed duty cycle and period of the PWM-PFM control of the solenoid valve. When $e\geq e_3$, there is a large duty cycle and period of the PWM-PFM control to narrow the error; when $e_2\leq e<e_3$, the medium duty cycle and period of PWM-PFM control is utilized; and when $e_1\leq e<e_2$, the small duty cycle and period of PWM-PFM control is designed to precisely track the desired value.

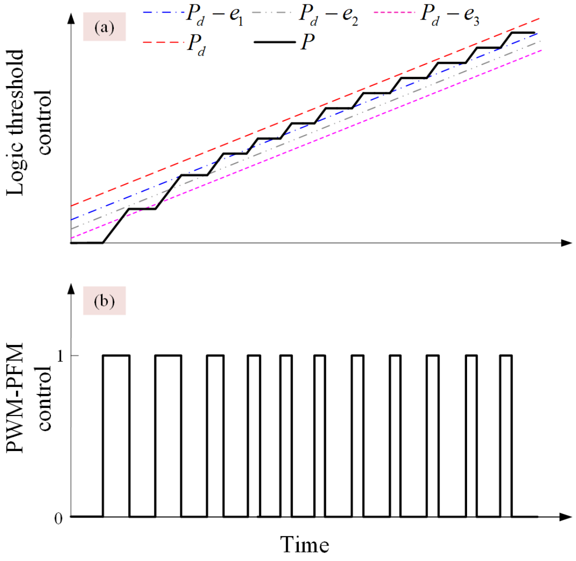

Fig. 6. *HSA control strategy; a) Logic threshold control, and b) PWM-PFM control*

2.4 Criteria

At present, the commonly used evaluation criteria for hill-start include the rollback distance, friction work and starting jerk.

If the vehicle rolls to the unintended direction, there is a risk of accident. To ensure the safety start of the vehicle, the rollback distance is expected to be 0.

The friction work is the magnitude of the friction work between the pressure plate and the clutch disk in the vehicle start process, influencing the clutch life and reliability. It is calculated using Eq. (12) in **[21]**, as follows:

$$L=\int_0^t T_c(t)[\omega_e(t)-\omega_c(t)]dt. \tag{12}$$

The starting jerk J, given by Eq. (13), is the change rate of the longitudinal acceleration of the vehicle, indirectly reflecting the ride comfort of the vehicle.

$$J=\frac{da}{dt}. \tag{13}$$

3 SIMULATION AND EXPERIMENT

3.1 Simulation

To evaluate the performance of the HSA control strategy, a vehicle model is conducted on the Trucksim platform; the main parameters of the vehicle are listed in Table 2. The HSA controller and the EPB system model are designed on the Matlab/Simulink platform; a co-simulation platform is thereby constructed on the basis of the Matlab/Simulink and Trucksim platforms to emulate the hill-start scenarios.

Table 2. *Main parameters of the vehicle*

Parameter	Value
m	8190
r	397
i_g	6.315
i_0	4.875
η	0.99

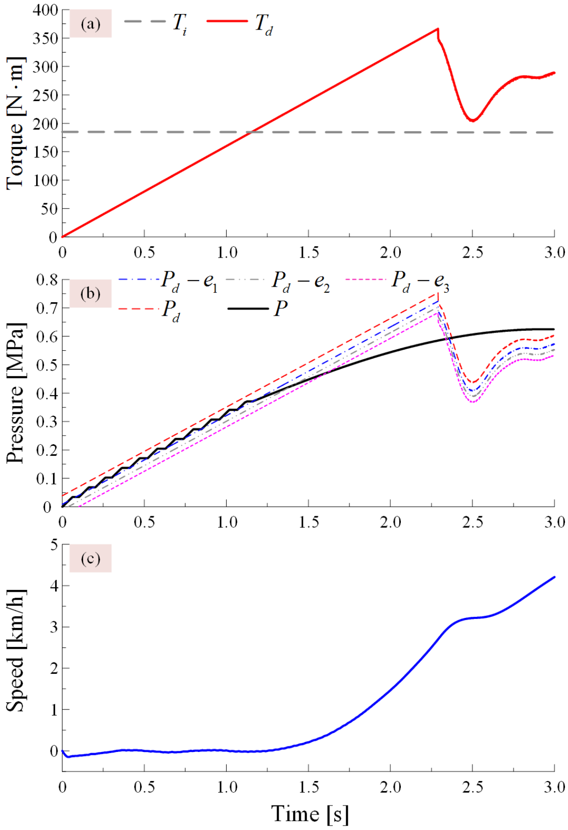

Fig. 7. *Simulation results of 18 % slope; a) torque, b) pressure, and c) speed*

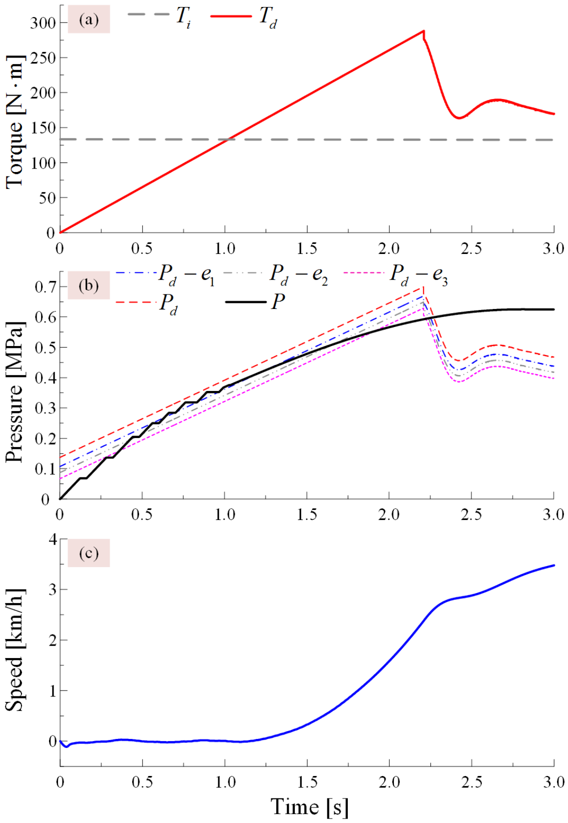

Fig. 8. *Simulation results of 13 % slope; a) torque, b) pressure, and c) speed*

This section firstly describes the simulation results under three different slope conditions, i.e., 18 %, 13 %, and 8 %. When the vehicle is about to start on the 18 % slope, as shown in Fig. 7, the proposed control ensures effective tracking of the desired pressure. When the driving torque just overcomes the demand torque at 1.16 s, the solenoid valve is opened to fast inflate and rapidly release the parking brake. At 1.25 s, the vehicle velocity starts to increase from 0, suggesting that the logic threshold controller can implement the HSA function of the EPB.

The simulation results on 13 % and 8 % slopes are demonstrated in Fig. 8 and Fig. 9, respectively. It can be seen that the proposed scheme can achieve fast tracking of the desired pressure P_d and is able to implement the HSA functionality, verifying the robustness and effectiveness of the logic threshold controller.

The performance of the HSA with the proposed logic threshold controller is compared with that of the two existing ones, namely, the conventional controller developed in [8] and the bang-bang designed in [16]. The bang-bang controller employs the same desired pressure P_d as that of the proposed controller with two threshold values of 0.9 P_d and 0.7 P_d. As shown in Fig. 10, when the pressure P is below 0.7 P_d, the solenoid valve is opened to release the parking brake; when the pressure P reaches 0.9 P_d, the solenoid valve is closed to maintain the pressure.

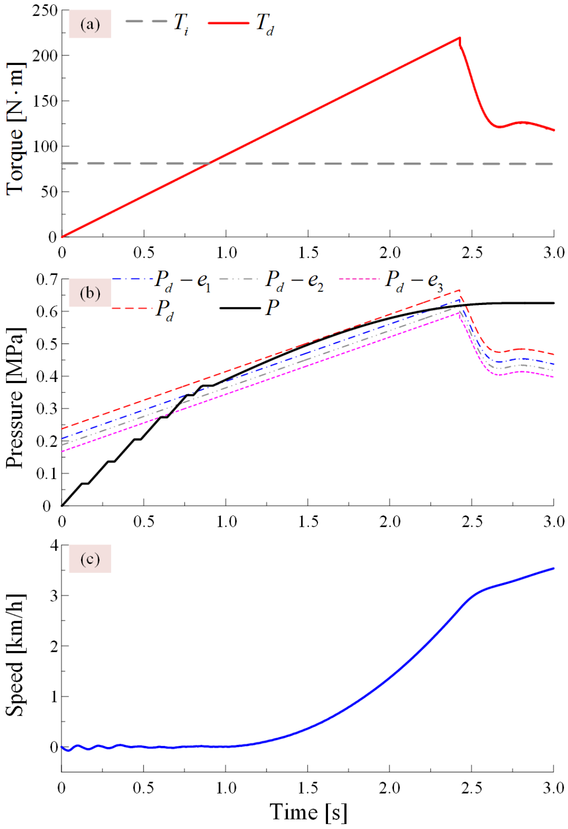

Fig. 9. *Simulation results of 8 % slope; a) torque, b) pressure, and c) speed*

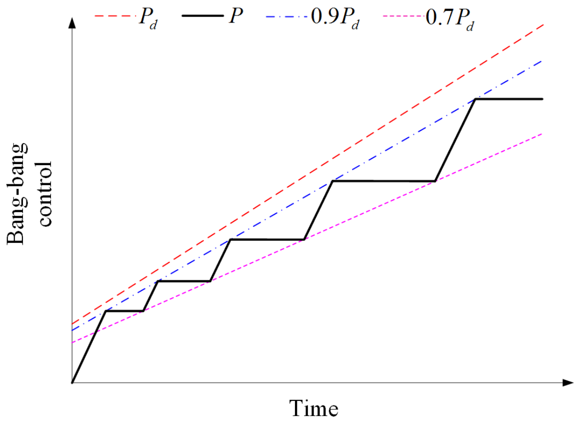

Fig. 10. *Bang-bang control*

Figs. 11 and 12 illustrate the comparative outcomes of the three controllers on 18 % slope. As depicted in Fig. 11, the parking brake release delay of our scheme, bang-bang control, and conventional control are 0.12 s, 0.29 s, and 0.79 s, respectively, showing that the proposed control ensures effective tracking of the desired pressure with a small release delay.

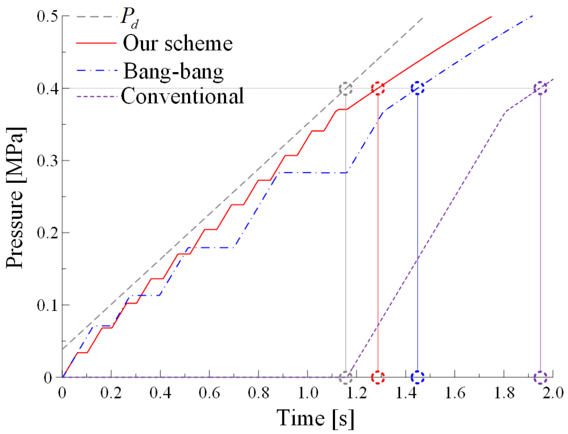

Fig. 11. *Comparison with the conventional and the bang-bang schemes in the inflation process*

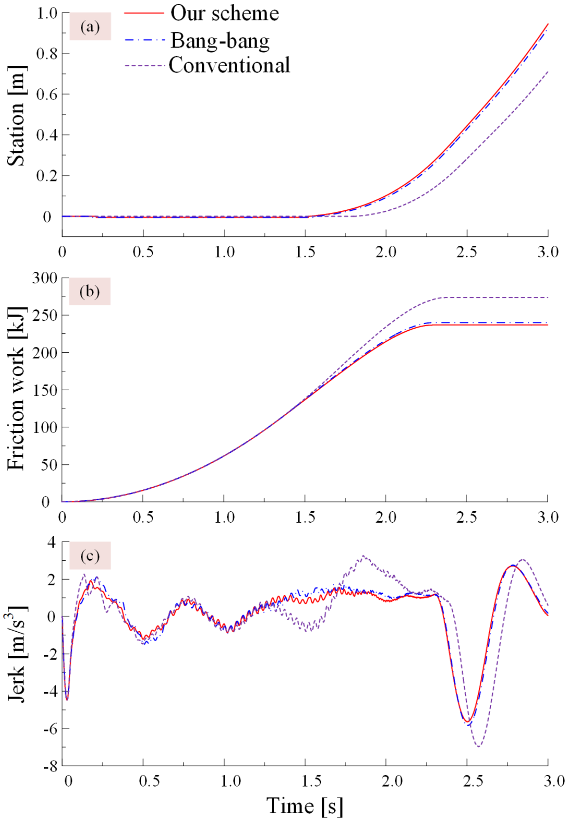

Fig. 12. *Comparison with conventional and bang-bang schemes in terms of the following criteria; a) rollback distance, b) friction work, and c) starting jerk*

Fig. 12a shows that there is no rollback with the conventional control, and bang-bang and the logic threshold controller both have an unnoticeable rollback distance of 0.005 m, which suggests that all of the above controllers meet the safety requirements. At the same time, it can be seen that the vehicle starts faster under the proposed controller. The comparative results in terms of the friction work are shown in Fig. 12b. It is evident that the conventional controller generates more clutch friction because of the longest release delay of the parking brake. The increases in the friction work are 15.43 % and 1.38 % in the cases of the conventional and the bang-bang controller, respectively. In Fig. 12c, the proposed scheme outshines its two counterparts from the perspective of the starting jerk. A clearer comparison can be achieved by using the root mean square (RMS) values of the starting jerk. The comparison of HSA criteria for three controllers is summarized in Table 3. It can be discerned that the proposed controller evidently outperforms bang-bang control and conventional control in aspects of brake release delay, clutch friction work, and starting jerk under all three slopes.

Table 3. *Comparison of HSA performance for three controllers*

Slope	Controller	Brake release delay [s]	Friction work [kJ]	*Starting jerk [-]	Rollback distance [m]
8 %	Proposed	0.11	124.46	1.03	0
	Bang-bang	0.25	126.16	1.06	0
	Conventional	0.79	142.81	1.14	0
13 %	Proposed	0.13	161.21	1.22	0
	Bang-bang	0.27	162.85	1.31	0
	Conventional	0.79	185.90	1.60	0
18 %	Proposed	0.12	236.63	1.65	0.005
	Bang-bang	0.29	239.89	1.75	0.005
	Conventional	0.79	273.15	2.06	0

*RMS value

3.2 Experiment

To further verify the effectiveness of the logic threshold controller, the experiment is performed on a commercial vehicle equipped with EPB introduced in section 1. The actual test vehicle employs the same parameters as those in Table 2. The experimental setup is shown in Fig. 13, the vehicle implements the HSA functionality on three different slopes, i.e., 20 %, 13 % and 8.2 %; the vehicle state signals are sent to CAN from the ECU of the EPB; a data acquisition program is developed in PC to acquire the real-time displaying and storing of the signals transmitted on CAN.

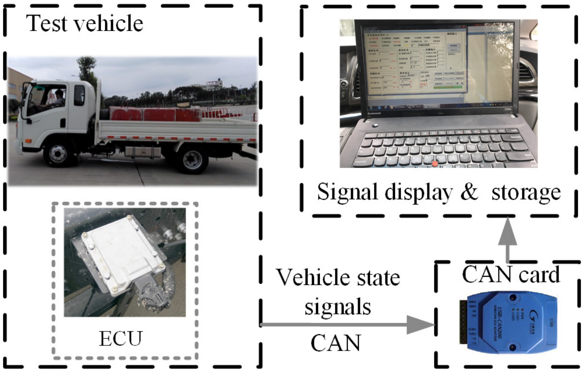

Fig. 13. *Experimental setup*

Fig. 14 shows the experimental results of 20 % slope: at first, the vehicle is stopped on the gradient; as the driving torque increases, the driver's starting intention is confirmed by the system and the solenoid valve is therefore opened to inflate. With the proposed logic threshold control, the pressure increases with an increase in the desired pressure, triggering the corresponding PWM-PFM control of the solenoid valve when encountering different thresholds. The

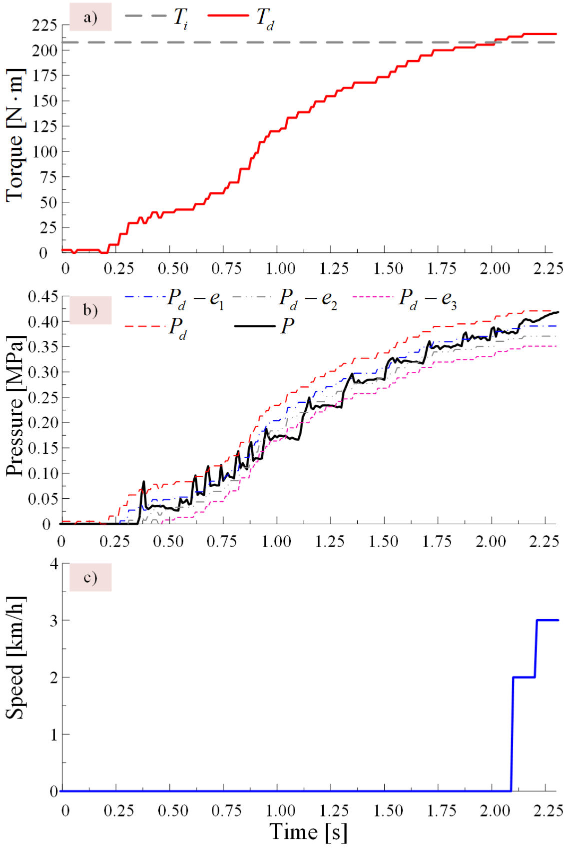

Fig. 14. *Experiment results of 20 % slope; a) torque, b) pressure, and c) speed*

driving torque overcomes the demand torque at 3.01 s, and then, the EPB system rapidly inflates. After 3.10 s, the vehicle velocity is gradually increased from 0, implying a successful HSA implementation. The parking brake is completely released when the pressure reaches 0.4 MPa at 3.15 s with a release delay of 0.14 s, which is sufficiently small. The pressure follows the desired pressure effectively, and no rollback of the vehicle is observed during the entire hill-start process.

Similar experimental results can be found in Figs. 15 and 16. It is clear that the proposed controller enables the pressure to track the desired pressure effectively and the HSA functionality of EPB-equipped commercial vehicle is effectively implemented on 13 % and 8.2 % slopes. A closer examination reveals that the release delay of the parking brake are 0.11 s and 0.09 s on 13 % and 8.2 % slope, respectively.

All of the above results demonstrate that the proposed logic threshold controller provides a satisfactory HSA performance of commercial vehicles equipped with EPB, and the parking brake release delay is sufficiently small, thereby reducing the clutch wear and the starting jerk.

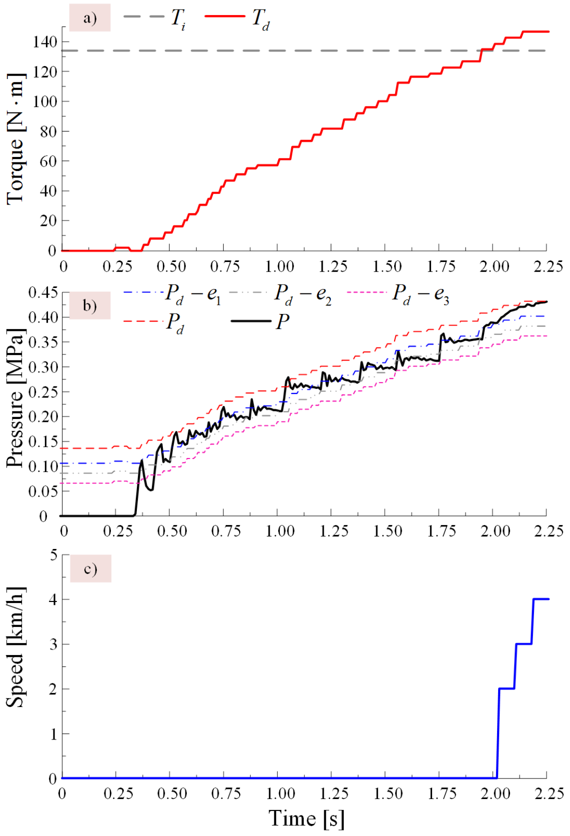

Fig. 15. *Experiment results of 13 % slope; a) torque, b) pressure, and c) speed*

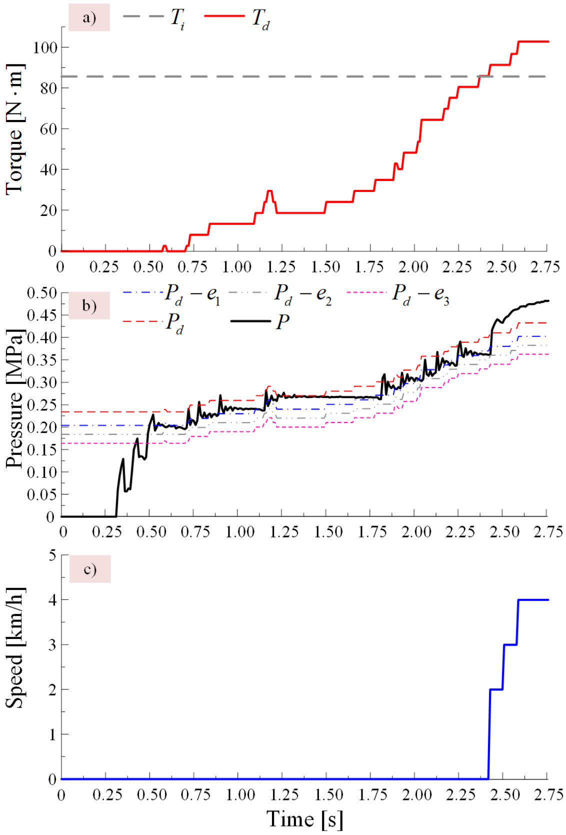

Fig. 16. *Experiment results of 8.2 % slope; a) torque, b) pressure, and c) speed*

4 CONCLUSIONS

In this study, we developed a logic threshold control framework to improve the hill-start quality of EPB-equipped vehicles under the prerequisite of safety start. In the control synthesis, the desired pressure model and EPB pneumatic system model were developed, and then, the proposed controller was constructed to control the solenoid valve according to the pressure error between the desired pressure and the actual pressure.

The simulation results verified the hill-start control effect, and the comparative results showed that the proposed controller outperformed the conventional and bang-bang controllers in terms of the brake release delay, friction work and starting jerk, which demonstrated that the proposed controller was capable of improving the hill-start quality of EPB-equipped vehicles.

The vehicle experiment results further demonstrated that the proposed scheme could effectively implement the hill-start assist of the EPB-equipped vehicle without rollback and track the desired pressure with a small tracking error.

One direction to extend this work is to develop a recognition algorithm of the vehicle mass during the hill-start manoeuver to improve the identification precision and reduce cost.

5 ACKNOWLEDGEMENTS

This work was supported by the National Natural Science Fund of China (grant number 51205209,51205204), Project of Jiangsu Provincial Six Talent Peaks (grant number 2016-JXQC-020), Fundamental Research Funds for the Central Universities (grant number 309171B8811), China Scholarship Council Funds (grant number 201606845008).

6 NOMENCLATURES

a	longitudinal acceleration, [ms^{-2}]
A_c	cross-sectional area of air gap, [m^2]
A_s	cross-sectional area of spool, [m^2]
c	viscous friction coefficient, [-]
e	pressure error, [MPa]
F_i	gradient resistance, [N]
$F_{i\max}$	maximal gradient resistance, [N]
F_t	driving force, [N]
F_{Xb}	brake force, [N]
$F_{Xb\max}$	maximal brake force, [N]
g	gravitational acceleration, [ms^{-2}]
i_g	transmission gear ratio, [-]
i_0	differential ratio, [-]
I	coil current, [A]
J	starting jerk, [ms^{-3}]
K_s	spring stiffness, [Nm^{-1}]
L	friction work, [J]
m	vehicle mass, [kg]
m_s	spool mass, [kg]
N	number of coils, [-]
P	actual pressure, [MPa]
P_{cr}	critical pressure ratio, [-]
P_d	desired pressure, [MPa]
P_{ds}	downstream pressure, [MPa]
P_{in}	initial pressure, [MPa]
P_s	supply pressure, [MPa]
P_{us}	upstream pressure, [MPa]
P_0	release pressure, [MPa]
ΔP	pressure increase, [MPa]
r	tyre rolling radius, [m]
R	equivalent resistance, [Ω]
R_{gs}	ideal gas constant, [-]
S	PWM-PFM control signal, [-]
t	lock-up time of the clutch, [s]
t_d	delay time, [s]
t_o	opening time, [s]
T_c	clutch torque, [N·m]
T_d	driving torque, [N·m]
T_i	demand torque, [N·m]
U	driving voltage, [V]
x	spool displacement, [m]
x_p	spring pre-compression, [m]
μ	air permeability, [Hm^{-1}]
ω_e	engine speed. [r·min^{-1}]
ω_c	speed of the clutch disk, [r·min^{-1}]
Φ	magnetic flux, [Wb]

7 REFERENCES

[1] Sharma, A., Gangwar, H., Dabhole, D., Pathak, S., Dwivedi, V., and Nigam, A. (2016). Hill start assistance developed for buses equipped with AMT. *SAE 2016 World Congress and Exhibition*, **DOI:10.4271/2016-01-1111**.

[2] Balasubramanian, B. (2015). Sensor-less hill-assist using traction control in electric LCV. *IEEE International Transportation Electrification Conference*, p. 1-7, **DOI:10.1109/ITEC-India.2015.7386921**.

[3] Subramanian, S., Thangavel, P., Safna, F.M.I., Sornam, K., Rambhaji, G.P., Velusamy, R. (2015). Development and testing of a control algorithm to assist drive-off in the gradient-a rapid control prototyping approach. *SAE Technical Paper*, **DOI:10.4271/2015-26-0002**.

[4] Petrun, T., Flašker, J., Kegl, M. (2013). A Theoretical and numerical study of an additional viscosity term in a modified elasto-plastic friction model for wet friction clutch simulations. *Strojniški vestnik - Journal of Mechanical Engineering*, vol. 59, no. 7-8, p. 358-366, **DOI:10.5545/sv-jme.2012.920**.

[5] Kakinuma, Y., Aoyama, T., Anzai, H. (2007). Development of the variable friction clutch applying the functional medium. *Strojniški vestnik - Journal of Mechanical Engineering*, vol. 53, no. 11, p. 755-770.

[6] Ohkubo, N., Matsushita, S., Ueno, M., Akamine, K., Hatano, K. (2013). Application of electric servo brake system to plug-in hybrid vehicle. *SAE International Journal of Passenger Cars - Electronic and Electrical Systems*, vol. 6, no. 1, p. 255-260, **DOI:10.4271/2013-01-0697**.

[7] Paulo, B., Claudinei, B., Alberto, B. (2013). Innovative hill start assistance device. *22nd SAE BRASIL International Congress and Display*, p. 748-754.

[8] Ge, A., Lei, Y., Gao, Y., Zhang, H. A. (1998). A research on hill starting control of AMT system of vehicle. *Automotive Engineering*, vol. 20, no. 3, p. 150-155.

[9] Travaglia, C., de Souza, L., Ferreira, P., Ferreira, R. da Silva, M., de Abreu, L. (2015). Improved hill start aid system for commercial vehicles equipped with automated transmission, *24th SAE Brasil International Congress and Display*.

[10] Lu, T., Dai, F., Zhang, J., Wu, M. (2012). Optimal control of dry clutch engagement based on the driver's starting intentions. *Proceedings of the Institution of Mechanical Engineers, Part*

D: Journal of Automobile Engineering, vol. 226, no. 8, p. 1048-1057, **DOI:10.1177/0954407011435465**.

[11] Li, L., Zhu, Z., Wang, X., Yang, Y., Yang, C., Song, J. (2015). Identification of a driver's starting intention based on an artificial neural network for vehicles equipped with an automated manual transmission. *Proceedings of the Institution of Mechanical Engineers, Part D: Journal of Automobile Engineering*, vol. 230, no. 10, **DOI:10.1177/0954407015611294**.

[12] Gao, B.Z., Chen, H., Lu, X.H., Sanada, K. (2013). Improved optimal controller for start-up of AMT trucks in consideration of driver's intention. *International Journal of Automotive Technology*, vol. 14, no. 2, p. 213-220, **DOI:10.1007/s12239-013-0024-0**.

[13] Wang, H.L., Yuan, Q.Z., Zhong, H.X., Pi, D.W. (2014). Research on the hill-start auto control for the vehicles with EPB. *Transactions of Beijing Institute of Technology*, vol. 34, no. 4, p. 344-348. (in Chinese)

[14] Delvecchio, D., Savaresi, S.M., Spelta, C., Dozio, S., Mandrioli, L., Cantoni, C. (2009). A control system for hill start assistance for commercial vehicles. *ASME Dynamic Systems and Control Conference*, p. 517-524, **DOI:10.1115/DSCC2009-2728**.

[15] Slosarczyk, K., Linden, J. G., Burnham, K. J., Cockings, K., Capolongo, R. (2008). Implementation of an electronic park brake feature with limited data availability. *International Conference on Systems Engineering*, p. 254-259, **DOI:10.1109/ICSEng.2008.92**.

[16] Wang, H.L., Gu, W.H., Zhang, Q.K., Wang, E.L. (2017). Research on bang-bang control of EPB system in vehicle hill start. *Transactions of Beijing Institute of Technology*, vol. 37, no. 1, p. 46-49, **DOI:10.15918/j.tbit1001-0645.2017.01.010**. (in Chinese)

[17] Wang, H.L., Li, M.Y., Jia, T.L. (2017). *Vehicle mass measurement method and device based on suspension compression*. Patent application CN 106679782 A, State Intellectual Property Office of the People's Republic of China, Beijing. (in Chinese)

[18] Wang, H.L., Zhang, Q.K., Gu, W.H. (2017). Simulation and experiment study on hill start control based on PID control. *Automotive Engineering*, vol. 39, no. 4, p. 480-485, **DOI:10.19562/j.chinasae.qcgc.2017.04.017**. (in Chinese)

[19] Kong, X.W., Li, S.Z. (2014). Dynamic performance of high speed solenoid valve with parallel coils. *Chinese Journal of Mechanical Engineering*, vol. 27, no. 4, p. 816-821, **DOI:10.3901/CJME.2014.0513.091**.

[20] He, L., Wang, X., Zhang, Y., Wu, J., Chen, L. (2011). Modeling and simulation vehicle air brake system. *Proceedings 8th Modelica Conference*, p. 430-435, **DOI:10.3384/ecp11063430**.

[21] Zhao, S., Hilmas, G.E., Dharani, L.R. (2008). Behavior of a composite multidisk clutch subjected to mechanical and frictionally excited thermal load. *Wear*, vol. 264, no. 11-12, p. 1059-1068, **DOI:10.1016/j.wear.2007.08.012**.

List of reviewers who reviewed manuscripts in 2018

Miklós Ákos, Hungary
Zaini Bin Ahmad, Malaysia
Narendra Akhadkar, France
Cetin T. Akinci, Turkey
Esther T. Akinlabi, South Africa
Izzat Al-Darraji, Turkey
Hafiz Muhammad Ali, Pakistan
Khalil Alipour, Iran
Wael G. Al-Kouz, Jordan
Fabrício Alves De Almeida, Brazil
Aziz Hakan Altun, Turkey
Sebhi Amar, Algeria
Andreas Archenti, Sweden
Fatahul Arifin, Taiwan, Republic of China
Kamil Arslan, Turkey
Viktor P. Astakhov, USA
Matjaž Četina, Slovenia
Franci Čuš, Slovenia
Joze Balic, Slovenia
Mustapha Barakat, France
Robert Bauer, Canada
Branko Bauer, Slovenia
Bernd Baufeld, UK
Károly Beneda, Hungary
Anton Bergant, Slovenia
Tomaž Berlec, Slovenia
Matej Biček, Slovenia
Ignacijo Biluš, Slovenia
Miha Bobic, Slovenia
Miha Boltežar, Slovenia
Éd Claudio Bordinassi, Brazil
Marek Boryga, Poland
Tomaž Brajlih, Slovenia
Charles-Henri Bruneau, France
Helena Burger, Slovenia
Matthias H. Buschmann, Germany
Michele Calì, Italy
Marina Campolo, Italy
Michele Carboni, Italy
Arnaldo Casalotti, Italy
Paolo Casoli, Italy
Kadir Cavdar, Turkey
Onur Çavuşoğlu, Turkey
Gregor Čepon, Slovenia
Yikai Chen, Chen
Peng Cheng, USA
Filippo Cianetti, Italy
Snezana Ciric-Kostic, Serbia
Paul Colegrove, UK
Franco Concli, Italy
Çağlar Conker, Turkey
José Gilberto Dalfré Filho, Brazil
Aydin Dönmez, Turkey
J. Paulo Davim, Portugal
Massimiliano De Agostinis, Italy
Luis Norberto López De Lacalle Marcaide, Spain
Anderson Paulo De Paiva, Brazil
Mihael Debevec, Slovenia
Lawrence Deepak, India
Marco Dell'Isola, Italy
Pinar Aydan Demirhan, Turkey
Janez Diaci, Slovenia
Baila Diana Irinel, Romania
Burak Dikici, Turkey
Zlate Dimkovski, Sweden
Anselmo Eduardo Diniz, Brazil
Mateja Dovjak, Slovenia
Idriss El-Thalji, Norway
Selcuk Erkaya, Turkey
Ron Faller, USA
Imre Felde, Hungary
Mirko Ficko, Slovenia
Tomasz Figlus, Poland
Rastko Fišer, Slovenia
Wolfgang Fricke, Germany
Tomislav Galeta, Croatia
Andrés Gabriel García, Argentina
Steven Garrett, USA
Ehsan Ghassemali, Singapore
Alfredo Gilbert, Mexico
Gilbert-Rainer Gillich, Romania
Srečko Glodež, Slovenia
Adam Glowacz, Poland
Sandro Goñi, Argentina
Emil Goettlich, Austria
Guilherme Ferreira Gomes, Brazil
Aleš Gosar, Slovenia
Janez Grum, Slovenia
Lucjan Gucma, Poland
Recep Gunes, Turkey
Huseyin Gurbuz, Turkey
Leo Gusel, Slovenia
Jiří Hájek, Czech Republic
Ales Hace, Slovenia

Reinhard Hackenschmidt, Germany
Miroslav Halilovič, Slovenia
Guangbo Hao, Ireland
Boštjan Harl, Slovenia
Simon A. Hayes, UK
Mario Hirz, Austria
Marko Hočevar, Slovenia
Matija Hoić, Croatia
Alexander Hošovský, Slovakia
Richárd Horváth, Hungary
Evangelos Vasileios Hristoforou, Greece
Soichi Ibaraki, Japan
Jamshed Iqbal, KSA
Md. Zohurul Islam, Bangladesh
Smutny Jaroslav, Czech Republic
Marko Jerman, Slovenia
Matteo Kalchschmidt, Italy
Uroš Karadžić, Slovenia
Irfan Karagoz, Turkey
Fatih Karpat, Turkey
Mitja Kastrevc, Slovenia
Marko Kegl, Slovenia
Tomaž Kek, Slovenia
Iyas Khader, Germany
Andrzej Kiełbus, Poland
Turgay Kivak, Turkey
Jernej Klemenc, Slovenia
Peder Klit, Denmark
Damjan Klobčar, Slovenia
Davorin Kofjac, Slovenia
Ergun Korkmaz, Turkey
Kari Koskinen, Finland
Attila Kovari, Hungary
Djordje Gojmir Kozic, Serbia
Grzegorz M. Krolczyk, Poland
Jurij Krope, Slovenia
Jan Kudlaček, Czech Republic
Janez Kušar, Slovenia
Robert Kunc, Slovenia
Marjan Leber, Slovenia
Vincent W. Lee, USA
Martin Leitner, Austria
Hirpa G. Lemu, Norway
Zsófia Lendek, Romania
Tadeusz Leppert, Poland
Mariusz Lewandowski, Poland
Junning Li, China
Yaoyao Liao, China
Barbara S. Linke, USA
Alexander Lion, Germany
Edward Lisowski, Poland
Huibin Liu, USA
Yingxiang Liu, China
Gorazd Lojen, Slovenia
Franco Lombardi, Italy
Darko Lovrec, Slovenia
Alessandro Maccarini, Denmark
Thiago Pandim Barbosa Machado, Brazil
Sotiris Makris, Greece
Pierre-Yves Manach, France
Tamás Mankovits, Hungary
Laura Marcheggiani, Italy
Boštjan Markoli, Slovenia
Angelos P. Markopoulos, Greece
Jure Marn, Slovenia
Masoud Masih-Tehrani, Iran
Amirreza Masoodi, Iran
Giovanni Meneghetti, Italy
Mehmet Selcuk Mert, Turkey
Miomir Mijić, Serbia
Vitaly Mikheev, Russia
Jonathon Mitchell-Smith, UK
Nikolaj Mole, Slovenia
Mohammad Hossein Moshaei, USA
Adrián Mota-Babiloni, Spain
Swarnajay Mukherjee, USA
Milan Naď, Slovakia
Marko Nagode, Slovenia
Janusz Narkiewicz, Poland
Balazs Nemeth, Hungary
Sasa S Nikolic, Serbia
Nagur Babu Noorbhasha, USA
Domen Novak, Slovenia
Gheorghe Oancea, Romania
Milosav Ognjanović, Serbia
Ivan Okorn, Slovenia
Simon Oman, Slovenia
Luca Oneto, Italy
Milan Ostrý, Czech Republic
Evren Ozbayoglu, USA
Govindasamy P, India
Iztok Palcic, Slovenia
Somnath Pan, India
Rok Pavlin, Slovenia
Stanislav Pehan, Slovenia
Tomaž Pepelnjak, Slovenia
Andrzej Perec, Poland
Damian Pietrusiak, Poland
Primož Podržaj, Slovenia
Pavel Polach, Czech Republic
Tomaž Požrl, Slovenia
Vladimir Popovic, Serbia
Primož Potočnik, Slovenia
Radu-Emil Precup, Romania
Jurij Prezelj, Slovenia
Ewan Pritchard, USA
Franci Pušavec, Slovenia
Sunil J. Raykar, India
Zoran Ren, Slovenia
Janez Rihtaršič, Slovenia
Aleksandar Rikalović, Serbia
Samuel Rodman Oprešnik, Slovenia
Alessandro Ruggiero, Italy
Izidor Sabotin, Slovenia
Farshid Sadeghi, USA

Mohammad Reza Safaei, USA
Graziano Salvalai, Italy
Gürcan Samtaş, Turkey
Robert Schmitt, Germany
Marcel Schweiker, Germany
Tine Seljak, Slovenia
Sathish Kumar Selvaperumal, Malaysia
Andrej Senegačnik, Slovenia
Vignesh V. Shanbhag, India
Ali Reza Shourangiz Haghighi, Iran
Silvio Simani, Italy
Vilmos Simon, Hungary
Samo Simončič, Slovenia
Janusz Skrzypacz, Poland
Janko Slavič, Slovenia
Lidija Slemenik Perše, Slovenia
Marco Sortino, Italy
Karsten Stahl, Germany
Vladimir Stanovov, Russia
Staniša Trajko Stojiljković, Serbia
Uroš Stritih, Slovenia
Róbert Szabolcsi, Hungary
Božidar Šarler, Slovenia
Domen Šeruga, Slovenia
Goran Šimunović, Croatia
Roman Šturm, Slovenia
Borivoj Šuštaršič, Slovenia
Jamaludin Mohd Taib, Malaysia
Behrouz Takabi, USA
Jože Tavčar, Slovenia
Arris S. Tijsseling, Netherlands
Eloisa Torres-Jimenez, Spain
Jovan Trajkovski, Slovenia
Roman Trochimczuk, Poland
Masaomi Tsutsumi, Japan
Toma Udiljak, Croratia
Miro Uran, Slovenia
Kamil Urbanowicz, Poland
Janez Urevc, Slovenia
Cuneyt Uysal, Turkey
Erdem Uzunsoy, Turkey
Octavio Vázquez-Gómez, Mexico
Joško Valentinčič, Slovenia
Branko Vasić, Serbia
Celine Vens, Belgium
Edgar Ernesto Vera Cardenas, Mexico
Vladislav V. Vershinin, Russia
Matej Vesenjak, Slovenia
Boris Vidrih, Slovenia
Rok Vrabič, Slovenia
Magd Abdel Wahab, Belgium
Frank Walther, Germany
Chao Wang, USA
Shu Wang, USA
Jürgen Weber, Germany
Daogao Wei, China
Walter Lindolfo Weingaertner, Brazil
Ding Wenfeng, China
Michał Wieczorowski, Poland
Zhang Xiaohong, China
Andrzej Zbrowski, Poland
Jie Zhang, UK
Song Zhang, China
Samo Zupan, Slovenia
Janez Žerovnik, Slovenia
Uros Župerl, Slovenia
Urban Žvar Baškovič, Slovenia

The Editorial would like to thank all the reviewers in participating in reviewing process.
We appreciate the time and effort and greatly value the assistance as a manuscript reviewer for Strojniški vestnik – Journal of Mechanical Engineering.

Vsebina

Strojniški vestnik - Journal of Mechanical Engineering
letnik 65, (2019), številka 1
Ljubljana, januar 2019
ISSN 0039-2480

Izhaja mesečno

Razširjeni povzetki (extended abstracts)

Strojniški vestnik - Journal of Mechanical Engineering 65(2019)1, SI 3
© 2019 Strojniški vestnik. Vse pravice pridržane.

Prejeto v recenzijo: 2018-04-23
Prejeto popravljeno: 2018-09-10
Odobreno za objavo: 2018-09-25

Metoda pridobivanja značilk napak na sestavljenih zobniških prenosnikih na osnovi EEMD in sosednjih koeficientov translacijsko invariantnih multivalčkov

Xinyu Pang[1,2,*] – Baoan Cheng[1] – Zhaojian Yang[1,2] – Feng Li[1]
[1] Tehniška univerza v Taiyuanu, Kolidž za strojništvo, Kitajska
[2] Shanxi laboratorij za avtomatizirano oprema za premogovništvo Kitajska

Sestavljeni zobniški prenosniki imajo v primerjavi z običajnimi prenosniki kompleksnejšo zgradbo, ta pa vodi do kompleksnih vibracijskih lastnosti. V signalu vibracij se skrivajo vibracijske lastnosti navadnega in planetnega zobniškega prenosnika, kakor tudi sklopljene vibracije. Zato obstaja interes za iskanje učinkovitih metod diagnosticiranja napak v tovrstnih prenosnikih. V članku je podan predlog metode pridobivanja značilk napak, ki bo uporabna za diagnosticiranje napak v sestavljenih zobniških prenosnikih.

Metoda bazira na EEMD in na sosednjih koeficientih translacijsko invariantih multivalčkov, omogoča pa določitev jasne spektralne ovojnice signala vibracij prenosnika. Uspešnost metode je bila dokazana s simulacijo in z eksperimentalnimi preskusi.

V študiji je bila metoda odstranjevanja šuma s sosednjimi koeficienti translacijsko invariantnih multivalčkov kombinirana z metodo EEMD za diagnosticiranje napak v sestavljenih prenosnikih. Na signalu je bila izvedena dekompozicija EEMD za izbiro visokofrekvenčnih komponent IMF z glavnimi informacijami na podlagi koeficienta energijske korelacije. Iz visokofrekvenčnih komponent IMF je bil najprej odstranjen šum s sosednjimi koeficienti translacijsko invariantnih multivalčkov, nato pa so bile rekonstruirane z nizkofrekvenčnimi signali za določitev frekvenčnega spektra in spektralne ovojnice očiščenega signala ter pridobivanje značilk napak v sestavljenih prenosnikih.

Opravljena je bila diagnostična obravnava posamičnih napak v obliki okrušenega zoba in abrazije, kakor tudi mešanih napak na različnih mestih.

Pri okrušenem zobu čelnega zobnika se je pojavil delno ojačen nizkofrekvenčni del spektra. Osnovno frekvenco napake spremljajo tudi njeni večkratniki, s čimer je dokazan obstoj okrušenega zoba.

Pri abraziji sončnega zobnika je napaka prisotna na vseh zobeh in napaka montaže planetnega zobnika je večja kot sicer. Amplituda frekvence napake planetnega zobnika je večja kot običajno. Frekvenca napake sončnega zobnika in njeni večkratniki se ujemajo s frekvenčno značilko abrazije sončnega zobnika, s čimer je dokazana abrazija na sestavljenem prenosniku.

Pri okrušenem zobu sončnega zobnika in mešani napaki abrazije čelnega zobnika Z3 vključuje glavna frekvenca v signalu vrtilno frekvenco nosilca planetnih zobnikov f_c, absolutno vrtilno frekvenco sončnega zobnika $f_{s1}^{(r)}$, frekvenco ubiranja f_{m3} čelnih zobnikov Z3 in Z4 ter večkratnika $1/4f_s$ in $2/4f_s$. Frekvenca ubiranja čelnih zobnikov f_{m3} je večja od vršne vrednosti v normalnem stanju. Signal po odstranitvi šuma v simulaciji je bil primeren za diagnostično obravnavo napak na prenosniku, saj je imel jasno frekvenčno karakteristiko, vključno z glavno frekvenco, njenimi večkratniki in stransko frekvenco.

V raziskavo bi bilo mogoče vključiti več oblik napak, kot so napake na notranjem obroču, napake na planetnem prenosniku in še posebej mešane napake na sestavljenem prenosniku. Obetavno raziskovalno področje bi bilo tudi pridobivanje značilk napak na ležajih sestavljenih prenosnikov.

Novost je metoda na osnovi EEMD in sosednjih koeficientov translacijsko invariantnih multivalčkov, ki ni primerna le za posamične napake, temveč tudi za mešane napake. Metoda omogoča uspešno pridobivanje značilk napak v sestavljenih zobniških prenosnikih in s tem točno identifikacijo napak. V simulacijah so bili uporabljeni signali vibracij s šumom, ki je bil odstranjen po različnih postopkih. Metoda na osnovi EEMD in sosednjih koeficientov translacijsko invariantnih multivalčkov ne omogoča le učinkovitega zmanjšanja šuma v signalu, temveč tudi pridobivanje značilk.

Ključne besede: sestavljeni prenosnik, pridobivanje značilk, EEMD, sosednji koeficienti multivalčkov, posamična napaka, mešane napake

---

*Naslov avtorja za dopisovanje: Tehniška univerza v Taiyuanu, Kolidž za strojništvo, No.79, Yingze West Street, Taiyuan, Kitajska, typangxy@163.com

Strojniški vestnik - Journal of Mechanical Engineering 65(2019)1, SI 4
© 2019 Strojniški vestnik. Vse pravice pridržane.

Prejeto v recenzijo: 2018-07-09
Prejeto popravljeno: 2018-11-09
Odobreno za objavo: 2018-12-13

Študija upravičenosti uvajanja hibridnih avtobusov v javnem potniškem prometu

Janez Blaž[1,*] – Samo Zupan[2] – Miha Ambrož[2]
[1] Republika Slovenija, Ministrstvo za infrastrukturo, Slovenija
[2] Univerza v Ljubljani, Fakulteta za strojništvo, Slovenija

Obravnavana problematika se nanaša na del optimizacije upravljanja javnega potniškega prometa kot obvezne gospodarske javne službe (GJS_JPP). Pristojno ministrstvo, ki je tudi v vlogi upravljavca medkrajevnega javnega potniškega prometa v Republiki Sloveniji ima nalogo, da glede na razpoložljiva javno finančna sredstva optimizira izvajanje te GJS_JPP, istočasno pa mora skrbeti da se v sistemu GJS_JPP uporabljajo čim bolj energijsko učinkovita in okolju prijazna prevozna sredstva. Pristojno ministrstvo ima namreč trenutno s 26 koncesionarji prevozniki podpisane koncesijske pogodbe, v sistemu GJS_JPP pa je vključenih približno 1100 avtobusov, ki prevozijo na letnem nivoju približno 48 milijonov kilometrov. Navedeni kazalniki so pokazali na upravičenost izvedbe raziskav, ki so prikazani v tem članku.

Predstavljeni izziv zahteva, da je potrebno pri novem razpisu podelitve koncesij v sistemu GJS_JPP (kar je v pristojnosti Ministrstva za infrastrukturo) določiti oziroma predpisati tudi pogoje glede uporabe prevoznih sredstev (avtobusov). V sistemu medkrajevnega potniškega prometa GJS_JPP v Republiki Sloveniji se izvaja približno 1700 linij in sicer kot hitre linije (tudi po avtocestah), kot lokalne linije, delno tudi kot linije mestnega prometa ali linije po hribovitih območjih. Zato je bil cilj raziskav postavitev in preizkus metodologije, ki bi na določenem karakterističnem izbranem pilotnem (hribovitem) obstoječem območju izvajanja GJS_JPP pokazala učinke uporabe avtobusov na alternativne oblike pogonov (hibridni avtobusi) in sicer tako z vidika prihrankov energije kot z vidika zmanjšanja škodljivih izpustov.

K raziskavam smo pristopili najprej s teoretičnimi izračuni potrebne energije, ki jo potrebuje avtobus za premagovanje vseh uporov na izbrani liniji oziroma karakterističnem pilotnem območju. Pri tem smo izhajali iz razpoložljivih tehničnih podatkov o avtobusih, ki se uporabljajo pri obstoječem izvajanju GJS_JPP na izbranem pilotnem območju. Pri teoretičnih izračunih smo upoštevali tudi negativne upore pri zaviranjih (vožnja po klancu navzdol, ustavljanje pred postajališči), ki bi jih teoretično lahko regenerirali. Nato smo izvedli primerjavo z eksperimentalnim delom meritev pri vožnji avtobusa na liniji, na kateri so bili predhodno izdelani teoretični izračuni.

Rezultati raziskav so pokazali, da je mogoče na pilotnem območju, ki predstavlja 0,28 % celotne mreže GJS_JPP, doseči 14 MWh prihrankov energije na letnem nivoju in približno 20 % zmanjšanja škodljivih izpustov. Največji izziv predstavlja natančna določitev stopnje izkoristka tako v transmisiji, kot v generatorju in baterijah. Poleg tega so rezultati odvisni tudi od načina vožnje (postopno zaviranje v primerjavi s sunkovitim zaviranjem). Iz teh razlogov morajo takšne raziskave vključiti tudi eksperimentalni del meritev med vožnjo avtobusov po karakterističnih linijah.

Raziskave so bile omejene na pilotno hribovito območja izvajanja GJS_JPP. V nadaljevanju predlagamo izvedbo eksperimentalnega dela tudi na hitrih linijah oziroma linijah kjer so visoke hitrosti in je sorazmerno malo ustavljanj in pospeševanj. Predlagamo tudi izvedba analiz ostalih alternativnih tehnologij pogona: CNG, kombinacija CNG- hibrid oziroma čisti električni pogon, ipd. Pri tem je potrebno izkoristiti specifičnost izvajanja GJS_JPP in sicer da so karakteristični profili in časi voženj oziroma poti vnaprej določeni.

Najpomembnejši rezultati predstavljajo izračuni učinkov tako na prihrankih energije kot pri zmanjšanju škodljivih izpustov. Investicije v vozila s takšnimi alternativnimi pogoni vsebujejo višje nabavne vrednosti, zato predstavljajo rezultati teh raziskav strokovno podlago upravljavcem javnega potniškega prometa pri njihovih odločitvah o uporabi takšnih vozil v sistemu GJS_JPP. To se običajno zahteva ob novih razpisih podelitve koncesij, kjer se optimalno določi tudi delež sofinanciranja države in lokalnih skupnosti.

Ključne besede: javni potniški promet, alternativne oblike pogona, hibridni avtobusi, energija regeneracije, izpusti emisij škodljivih plinov, linije javnega potniškega prometa, koncesije

---

*Naslov avtorja za dopisovanje: Republika Slovenija, Ministrstvo za infrastrukturo, Langusova ulica 4, SI-1000 Ljubljana, Slovenija, janez.blaz@gov.si

Strojniški vestnik - Journal of Mechanical Engineering 65(2019)1, SI 5

Prejeto v recenzijo: 2018-07-02
Prejeto popravljeno: 2018-10-20
Odobreno za objavo: 2018-11-05

Udarne sile v sistemu več razmaknjenih teles z dušenjem

Guillaume Ricciardi
CEA Cadarache, Francija

Udarne sile, ki nastanejo zaradi stika med telesi v primeru seizmičnega dogodka, lahko povzročijo škodo. Ocena največje sile, ki se lahko pojavi v primeru potresa, je zato pomembna pri projektiranju konstrukcij. Članek opisuje vpliv razmika in drugih parametrov na največje udarne sile, ki se lahko pojavijo v sistemu več teles. Podan je predlog brezdimenzijske enačbe za opis dinamike sistema. Opravljene so bile tudi numerične simulacije nad širokim območjem parametrov ob predpostavki, da se vitke konstrukcije upogibajo le s prvo lastno frekvenco.

Obravnavan je preprost sistem, sestavljen iz masnih teles, ki so s tlemi povezana z vzmetjo in viskoznim blažilnikom. Pomiki tal ustrezajo seizmičnim dogodkom. Telesa so razmaknjena in ob stiku se pojavijo udarne sile na levi oz. na desni strani telesa. Udarne sile ob stikih so modelirane z linearnimi vzmetmi, s čimer je upoštevana togost stika, ki se lahko razlikuje od togosti sistema. Za to študijo je bila izbrana linearna vzmet za opis lokalnih deformacij vitkega telesa na mestu stika, ki so mnogo večje od upogibne togosti.

Numerični rezultati kažejo na obstoj treh različnih področij. V prvem področju ni nobenih stikov med telesi. Za drugo področje je značilen zvezen razvoj koncentracije udarnih sil na mejah. Ko je v stiku le nekaj teles, število teh teles ni odvisno od skupnega števila stikov in zato je tudi hitro dosežena asimptotična vrednost.

Vedenje sistema v zadnjem področju z najpomembnejšimi udarnimi silami pa je kaotično in velja za manjše vrednosti zračnosti. Bifurkacijski diagram za prvo telo ilustrira razna vedenja nelinearnega sistema. Periodična rešitev preide v bifurkacijo z dvojno periodo in nato v kaos. Razviden je tudi zelo neenakomeren razvoj največjih udarnih sil kot funkcije zmanjšane frekvence z nenadnimi padci. Največje udarne sile v področju kaosa so veliko pomembnejše od teh sil v zveznem področju.

Na osnovi lineariziranega sistema in empirične formule za prvo lastno frekvenco je podan predlog zgornje meje verjetnih največjih udarnih sil. Kriterij je izpolnjen v zveznem področju, medtem ko so v kaotičnem področju določena odstopanja. Kriterij je vseeno primeren za ocenjevanje. Rezultat brezdimenzijske analize je, da je največja udarna sila sorazmerna z maso, pospeškom, razmerjem togosti in obratno vrednostjo koeficienta dušenja. Podan je predlog teoretične zgornje meje za največje sile ter primerjava z rezultati numerične simulacije in eksperimentov.

Eksperiment je bil zasnovan s stresalno mizo, na kateri je bila nameščena vrsta 46 vertikalnih vitkih konstrukcij (gorivnih sestavov), vpetih v podnožju. Konstrukcije lahko vibrirajo s prvo upogibno lastno frekvenco. Meritve udarnih sil so pokazale, da se največje sile pojavijo na skrajnem koncu. Največja reducirana udarna sila je bila manjša od sile, ocenjene s teoretično analizo. Poenostavljena analiza torej zagotavlja konzervativno zgornjo mejo. Razliko je mogoče pojasniti z dejstvom, da telesa niso sistemi z eno prostostno stopnjo in da se del disipacije energije lahko zgodi pri višjih frekvencah, poleg tega pa vzbujanje v eksperimentu ni harmonično in zato lahko nastopijo nekateri prehodni pojavi.

V prihodnjih študijah bi bilo mogoče preučiti še vpliv nehomogenosti razmikov in togosti ter nelinearne kontaktne togosti za boljši opis realnih sistemov. V prihodnosti bo opravljena tudi analiza sistema več nosilcev in primerjava s tukajšnjimi rezultati.

Ključne besede: sistem več teles, udarec, razmik, nelinearnost, kaos, dušenje

---

*Naslov avtorja za dopisovanje: CEA, Cadarache, 13108 Saint Paul lez Durance, Francija, guillaume.ricciardi@cea.fr

Strojniški vestnik - Journal of Mechanical Engineering 65(2019)1, SI 6

Prejeto v recenzijo: 2018-03-30
Prejeto popravljeno: 2018-10-17
Odobreno za objavo: 2018-11-13

Poslabšanje kakovosti notranjega okolja kot posledica obsežnih energijskih prenov

Mateja Dovjak[1,*] – Jan Slobodnik[1] – Aleš Krainer[2]
[1]Univerza v Ljubljani, Fakulteta za gradbeništvo in geodezijo, Slovenija
[2]Inštitut za sanitarno inženirstvo, Ljubljana, Slovenija

Obsežne energijske prenove v današnjem času potekajo v smeri enostranskih ukrepov in vključujejo visoko zrakotesnost in toplotno izolativnost stavbnega ovoja ter vgradnjo energijsko učinkovitih mehanskih sistemov za delovanje stavbe. Necelovit pristop se pogosto odrazi v poslabšanju kakovosti notranjega okolja, neudobnih in nezdravih razmerah ter ostalih možnih zdravstvenih izidih. Prenove so podprte s strani nacionalnih zakonskih zahtev, ki dopuščajo načrtovanje po minimalnih dovoljenih vrednostih za prezračevanje, medtem ko so ostale optimalne priporočene vrednosti praviloma neupoštevane. Kakovost notranjega okolja je pomembna v vseh delovnih in bivalnih okoljih; še posebej v vzgojno varstvenih in izobraževalnih, kjer so prisotne ranljive skupine in podaljšani časi izpostavljenosti dejavnikom tveganja za zdravje.

Raziskava se ukvarja s problematiko kakovosti notranjega okolja v vrtcih, kjer so številne epidemiološke raziskave odkrile slabo kakovost notranjega zraka kot najbolj problematično področje kakovosti notranjega okolja. Z namenom raziskave smo izvedli primerjalno analizo izbranih parametrov kakovosti notranjega zraka in rabe energije za pet scenarijev, kjer se je načrtovana stopnja prezračevanja spreminjala glede na nacionalne zakonske zahteve.

Za simulacijo smo uporabili model realnega vrtca, prenovljenega v letu 2016. Koncentracije CO_2 in formaldehida so bile izračunane v dveh modelnih igralnicah (starostna skupina 1 in 2) s programom CONTAM 3.2. Letna raba energije za ogrevanje je bila izračunana za dve toplotni coni igralnic obeh starostnih skupin s programom Energy Plus 8.8.0. Rezultati simulacij CO_2 so pokazali, da je posledica minimalne dovoljene vrednosti izmenjave zraka (air change ~ ACH) 0.5 najvišja koncentracija CO_2 v obeh modelnih igralnicah (igralnica A: 8891 mg/m^3, igralnica B: 7408 mg/m^3) in presega maksimalno dovoljeno vrednost CO_2 za kakovost notranjega zraka za 2,5 krat (igralnica B) in 3,0 krat (igralnica A). Posledica vseh zahtevanih in priporočenih načrtovanih stopenj prezračevanja je prekoračitev priporočenih vrednostih za CO_2 koncentracije za kategorijo 1 kakovosti notranjega zraka (Category I of IAQ), razen načrtovane stopnje prezračevanja 55 m^3/h na osebo. Rezultati simulacij koncentracij formaldehida v obeh modelnih igralnicah skoraj dosežejo priporočeno vrednost s strani WHO (World Health Organisation) in prekoračijo priporočeno vrednost s strani NIOSH-CDC (National Institute for Occupational Safety and Health) za 4,6 (igralnica A) in 4,5 krat (igralnica B). Posledica povečanja načrtovane stopnje prezračevanja iz 0.5 ACH (scenarij 1) na 55 m^3/h na osebo (scenarij 5) je 8,2 krat (igralnica A) in 6,8 krat (igralnica B) nižja CO_2 koncentracija ter 22,8 krat (igralnica A) in 17,6 krat nižja koncentracija formaldehida. Pri tem pa se je raba energije brez rekuperacije povečala za 5,67 krat (igralnica A) in 6,68 krat (igralnica B), z rekuperacijo pa 1,81 krat (igralnica A) in 2,08 krat (igralnica B), v primerjavi z referenčnim scenarijem 1 (0,5 ACH brez rekuperacije).

Sprejemanje odločitev v procesu graditve stavb mora potekati v smeri doseganja zdravih, udobnih in stimulirajočih razmer, varovanju okolja, ob minimalni možni rabi energije. Za doseg visoke kakovosti notranjega zraka so potrebni celoviti ukrepi (od izbora zdravju prijaznih materialov do zasnove sistema glede na lokacijsko kakovost z zraka) in vključujejo tudi izbor optimalnih vrednosti prezračevanja. To mora podpirati nacionalna zakonodaja. Definicija načrtovanih optimalnih stopenj prezračevanja naj izhaja iz raziskav, ki ugotavljajo, da višje vrednosti prezračevanja rezultirajo v boljši kakovosti zraka, zdravih in udobnih razmerah. Kot osnovni kriterij načrtovanja je dejansko število uporabnikov in ostali možni viri emisij.

Ugotovitve raziskave se prenese v ostala notranja okolja s podobno problematiko in se uporabi kot vodila pri določitvi politik in strategij v smeri zdravih notranjih okolij z osveščanjem in dvigom zavedanja vseh deležnikov v procesa graditve.

Ključne besede: vrtci, energijske prenove, kakovost zraka, prezračevanje

---

*Naslov avtorja za dopisovanje: Univerza v Ljubljani, Fakulteta za gradbeništvo in geodezijo, Jamova cesta 2, 1000 Ljubljana, Slovenija, mdovjak@fgg.uni-lj.si

Strojniški vestnik - Journal of Mechanical Engineering 65(2019)1, SI 7
© 2019 Strojniški vestnik. Vse pravice pridržane.

Prejeto v recenzijo: 2018-02-20
Prejeto popravljeno: 2018-07-07
Odobreno za objavo: 2018-08-09

Eksperimentalna raziskava toka newtonske in nenewtonske kapljevine v valovitih in ravnih minikanalih križnotočnega ploščnega prenosnika toplote

Ali Reza Anvari[1] – Koroush Javaherdeh[2,*]
[1] Univerza v Guilanu, Oddelek za strojništvo, Iran
[2] Univerza v Guilanu, Fakulteta za strojništvo, Iran

V članku je predstavljena raziskava nove tehnologije na področju prenosnikov toplote in medijev za prenos toplote. Kot medija za prenos toplote sta bila uporabljena deionizirana (DI) voda (newtonska tekočina) in vodna raztopina 0,2 ut. % karboksimetil celuloze (CMC) (nenewtonska kapljevina). Preučene so bile toplotne in reološke lastnosti nenewtonske kapljevine. Razvit je bil eksperimentalni sistem za preučevanje lastnosti prenosa toplote in izgube tlaka v valovitih in ravnih minikanalih pri različnih tokovnih razmerah.

Eksperimentalni sistem vključuje toplo in hladno kapljevino. Za vodne raztopine CMC velja potenčni zakon z eksponentom, manjšim od 1. Plošče prenosnika toplote so bile izdelane iz bakrove zlitine, vsaka pa je bila široka 80 mm, dolga 80 mm in debela 2 mm. Valoviti in ravni minikanali prereza 1 mm × 1 mm (skupaj 27 vzporednih kanalov) so bili izdelani na CNC-stroju. Uporabljeni sta bili dve vrednosti relativne valovitosti ($2A/2L = 0{,}2$ in 0,3). Delovanje minikanalnega križnotočnega prenosnika toplote (CFHE) je bilo preučeno za vrednosti Reynoldsovega števila (Re) od 200 do 1800. Vstopna temperatura toplejše testne tekočine je bila 40 °C do 50 °C, hladnejše vode pa 10 °C do 20 °C. Za tok fluida, ki je opisan s potenčnim zakonom, je bila uporabljena posplošena vrednost Re za nenewtonske kapljevine. Krivulja prenosa toplote je bila izračunana s pomočjo empiričnih formul za določitev Nusseltovega števila po Shahu, Londonu, Stephanu in Preußerju in uporabljena za validacijo eksperimentalnih podatkov o prenosu toplote. Potrjeno je bilo dobro ujemanje rezultatov z analizo.

Iz krivulje odvisnosti q od Re je razvidno, da je prenos toplote večji pri CFHE z valovitimi kanali in se povečuje z relativno valovitostjo. Ta zaključek potrjuje tudi analiza vrednosti U v odvisnosti od Re za hladno kapljevino. Eksperimentalna analiza za vodo in CMC je pokazala, da je faktor trenja pri valovitih kanalih vedno večji kot pri ravnih kanalih, vpliv nenewtonske kapljevine na povečanje tlačnega padca pa je manjši pri CFHE z relativno bolj valovitimi mikrokanali.

Kriterij za vrednotenje učinkovitosti (PEC) se povečuje približno sorazmerno z Reynoldsovim številom, celotno izboljšanje pri večjih pretokih iz naslova valovitih kanalov pa je signifikantno. Višjo vrednost PEC pri danem pretoku ima nenewtonska kapljevina z večjim utežnim deležem.

Pri obeh kapljevinah je toplotna učinkovitost valovitih minikanalov večja od toplotne učinkovitosti ravnih minikanalov. Kljub večjemu tlačnemu padcu je njegov vpliv pri visokih vrednostih Re majhen.

Analogni zapis formule za PEC ni bil jasno preverjen za tukajšnjo konfiguracijo.

Analizirati bi bilo treba stroške nenewtonske kapljevine v primerjavi z vodo, kakor tudi stroške izdelave CFHE z valovitimi kanali v primerjavi z ravnimi kanali.

Obstajajo dokazi, da je mogoče z novo konstrukcijo prenosnika toplote in novih medijev za prenos toplote intenzivirati proces prenosa toplote. Članek je namenjen nadaljnjemu razvoju tega področja.

Ključne besede: prenosnik toplote, minikanal, valovit, nenewtonska kapljevina, CMC, intenziviranje procesa

---

[*] Naslov avtorja za dopisovanje: Univerza v Guilanu, Oddelek za strojništvo, Iran, javaherdeh@guilan.ac.ir

Strojniški vestnik - Journal of Mechanical Engineering 65(2019)1, SI 8

Prejeto v recenzijo: 2018-04-13
Prejeto popravljeno: 2018-08-13
Odobreno za objavo: 2018-08-20

Raziskava sistema za pomoč pri speljevanju navkreber na osnovi elektronske parkirne zavore pri gospodarskih vozilih

Pai Peng[1] – Hongliang Wang[1,*] – Xianhui Wang[1] – Weihua Wang[2] – Dawei Pi[1] – Tianle Jia[1]

[1] Znanstveno-tehniška univerza v Nanjingu, Oddelek za strojništvo, Kitajska
[2] Univerza za pošto in telekomunikacije v Nanjingu, Šola za elektroniko, Kitajska

Cilj predstavljene študije je razvoj regulacijskega okvirja z logičnimi pragovi za izboljšanje kakovosti delovanja funkcije za pomoč pri speljevanju navkreber (HSA) pri gospodarskih vozilih, opremljenih z elektronsko parkirno zavoro (EPB), obenem pa izpolnitev zahtev glede varnega speljevanja. Najprej je podana podrobna analiza arhitekture in načela delovanja sistema EPB pri gospodarskih vozilih, kakor tudi lastnosti pnevmatskega sistema EPB. Na osnovi analize pnevmatskega sistema EPB je nato zasnovan načrt za regulacijo sistema HSA.

Model zahtevanega tlaka je oblikovan z analizo odvisnosti med dinamično komponento teže, zavorno silo in pogonsko silo. Postavljen je model pnevmatskega sistema EPB z elektromagnetnim ventilom in komoro parkirne zavore. Predstavljena je metoda regulacije z logičnimi pragovi za HSA pri gospodarskih vozilih s sistemom EPB. Elektromagnetni ventil v predlagani rešitvi je voden z regulirnim signalom s pulzno-širinsko in frekvenčno modulacijo (PWM-PFM) na osnovi razlike med dejanskim in nastavljenim tlakom, izpeljane iz pnevmatskega modela EPB.

Cilj regulacije je vzdrževanje nastavljenega tlaka, tj. sproščanje parkirne zavore s povečevanjem pogonskega momenta. Za vrednotenje uspešnosti strategije vodenja HSA je bil na platformi Matlab/Simulink oblikovan model vozila z modulom Trucksim, modelom krmilnika HSA in modelom pnevmatskega sistema EPB. Na ta način je bila vzpostavljena sosimulacijska platforma za scenarije speljevanja navkreber. Predlagani krmilnik je bil ovrednoten pri različnih naklonih (8, 13 in 18 %) in rezultati so pokazali, da lahko krmilnik učinkovito sledi nastavljenemu tlaku za učinkovito implementacijo funkcije HSA v okviru sistema EPB. Delovanje sistema HSA s predlaganim krmilnikom z logičnimi pragovi je bilo primerjano z dvema obstoječima krmilnikoma – konvencionalnim in krmilnikom Bang-Bang. Predlagani krmilnik očitno prekaša krmilnik Bang-Bang in konvencionalni krmilnik pri odlogu sprostitve zavor, tornem delu sklopke in sunkovitosti speljevanja pri vseh treh naklonih.

Opravljena je bila tudi eksperimentalna validacija uspešne implementacije HSA s predlaganim krmilnikom za naklone 8,2, 13 in 20 %. Rezultati eksperimenta tako kažejo, da predlagani krmilnik zagotavlja učinkovito sledenje nastavljeni vrednosti tlaka in zadovoljivo delovanje HSA pri gospodarskih vozilih s sistemom EPB. Odlog deaktiviranja parkirne zavore je dovolj kratek za manjšo obrabo sklopke in manj sunkovito speljevanje. Masa vozila je bila določena z meritvami odklona vzmetenja s Hallovim senzorjem zasuka, toda natančnost meritev je bila majhna zaradi spreminjanja položaja masnega središča s spreminjanjem obremenitve vozila.

Ena od možnih smeri za nadaljevanje tega dela je razvoj algoritma za prepoznavanje mase vozila med manevrom speljevanja navkreber za izboljšanje natančnosti identifikacije in zmanjšanje stroškov.

Najpomembnejši prispevek predstavljene raziskave je v tem, da je bila regulacija z logičnimi pragovi prvič uporabljena pri funkciji HSA gospodarskih vozil s sistemom EPB in da so bile dokazane njene prednosti, kot so preprosta regulacijska shema, robustnost in praktičnost.

Ključne besede: pomoč pri speljevanju navkreber, elektronska parkirna zavora, gospodarsko vozilo, regulacija z logičnimi pragovi, sosimulacija, eksperimenti

---

*Naslov avtorja za dopisovanje: Znanstveno-tehniška univerza v Nanjingu, Oddelek za strojništvo, Nanjing, Jiangsu, Kitajska, whl343@163.com

Information for Authors

All manuscripts must be in English. Pages should be numbered sequentially. The manuscript should be composed in accordance with the Article Template given above. The maximum length of contributions is 10 pages. Longer contributions will only be accepted if authors provide juastification in a cover letter. For full instructions see the Information for Authors section on the journal's website: http://en.sv-jme.eu .

SUBMISSION:

Submission to SV-JME is made with the implicit understanding that neither the manuscript nor the essence of its content has been published previously either in whole or in part and that it is not being considered for publication elsewhere. All the listed authors should have agreed on the content and the corresponding (submitting) author is responsible for having ensured that this agreement has been reached. The acceptance of an article is based entirely on its scientific merit, as judged by peer review. Scientific articles comprising simulations only will not be accepted for publication; simulations must be accompanied by experimental results carried out to confirm or deny the accuracy of the simulation. Every manuscript submitted to the SV-JME undergoes a peer-review process.

The authors are kindly invited to submit the paper through our web site: http://ojs.sv-jme.eu. The Author is able to track the submission through the editorial process - as well as participate in the copyediting and proofreading of submissions accepted for publication - by logging in, and using the username and password provided.

SUBMISSION CONTENT:

The typical submission material consists of:

- A **manuscript** (A PDF file, with title, all authors with affiliations, abstract, keywords, highlights, inserted figures and tables and references),
- Supplementary files:
  - a **manuscript** in a WORD file format
  - a **cover letter** (please see instructions for composing the cover letter)
  - a ZIP file containing **figures** in high resolution in one of the graphical formats (please see instructions for preparing the figure files)
  - possible **appendicies** (optional), cover materials, video materials, etc.

Incomplete or improperly prepared submissions will be rejected with explanatory comments provided. In this case we will kindly ask the authors to carefully read the Information for Authors and to resubmit their manuscripts taking into consideration our comments.

COVER LETTER INSTRUCTIONS:

Please add a **cover letter** stating the following information about the submitted paper:

1. Paper **title**, list of **authors** and their **affiliations**.
2. **Type of paper**: original scientific paper (1.01), review scientific paper (1.02) or short scientific paper (1.03).
3. A **declaration** that neither the manuscript nor the essence of its content has been published in whole or in part previously and that it is not being considered for publication elsewhere.
4. State the **value of the paper** or its practical, theoretical and scientific implications. What is new in the paper with respect to the state-of-the-art in the published papers? Do not repeat the content of your abstract for this purpose.
5. We kindly ask you to suggest at least two **reviewers** for your paper and give us their names, their full affiliation and contact information, and their scientific research interest. The suggested reviewers should have at least two relevant references (with an impact factor) to the scientific field concerned; they should not be from the same country as the authors and should have no close connection with the authors.

FORMAT OF THE MANUSCRIPT:

The manuscript should be composed in accordance with the Article Template. The manuscript should be written in the following format:

- A **Title** that adequately describes the content of the manuscript.
- A list of **Authors** and their **affiliations**.
- An **Abstract** that should not exceed 250 words. The Abstract should state the principal objectives and the scope of the investigation, as well as the methodology employed. It should summarize the results and state the principal conclusions.
- 4 to 6 significant **key words** should follow the abstract to aid indexing.
- 4 to 6 **highlights;** a short collection of bullet points that convey the core findings and provide readers with a quick textual overview of the article. These four to six bullet points should describe the essence of the research (e.g. results or conclusions) and highlight what is distinctive about it.
- An **Introduction** that should provide a review of recent literature and sufficient background information to allow the results of the article to be understood and evaluated.
- A **Methods** section detailing the theoretical or experimental methods used.
- An **Experimental section** that should provide details of the experimental set-up and the methods used to obtain the results.
- A **Results** section that should clearly and concisely present the data, using figures and tables where appropriate.
- A **Discussion** section that should describe the relationships and generalizations shown by the results and discuss the significance of the results, making comparisons with previously published work. (It may be appropriate to combine the Results and Discussion sections into a single section to improve clarity.)
- A **Conclusions** section that should present one or more conclusions drawn from the results and subsequent discussion and should not duplicate the Abstract.
- **Acknowledgement** (optional) of collaboration or preparation assistance may be included. Please note the source of funding for the research.
- **Nomenclature** (optional). Papers with many symbols should have a nomenclature that defines all symbols with units, inserted above the references. If one is used, it must contain all the symbols used in the manuscript and the definitions should not be repeated in the text. In all cases, identify the symbols used if they are not widely recognized in the profession. Define acronyms in the text, not in the nomenclature.
- **References** must be cited consecutively in the text using square brackets [1] and collected together in a reference list at the end of the manuscript.
- **Appendix(-icies)** if any.

SPECIAL NOTES

Units: The SI system of units for nomenclature, symbols and abbreviations should be followed closely. Symbols for physical quantities in the text should be written in italics (e.g. v, T, n, etc.). Symbols for units that consist of letters should be in plain text (e.g. ms^{-1}, K, min, mm, etc.). Please also see: http://physics.nist.gov/cuu/pdf/sp811.pdf .

Abbreviations should be spelt out in full on first appearance followed by the abbreviation in parentheses, e.g. variable time geometry (VTG). The meaning of symbols and units belonging to symbols should be explained in each case or cited in a **nomenclature** section at the end of the manuscript before the References.

Figures (figures, graphs, illustrations digital images, photographs) must be cited in consecutive numerical order in the text and referred to in both the text and the captions as Fig. 1, Fig. 2, etc. Figures should be prepared without borders and on white grounding and should be sent separately in their original formats. If a figure is composed of several parts, please mark each part with a), b), c), etc. and provide an explanation for each part in Figure caption. The caption should be self-explanatory. Letters and numbers should be readable (Arial or Times New Roman, min 6 pt with equal sizes and fonts in all figures). Graphics (submitted as supplementary files) may be exported in resolution good enough for printing (min. 300 dpi) in any common format, e.g. TIFF, BMP or JPG, PDF and should be named Fig1.jpg, Fig2.tif, etc. However, graphs and line drawings should be prepared as vector images, e.g. CDR, AI. Multi-curve graphs should have individual curves marked with a symbol or otherwise provide distinguishing differences using, for example, different thicknesses or dashing.

Tables should carry separate titles and must be numbered in consecutive numerical order in the text and referred to in both the text and the captions as Table 1, Table 2, etc. In addition to the physical quantities, such as t (in italics), the units [s] (normal text) should be added in square brackets. Tables should not duplicate data found elsewhere in the manuscript. Tables should be prepared using a table editor and not inserted as a graphic.

REFERENCES:

A reference list must be included using the following information as a guide. Only cited text references are to be included. Each reference is to be referred to in the text by a number enclosed in a square bracket (i.e. [3] or [2] to [4] for more references; do not combine more than 3 references, explain each). No reference to the author is necessary.

References must be numbered and ordered according to where they are first mentioned in the paper, not alphabetically. All references must be complete and accurate. Please add DOI code when available. Examples follow.

Journal Papers:

Surname 1, Initials, Surname 2, Initials (year). Title. Journal, volume, number, pages, DOI code.

[1] Hackenschmidt, R., Alber-Laukant, B., Rieg, F. (2010). Simulating nonlinear materials under centrifugal forces by using intelligent cross-linked simulations. *Strojniški vestnik - Journal of Mechanical Engineering,* vol. 57, no. 7-8, p. 531-538, DOI:10.5545/sv-jme.2011.013.

Journal titles should not be abbreviated. Note that journal title is set in italics.

Books:

Surname 1, Initials, Surname 2, Initials (year). Title. Publisher, place of publication.

[2] Groover, M.P. (2007). *Fundamentals of Modern Manufacturing*. John Wiley & Sons, Hoboken.

Note that the title of the book is italicized.

Chapters in Books:

Surname 1, Initials, Surname 2, Initials (year). Chapter title. Editor(s) of book, book title. Publisher, place of publication, pages.

[3] Carbone, G., Ceccarelli, M. (2005). Legged robotic systems. Kordić, V., Lazinica, A., Merdan, M. (Eds.), Cutting Edge Robotics. Pro literatur Verlag, Mammendorf, p. 553-576.

Proceedings Papers:

Surname 1, Initials, Surname 2, Initials (year). Paper title. Proceedings title, pages.

[4] Štefanić, N., Martinčević-Mikić, S., Tošanović, N. (2009). Applied lean system in process industry. *MOTSP Conference Proceedings*, p. 422-427.

Standards:

Standard-Code (year). Title. Organisation. Place.

[5] ISO/DIS 16000-6.2:2002. *Indoor Air – Part 6: Determination of Volatile Organic Compounds in Indoor and Chamber Air by Active Sampling on TENAX TA Sorbent, Thermal Desorption and Gas Chromatography using MSD/FID.* International Organization for Standardization. Geneva.

WWW pages:

Surname, Initials or Company name. Title, from http://address, date of access.

[6] Rockwell Automation. Arena, from *http://www.arenasimulation.com,* accessed on 2009-09-07.

EXTENDED ABSTRACT:

When the paper is accepted for publishing, the authors will be requested to send an **extended abstract** (approx. one A4 page or 3500 to 4000 characters). The instruction for composing the extended abstract are published on-line: http://www.sv-jme.eu/information-for-authors/ .

COPYRIGHT:

Authors submitting a manuscript do so on the understanding that the work has not been published before, is not being considered for publication elsewhere and has been read and approved by all authors. The submission of the manuscript by the authors means that the authors automatically agree to transfer copyright to SV-JME when the manuscript is accepted for publication. All accepted manuscripts must be accompanied by a Copyright Transfer Agreement, which should be sent to the editor. The work should be original work by the authors and not be published elsewhere in any language without the written consent of the publisher. The proof will be sent to the author showing the final layout of the article. Proof correction must be minimal and executed quickly. Thus it is essential that manuscripts are accurate when submitted. Authors can track the status of their accepted articles on http://en.sv-jme.eu/.

PUBLICATION FEE:

Authors will be asked to pay a publication fee for each article prior to the article appearing in the journal. However, this fee only needs to be paid after the article has been accepted for publishing. The fee is 380 EUR (for articles with maximum of 6 pages), 470 EUR (for articles with maximum of 10 pages), plus 50 EUR for each additional page. The additional cost for a color page is 90.00 EUR. These fees do not include tax.

Strojniški vestnik -Journal of Mechanical Engineering
Aškerčeva 6, 1000 Ljubljana, Slovenia,
e-mail: info@sv-jme.eu

ISSN 0039-2480

http://www.sv-jme.eu

Contents

Papers